Controlling Quantum Systems for Computation and Communication

Bikun Li

Dissertation submitted to the Faculty of the

Virginia Polytechnic Institute and State University

in partial fulfillment of the requirements for the degree of

Doctor of Philosophy

in

Physics

Edwin F. Barnes, Chair

Sophia E. Economou

Uwe C. Täuber

Vinh Nguyen

December 2, 2022

Blacksburg, Virginia

Keywords: Quantum Information, Quantum Physics

Controlling Quantum Systems for Computation and Communication

Bikun Li

(ABSTRACT)

Quantum information processing has the potential of implementing faster algorithms for numerous problems, communicating with more secure channels, and performing higher precision sensing compared to classical methods. Recent experimental technology advancement has brought us a promising future of harnessing such quantum advantage. Yet, quantum engineering entails wise control and strategy under the current noisy intermediate-scale quantum era. Developing robust and efficient approaches to manipulating quantum systems based on constrained and limited resources is imperative. This dissertation focuses on two major topics theoretically. In the first part, this work present how to conceive robust quantum control on matter-based qubits with a geometric approach. We have proposed the method of designing noise robust control pulses suitable for practical devices by combining spatial curves, filter functions, and machine learning. In the second part, this work stresses the topic of photonic multipartite entangled graph states. An improved protocol of generating arbitrary graph states is introduced. We show that one can efficiently find the deterministic photon emission circuit with minimal overhead on the number of quantum emitters.

Controlling Quantum Systems for Computation and Communication

Bikun Li

(GENERAL AUDIENCE ABSTRACT)

As classical information technology has revolutionized our modern world, theoretically, quantum information technology outperforms its classical counterpart and has the potential to achieve further progress. Utilizing the non-classical features unique to quantum physics, one can build quantum computers capable of accelerating data searching, breaking most current cryptographic systems, simulating molecular-level dynamics, and enhancing artificial intelligence. Furthermore, one can use the entangled quantum resource to establish secure communication or increase the capacity of the classical communication channel. Although numerous applications may reshape our daily life, industry, and scientific research, the mastery of quantum information technology is still challenging since quantum systems are more susceptible to noise than classical systems. Unlike classical signal processing, reading out an unknown quantum state will irreversibly change the state, while copying an unknown quantum state is strictly infeasible. Therefore, detecting and correcting errors from quantum data can be tricky. Depending on different platforms, establishing a complicated quantum network can also be constrained by the near-term noisy device. Mainly, what this work attempts to innovate are the previous results on quantum dynamical control pulse design and the protocol of entangling photons. For the former, the goal of this work is to develop control pulses that can decouple coherent noise in the quantum computer when manipulating the quantum information. This work combines the mathematical framework of spatial curve quantum control with filter functions and machine learning to yield new outcomes. The flexibility of this framework enables us to give neat mathematical analysis and obtain satisfying control pulses design for physical implementations through numerical experiments. For the latter,

this work studies a promising scheme of deterministically producing an entangling photonic quantum network, where quantum emitters are treated as the media to build up quantum non-locality. Achieving this emission process in the real world is desirable for distributing entangled quantum resources and realizing measurement-based quantum computation. In this case, we analyze the emitter overhead needed to generate an entangling photonic resource state, specifically when sending photons back for interactions is inaccessible. At last, we propose an efficient algorithm for producing the generation protocol along with several practical examples whose overheads on quantum emitters number are strictly optimized.

Dedication

To my family and friends.

Acknowledgments

I express my deepest gratitude to Prof. Ed Barnes and Prof. Sophia Economou. They have provided much academic guidance from various aspects during my PhD study. They are very responsive advisors who offer me many precious and beneficial opportunities. My PhD journey and probably future career would not go smoothly without their immense inspiration and generous support.

I would like to thank Prof. Uwe Täuber and Prof. Vinh Nguyen. They are respected committee members who have provided many pertinent comments and valuable suggestions in all of my PhD exams. Especially, Prof. Täuber offered much help in my postdoc application.

I would like to extend my sincere thanks to Prof. Shengfeng Cheng, who offered me support and care in my first year at Blacksburg. I would also like to thank all other members of Barnes and Economou joint group. I had the pleasure of knowing and working with so many people in this wonderful group. I really enjoy the environment studying and working here. At last, I would like to acknowledge Betty Wilkins, who made our graduate student life at Virginia Tech so much easy.

Contents

List of Figures ix

List of Tables xv

1 Introduction 1

2 Controlling Matter-Based Qubit Systems 4

2.1 Dynamics of Open Quantum System 5

2.1.1 Operator-Sum Representation 7

2.1.2 Time-Dependent Noise 9

2.2 Quantum Control 12

2.2.1 Dynamical Decoupling and Dynamical Error-Correcting Gate 12

2.2.2 Filter Function 15

2.3 Geometric Formalism for Gate Design 18

2.3.1 Overview 18

2.3.2 Counteracting Time-Dependent Noise with SCQC 22

2.4 Time Optimal Control with SCQC 34

2.4.1 PMP for Free-time and Fixed-End Problem 35

2.4.2 Demonstration of Deriving 2D Dubins Curve 37

2.4.3 Discovering Time-Optimal Pulses by Machine Learning 41

2.5 Quantum Error Correcting Code 48

2.5.1 Introduction of QECC 48

2.5.2 Stabilizer Formalism 51

3 Entangling Photonic Qubits **58**

3.1 Multipartite Entangled Photonic State: Graph State 59

3.2 Photonic Stabilizer State Generation Protocols 63

3.2.1 Introduction 64

3.2.2 Results and Discussion 66

3.2.3 Methods 78

3.2.4 Supplemental Notes 82

4 Conclusion and Outlook **91**

Bibliography **93**

List of Figures

2.1 Geometric space curves provide a general method to design quantum gates that are robust to environmental noise and other sources of error. The evolution of a system subject to noise can be mapped onto a space curve. We can reverse engineer this evolution by starting from a space curve and extracting the control Hamiltonian from its generalized curvatures. Choosing the space curve to be closed yields noise-cancelling control pulses. (This figure is adapted from [1]) 19

2.2 An illustration of a sequence of closed curves $\{r_m\}$, where the red dots represent the starting and ending points of each curve. Each curve in the sequence is obtained by integrating the previous. $r_0(s)$ is given by the integral of $e^{i\phi(Ts)}$. In this example, the integral of $r_3(s)$ is no longer a closed curve, so the sequence terminates and thus contains four curves in total (This figure is adapted from [2].) 25

2.3 (a) Seven control pulses (colored lines) that achieve $T^{-1}f(\omega,T) = \mathcal{O}(\omega^k T^k)$ noise cancellation. The kth pulse implements an x-rotation by angle $(k+1)\pi$. A square pulse that achieves a 9π rotation (black dotted line) is shown for comparison. The inset shows the maximum slopes (bandwidths) that are required for different k. These exhibit a $\sim k^3$ dependence at small k (green line). (b) The filter functions for the control pulses in (a) (colored lines). The asymptotic slopes of the filter functions are $\approx 2k$, indicating the $\mathcal{O}(\omega^{2k}T^{2k+2})$ suppression near $\omega T = 0$. The inset shows the same filter functions on a linear scale. (This figure is adapted from [2].) 27

2.4 (a) Closed curves $r_0(t)$ that generate a hierarchy of closed curves $r_k(t)$ up to $r_4(t)$ (see e.g., Fig. 2.2). The opening angles of the cusps at the origin determine the rotation angles θ. (b) Pulses that implement x-rotations of various angles with $k = 5$ time-dependent noise suppression. (c) The polynomial coefficients that define the control pulses shown in (b). 28

2.5 The full infidelities of the pulse with $k = 6$ for (a) a virtual random quantum bath, and (b) classical noise $\eta(t)$ with a soft high-frequency cutoff. Each curve is plotted with varying control gate time T, but fixed ω_B and λ/ω_B. The dashed curve shows the leading-order contribution of the infidelity for $\lambda/\omega_B = 10^{-2}$, which has an asymptotic slope $2k + 2 = 14$. The target operation is chosen to be an identity gate ($\theta = 8\pi$) so that we can compare with the Uhrig dynamical decoupling sequence (UDD_6) [3], which is also included in the figure. Results that include errors in $\Omega(t)$ are also displayed by data points with triangles (with coupling $\lambda/\omega_B = 10^{-2}$), where $\widetilde{p}_j$ is implemented with small fluctuations, whose standard deviation is δp_j. (This figure is adapted from [2].) 31

2.6 Optimized closed Dubins curve examples (blue curves) under the assumptions of $|\Omega(t)| \leq 1$, $\Omega^*(0) = \Omega^*(T) = -1$. The values of θ are taken as 1.2π and 0.6π for the left and right panels separately. The curves start at the origin tangential to the x-axis. In both figures, divided by purple line ℓ (Eq. (2.65)), the pink half-plane requires the trajectories' curvature being $+1$, and the cyan half-plane requires the trajectories' curvature being -1. 41

2.7 The ANN structure that this section uses for a PINN. The outputs are the expected trajectory and control function, while the input here is a single variable. As long as the activation functions in the hidden layers are continuous, the output will be a continuous function with respect to the input. To obtain the result in Fig. 2.8, our models use $\tanh(\cdot)$ as the activation function by default. The ANN has a fully connected layout with 6 hidden layers, each of them with 256 nodes. 10 outputs are needed for a 3×3 matrix $\mathbf{C}(t)$ and a control field $\Omega(t)$. 43

2.8 A near-optimal curve design outcome instance found by PINN. In the first 3 panels, red, green and green arrows represent $\mathbf{T}$, $\mathbf{N}$ and $\mathbf{B}$ separately. Panel (a,b,c) display the integrated curves of $\mathbf{T}$, $\mathbf{N}$ and $\mathbf{B}$. Under $T = 13.3$ and $\Delta = 1$. Panel (d) displays the control pulse at different T found by PINN, which value is bounded by $[0, 2]$. Panel (e) displays the square root of loss function v.s. different control time T, after $> 10^6$ steps of ANN training. The turning point in panel (e) implies a critical (optimum) control time $T_c \approx 13.23$. (f) presents the infidelity comparison between the result with the $T = 13.3$ pulse given in (d), and the result with $\Omega(t) \equiv 0$, $\Delta \cdot T = 2\pi$. . . . 46

3.1 A simple connected graph example $G(V, E)$, with $V = \{1, 2, \cdots, 40\}$, and $E = \{(1, 5), (6, 20), (11, 35), \cdots\}$. 60

3.2 Universal computation can be done on the square lattice cluster state shown in this figure, which is known as MBQC. 61

3.3 An example of applying local graph complementation LC_a, with $a = 6$. The graph state given by the left graph is LC equivalent to the right one by LC unitary $U_{LC}^{(6)}$. 62

3.4 The quantum emission scheme presented in [4]. Panel (a) shows a possible level structure of a quantum emitter. The green arrows stand for pumping group state subspace, and release a photon by spontaneous emission. Panel (b) shows the circuit representation of this emission process. 64

3.5 Illustration of the protocol solver algorithm. (a) An example of a 4-photon graph state. (b) The graph is mapped to a 1D lattice. (c) The height function is computed and found to have maximum value 2, implying 2 emitters are needed. These are added to the 1D lattice. (d) Starting from the target state and decoupled emitters, a time-reversed sequence of emitter gates, photon absorption events, and time-reversed emitter measurements is constructed, until all qubits are disentangled. Further details about this example can be found in the section 3.2.4. (This figure is adapted from [5].) 67

3.6 **Results for repeater graph states.** (a) 12-photon repeater graph state in which external photons are emitted first. (b) Same graph state as in (a), but with "natural" emission ordering. (c) Same graph state as in (b) but with some unnecessary edges deleted. (d), (e) and (f) show the height functions of the states in (a), (b) and (c), respectively. (g) Emission circuit for state shown in (c), where H is the Hadamard gate, $P = \mathrm{diag}(1, i)$ is the phase gate, and $X \equiv \sigma^x$. (This figure is adapted from [5].) 72

3.7 Scaling of emitter number and generation circuit depth. The maximum value of the height function $h_{\max}$, measurement counts, and gate counts needed to produce random graphs of size n_p are all averaged over 1024 graph realizations for each value of n_p drawn from an Erdös–Rényi ensemble with edge probability $p = 0.95$. Dashed curves are included to show the scaling with n_p and n_p^2. The error bars stand for the standard deviation of these realizations. (This figure is adapted from [5].) 76

3.8 Step-by-step illustration of the protocol solver. (a) A target graph state with 4 photons. (b) The set of generators $\mathcal{G}_f = \{g_m\}$ is depicted as a tableau in which each row corresponds to one generator. Different colors correspond to different Pauli operators. The first 4 columns correspond to photonic qubits, and the last 2 columns correspond to emitters. (c) Step by step demonstration of how to obtain the time-reversed generation sequence, where $\mathcal{G}_0 = \{\sigma_i^z\}$ is finally obtained. Explanations are in the main text. (d) Local Clifford equivalent graph state representations of tableaux in (c). (This figure is adapted from [5].) 82

3.9 Graph state generation circuits for the 4-photon example graph shown in Fig. 3.8. In this figure, p_j ($j = 1, 2, 3, 4$) labels different photonic qubits, and e_1 and e_2 are emitter qubits. At the end of each circuit, the photon qubits are in the target graph state displayed at the top right, while the emitter qubits are in state $|0\rangle$ after the measurements. (a) The emission circuit obtained from the steps in Fig. 3.8. (b) A different generation circuit that produces the same target graph state as in (a). This circuit is obtained by swapping qubits $1 \leftrightarrow 3$, resulting in a circuit that requires only one emitter. (This figure is adapted from [5].) 86

3.10 The emission circuit that generates a logical state of the Shor code, controlled by a local operation R (the yellow block). The inset displays the height function of $|\pm\rangle_L$, which has $h_{\max} = 2$. (This figure is adapted from [5].) . . 87

3.11 (a) and (b) show the emission circuit and height function for the repeater graph state of $2m$ photons displayed in (c). The boxed area of the circuit is repeated multiple times to generate photons $p_4, p_5, p_6, \cdots, p_{2m-6}$. (This figure is adapted from [5].) 88

3.12 (a) The graph for RGS, which has $6m$ vertices. The labels represent the emission sequence. (b) The height function $h(x)$ for the target graph state in (a). (This figure is adapted from [5].) 89

List of Tables

2.1 The transformation rules for Hadamard H, phase gate P and controlled-NOT operation CNOT. 53

3.1 The transformation rules for unitary operation $U = \sqrt{-iX} \equiv ZPHP^\dagger$ and $U = \sqrt{iZ} \equiv P^\dagger$, which are useful for local graph complementation (Eq. (3.3)). 62

Chapter 1

Introduction

After the development of the past three decades, quantum information science has evolved as an exciting, abundant, but challenging field. Attractive application schemes such as quantum computation [6–8], quantum communication [9, 10] and other many interesting scientific tasks [11] have emerged in this active area. Quantum information processing is no longer a hypothetical toy for theorists with the advancement of experimental techniques and device fabrication. Different approaches and schemes have been conceived and brought into real life to test the feasibility of achieving quantum advantage. Compared to its classical counterparts, the processing of quantum information is more challenging because of the novel feature of quantum physics. The challenge is not only coming from the vulnerability of controllable quantum states due to the exposure of noise, but also coming from performing quantum operations under physical constraints, such as preparing a quantum state with a limited physical resource. Although we may have a solid understanding of the foundation of quantum mechanics, designing robust and efficient ways of manipulating a quantum system are still a current major research task. Therefore, harnessing the power of quantum physics in reality with near-term technology requires much ingenious conception from the theoretical side.

Like any other control problem in the classical world, unwanted perturbations accumulated in the control process cause failure. closed-loop control is usually adopted to monitor and correct errors of this kind. However, in the quantum world, direct readout of the quantum

information will destroy the system's state. What is worse, the non-cloning theorem will prevent us from replicating an unknown state. In this case, to ease error accumulation, open-loop control or sophisticated error syndrome measurement is often used to protect the logical information [12]. Some early noise decoupling techniques in NMR experiments [13–15] have enlightened us to develop methods like dynamical decoupling and dynamical error-correcting gates [16–18] at an early stage. To substantially prolong the coherence time while suppressing noise, one has to optimize the control functions such that they are applicable to practical devices. Among various tricks that have been developed, this dissertation will concentrate on the mathematical framework known as geometric formalism or space curve quantum control (SCQC) [1, 2, 19–22]. The flexibility of this approach can fundamentally unleash us from designing a control pulse of infeasible shape, which facilitates practical application. Particularly, regarding this formalism, this dissertation will present the results of combining this framework with filter function [2] and machine learning, which separately attempt to suppress time-dependent noise and optimize the control time.

Another topic that this dissertation focuses on is how to entangle photonic qubits for practical applications. Traditionally, quantum optics is well known for transmitting quantum states between distant locations, which is useful for quantum networks and quantum cryptography. Photons can also be used for quantum computation based on different schemes [23–25]. The recent development of integrated photonic circuits [26] is making photons a prospective candidate for numerous quantum technologies. One of the main hurdles for exploiting the advantage of photons is establishing quantum entanglement among photonic qubits efficiently since a multi-partite entangled quantum state is commonly desired in different scenarios. Utilizing the quantum emitter as a mediator to build up the inter-photon entanglement [4, 27–29] is a possible way of overcoming the bottleneck. With these schemes, quantum graph states [30] as a key resource for diverse applications can be generated. To

facilitate experimental realization and promote theoretical understanding, this dissertation presents a protocol that improves these methods in the scheme without photon feedback. The algorithm provided by this protocol allows one to find the quantum circuit for generating arbitrary quantum graph states with the least number of emitter qubits [5].

Due to the limited knowledge of the author and the focus of this dissertation, we are not able to cover every aspect of the latest scientific progress. Nevertheless, some basic knowledge will still be reviewed to the reader to make this dissertation self-contained and complete. This dissertation is organized as follows: Chapter 2 will first briefly review the mechanism of quantum decoherence in section 2.1. The technique of quantum control will be introduced in section 2.2. In section 2.3, we will combine SCQC with a filter function to design control pulses that can mitigate time-dependent noise [2]. Section 2.4 starts with the discussion of optimization of control theory, and demonstrates our exploration of designing pulses with machine learning. Moreover, we provide the information of quantum error correction codes and the stabilizer formalism in section 2.5. Chapter 3 will focus on photonic system. The preliminary framework of graph state is given in section 3.1. In this chapter, section 3.2 presents the protocol for generating entangled photons while optimizing the emitter overhead. Finally, chapter 4 will give a summary and outlook of this dissertation.

Chapter 2

Controlling Matter-Based Qubit Systems

The purpose of this chapter is to introduce the mathematical framework of noise and some basic methods of error correction in quantum systems. We will start by introducing the dynamics of open quantum systems, which is suitable for describing most quantum systems. It should provide a convincing explanation of the noise or error mechanism that induces quantum decoherence. Given the models with noise, we will bring in the main focus of this chapter: designing robust quantum control that combats external perturbations. Such techniques developed for decades have been implemented on matter quantum devices like superconductor qubits, semiconductor quantum dot qubits, and trapped ions to prolong the lifetime of quantum information.

Like any other engineering problem, a practically meaningful quantum control scheme has to be robust. Otherwise, control error accumulates and corrupts the data when extending the control procedures temporally. After all, we hope that the desired quantum operation can still be approximately and reliably achieved with an imperfect device. Regarding quantum control on matter systems, this chapter will also present some original works from the author, which include how to combine the geometric formalism or the space curve quantum control (SCQC) with the filter function formalism and machine learning.

Furthermore, suppressing the noise at the control level may allow us to build fundamental

quantum computing modules that dive below the error threshold of quantum error correction. The latter is another theoretical pillar of realizing reliable quantum computation and communication. Correspondingly, as a complement to open-loop quantum control, a brief introduction to quantum error correction codes (QECC) will be given. The relevant sections of the stabilizer formalism will serve as references for the other parts of this dissertation.

2.1 Dynamics of Open Quantum System

Generally, to study the dynamics of an isolated quantum system, one can start with a Hamiltonian $\hat{H}$ that acts on a Hilbert space $\mathscr{H}$. If one uses the density matrix $\hat{\rho} := \sum_{mn} \rho_{mn}(t) \left|m\right\rangle \left\langle n\right|$, ($\left|m\right\rangle, \left|n\right\rangle \in \mathscr{H}$) to represent the quantum state, the equation of motion is given by Heisenberg's equation[1]:

$$i\frac{\mathrm{d}\hat{\rho}}{\mathrm{d}t} = [\hat{H}, \hat{\rho}] \ , \tag{2.1}$$

where we have useed the Schrödinger picture with $\hbar = 1$. The evolving density matrix can be written as

$$\hat{\rho}(t) = U(t)\hat{\rho}(0)U^{\dagger}(t) \tag{2.2}$$

with a unitary $U(t)$ that fulfills

$$i\frac{\mathrm{d}U(t)}{\mathrm{d}t} = \hat{H}U(t) \ , \tag{2.3}$$

since most of the quantum algorithms or applications are based on pure quantum states. Therefore, naively speaking, one can perform a unitary operation on the quantum state, which maintains its purity[2], by controlling a time-dependent $\hat{H}$.

[1] In this dissertation, we define $[A, B] := AB - BA$ as the commutator, and $\{A, B\} := AB + BA$ as the anti-commutator.

[2] The purity of a density matrix $\hat{\rho}$ is defined as $\mathrm{tr}\left(\hat{\rho}^2\right)$.

However, any realistic control scheme always comes with error — the practical controllable system is always interacting with the "outside world", namely, the bath or environment. Correspondingly, the Hilbert space should be mathematically decomposed as $\mathscr{H} = \mathscr{H}_{\text{sys}} \times \mathscr{H}_{\text{bath}}$, where the system part $\mathscr{H}_{\text{sys}}$ is what we want to control (sometimes called principal system or sub-system), and $\mathscr{H}_{\text{bath}}$ is a much larger Hilbert space we want to get rid of. In principle, one can treat $\mathscr{H}$ as the total Hilbert space of an isolated system, although the focus will be the reduced density matrix $\rho_{\text{sys}} := \sum_{ij} \rho_{ij}(t) \left|i\right\rangle \left\langle j\right| = \text{tr}_{\text{bath}}(\hat{\rho})$, $(\left|i\right\rangle \in \mathscr{H}_{\text{sys}})$. Under this system-bath relationship, the Hamiltonian is commonly expressed as [12]:

$$\hat{H} = \hat{H}_{\text{sys}} \otimes \mathbb{1} + \mathbb{1} \otimes \hat{H}_{\text{bath}} + \lambda \hat{H}_{\text{int}} \ , \tag{2.4}$$

in which $\hat{H}_{\text{sys}}$ and $\hat{H}_{\text{bath}}$ are separately supported on the system and the bath, and λ characterizes the coupling strength of these two via operator $\hat{H}_{\text{int}}$. Under most circumstances, $\hat{H}_{\text{int}}$ is a summation of terms like $\hat{S}_a \otimes \hat{B}_a$, where $\hat{S}_a$ and $\hat{B}_a$ are supported on the system and the bath respectively. Usually, S_a is an operator acting on a set of qubits we want to control, and B_a can be field operators for a bosonic bath [3] such as phonons and charge density waves, or spin operators for a spin bath [31, 32]. For example, the Hamiltonian below describes a qubit (two-level system) interacting with a bosonic bath [3]:

$$\hat{H} = \frac{1}{2}\boldsymbol{\Omega}(t) \cdot \boldsymbol{\sigma} + \sum_i \omega_i \hat{b}_i^\dagger \hat{b}_i + \frac{1}{2}\sigma_z \sum_i \lambda_i (\hat{b}_i^\dagger + \hat{b}_i) \ , \tag{2.5}$$

where $\boldsymbol{\Omega}$ is the control field, $\boldsymbol{\sigma} = (\sigma_x, \sigma_y, \sigma_z)$ is an operator vector of Pauli matrices that is acting on the qubit only. $\hat{b}_i$ is a bosonic field annihilation operator[3] of mode i and frequency ω_i, which couples to the qubit with strength λ_i. The first two terms of Eq. (2.5) act on the principal system and the bosonic bath separately, while the last interaction term indicates

[3]Bosonic field operators satisfy canonical commutation relationships: $[\hat{b}_i, \hat{b}_j^\dagger] = \delta_{ij}$ and $[\hat{b}_i, \hat{b}_j] = 0$.

that each bosonic mode can "dephase" the principal system by strength λ_i.

Unlike Eq. (2.1), now the differential equation for $\hat{\rho}_{\text{sys}}(t)$ is given by the master equation:

$$\frac{\mathrm{d}\hat{\rho}_{\text{sys}}}{\mathrm{d}t} = \mathcal{L}[\hat{\rho}_{\text{sys}}(t)] \tag{2.6}$$

with a superoperator $\mathcal{L}[\cdot]$. Under the approximation of a Markovian bath, that is, assuming the bath is memory-less, Eq. (2.6) is generally expressed as Lindblad equation [33]:

$$\frac{\mathrm{d}\hat{\rho}_{\text{sys}}}{\mathrm{d}t} = -i[\hat{H}_{\text{sys}}, \hat{\rho}_{\text{sys}}] + \sum_k \left(L_k \hat{\rho}_{\text{sys}} L_k^\dagger - \frac{1}{2} \left\{ L_k^\dagger L_k, \hat{\rho}_{\text{sys}} \right\} \right) , \tag{2.7}$$

in which L_k are called Lindblad operators. Due to the extremely high dimensionality of $\mathscr{H}_{\text{bath}}$, L_k or $\mathcal{L}[\cdot]$ can only be determined phenomenologically.

2.1.1 Operator-Sum Representation

Besides adding correction terms to an equation of motion like the master equation, another effective way of describing quantum decoherence is by using Kraus operators. Without loss of generality, we can continue the discussion based on the model of Eq. (2.4). Denote the state vector $|\mu\rangle, |\nu\rangle \in \mathscr{H}_{\text{bath}}$ with Greek letter indices. Suppose one initializes a decoupled total state as $\hat{\rho}(0) := \hat{\rho}_{\text{sys}} \otimes \hat{\rho}_{\text{bath}}$, with the bath part being $\hat{\rho}_{\text{bath}} := \sum_\nu p_\nu |\nu\rangle\langle\nu|$. Then the evolved density matrix $\hat{\rho}_{\text{sys}}(t)$ at time t is given by:

$$\begin{aligned} \hat{\rho}_{\text{sys}}(t) &= \mathrm{tr}_{\text{bath}} \left[U(t) \hat{\rho}(0) U^\dagger(t) \right] = \mathrm{tr}_{\text{bath}} \left[U(t) \left(\hat{\rho}_{\text{sys}} \otimes \sum_\nu p_\nu |\nu\rangle\langle\nu| \right) U^\dagger(t) \right] \\ &= \sum_{\mu,\nu} p_\nu \langle\mu| U(t) \left(\hat{\rho}_{\text{sys}} \otimes |\nu\rangle\langle\nu| \right) U^\dagger(t) |\mu\rangle = \sum_{\mu,\nu} K_{\mu\nu}(t) \hat{\rho}_{\text{sys}} K_{\mu\nu}^\dagger(t) \end{aligned} , \tag{2.8}$$

where $K_{\mu\nu}(t) := \sqrt{p_\nu}\,\langle\mu|\,U(t)\,|\nu\rangle$ is called a Kraus operator, with $|\mu\rangle, |\nu\rangle \in \mathscr{H}_{\text{bath}}$. Note that there are different representations of $K_{\mu\nu}$ for the same quantum operation, since in Eq. (2.8) one can replace $\{|\mu\rangle\}$ with a different orthonormal basis $\{|\mu'\rangle\}$ of $\mathscr{H}_{\text{bath}}$. When the interaction strength $\lambda = 0$, there is a representation such that $K_{\mu\nu} = U_{\text{sys}}\delta_{\mu,1}\delta_{\nu,1}$ recovers the unitary evolution (2.2). When $\lambda \neq 0$, the mapping (2.8) can change the purity of $\hat{\rho}_{\text{sys}}$, which can turn a pure state into a mixed state. We highlight that Kraus operators are usually complicated, that sometimes K_a cannot be reduced as an operator proportional to U_a when $\dim(\mathscr{H}_{\text{sys}}) > 2$, which means the hypothesis of a *random unitary channel* $\hat{\rho} \mapsto \sum_a p_a U_a \hat{\rho} U_a^\dagger$ is not always possible[4] for a multi-level system [34].

In fact, we can use an operator-sum to represent any reasonable quantum operations on a quantum state $\hat{\rho}$:

$$\hat{\rho} \mapsto \hat{\rho}' = \sum_a K_a \hat{\rho} K_a^\dagger \,. \tag{2.9}$$

Here "reasonable" means it will not flip the sign of the eigenvalues of $\hat{\rho}$, which is mathematically known as *completely positive* (CP) map. In some cases, we wish to preserve the trace $\text{tr}\,(\hat{\rho}) = \text{tr}\,(\hat{\rho}')$. Such a map is called a *completely positive trace preserving* (CPTP) map, where an additional constraint $\sum_a K_a^\dagger K_a = \mathbb{1}$ is required. Nevertheless, a trace-preserving map is not always necessary when tracking a particular probabilistic operation. Since the corruption of quantum information is a reasonable quantum operation, the operator-sum representation is a proper candidate for modeling quantum error channels. For example, the depolarizing channel that isotropically degrades a two-level quantum system (qubit) is defined as:

$$\hat{\rho}' = \mathcal{E}[\rho] = (1-p)\hat{\rho} + p\,(X\hat{\rho}X + Y\hat{\rho}Y + Z\hat{\rho}Z) \quad (0 \leq p \leq 1)\,, \tag{2.10}$$

[4] An counter-example of the trace-preserving map given in [34] is $\rho_{\text{sys}} \mapsto \frac{1}{j(j+1)}\sum_{a=1}^{3} J_a \rho_{\text{sys}} J_a^\dagger$, where J_a are spin operators of spin-j. For a qudit (d-level system, $d = 2j+1 > 2$), all Kraus operators $J_a/\sqrt{d(d+1)}$ are singular matrices if d is odd. Hence, they cannot be written as $\sqrt{p_a}U_a$.

where X, Y, Z are Pauli operators. The Kraus operators K_a in this case are $\sqrt{1-p}\mathbb{1}$, $\sqrt{p}X$, $\sqrt{p}Y$ and $\sqrt{p}Z$. $\hat{\rho}'$ becomes a completely mixed state as $p = 1/2$.

In the lab, we usually assume that $\hat{H}_{\text{sys}}$ is controllable for devices based on transmons, trapped ions, and quantum dots [35–37], since the control signal is usually directly delivered to the system of interest. As we are controlling $\hat{H}_{\text{sys}}$ in Eq. (2.4), the interaction term $\lambda\hat{H}_{\text{int}}$ can corrupt the quantum information by the mechanism depicted in this section. Thus, to achieve the quantum advantage, we are not only building the device on a system with a mild coupling to the bath (i.e. small λ), but we want to further suppress decoherence by appropriate control techniques.

2.1.2 Time-Dependent Noise

As we have mentioned in the previous sections, it is extremely challenging to predict the exact dynamics of an open system when dealing with a huge bath. In fact, the same issue arises in open systems of classical mechanics. An example is Brownian motion – the fluctuating motion of a small particle due to the stochastic memory-less collisions of the environment. A good approximation of the dynamics follows the Langevin equation:

$$m\ddot{\mathbf{x}} = -\gamma\dot{\mathbf{x}} + \boldsymbol{\eta}(t) \ , \tag{2.11}$$

where m is the mass of the particle, γ gives the damping, and $\boldsymbol{\eta}(t)$ is a time-dependent *stochastic force* from the environment, which has zero average $\langle\boldsymbol{\eta}(t)\rangle = 0$ and time correlation[5] $\langle\eta_i(t)\eta_j(t')\rangle = 2\gamma k_B T\delta_{ij}\delta(t-t')$. Here, k_B is the Boltzmann constant, T is the temperature of the bath, and $\delta(\cdot)$ is the Dirac delta function. Because of the fluctuation-dissipation

[5] In the rest of this dissertation, $\langle f\rangle$ and $\overline{f}$ both represent the expectation value of the quantity/operator f.

theorem, there happens to be a factor 2γ in the correlation function. This example implies that a good approximation of the dynamics sometimes does not need a full description of the entire system. Heuristically, it is also true for quantum systems governed by Eq. (2.4). For simplicity, let us consider $\hat{H}_{\text{sys}} = \hat{H}_0(t)$ to be a time-dependent controllable Hamiltonian, while $\hat{H}_{\text{bath}}$ and $\lambda\hat{H}_{\text{int}}$ are time-independent. Then the equation of motion in the interaction picture is:

$$i\frac{\mathrm{d}U_I(t)}{\mathrm{d}t} = \hat{H}_I(t)U_I(t) \tag{2.12}$$

if we denote $U_I(t) := e^{i(\mathbb{1}\otimes\hat{H}_{\text{bath}})t}U(t)$. The definition of $\hat{H}_I(t)$ is given by

$$\hat{H}_I(t) = \hat{H}_0(t)\otimes\mathbb{1} + \lambda e^{i(\mathbb{1}\otimes\hat{H}_{\text{bath}})t}\hat{H}_{\text{int}}e^{-i(\mathbb{1}\otimes\hat{H}_{\text{bath}})t}\ . \tag{2.13}$$

Applying this to the example (2.5), the second term

$$\frac{1}{2}\sigma_z\sum_i \lambda_i e^{i\omega_i\hat{b}_i^\dagger\hat{b}_i}(\hat{b}_i^\dagger + \hat{b}_i)e^{-i\omega_i\hat{b}_i^\dagger\hat{b}_i} = \frac{1}{2}\sigma_z\sum_i \lambda_i(\hat{b}_i^\dagger e^{i\omega_i t} + \hat{b}_i e^{-i\omega_i t}) \tag{2.14}$$

becomes time-dependent, even though the Hamiltonian is autonomous in the absence of time-dependent control. In this case, $\sum_i \lambda_i(\hat{b}_i^\dagger e^{i\omega_i t} + \hat{b}_i e^{-i\omega_i t})$ can be approximated by a classical stochastic scalar field $\eta(t)$ if each bosonic mode in the bath is assigned with random phases. Such a semi-classical approximation allows one to simulate the noise with a random unitary channel consisting of an ensemble of classical noise source without considering the details of the bath.

Due to the stochastic "unpredictable" nature of $\eta(t)$, a convenient way to treat the problem is to study its correlation functions, such as $\langle\eta(t)\eta(t')\rangle$. Many experiments characterize the

noise by its power spectrum density $S(\omega)$[38], which is defined by

$$\begin{aligned} \langle \eta(t)\eta(t')\rangle &= \int_{-\infty}^{\infty} S(\omega) e^{-i\omega(t-t')} \frac{\mathrm{d}\omega}{2\pi} \\ \Longleftrightarrow S(\omega) &= \int_{-\infty}^{\infty} \langle \eta(t)\eta(0)\rangle \, e^{i\omega t} \mathrm{d}t \ , \end{aligned} \tag{2.15}$$

in which we have assumed $\langle \eta(t)\eta(t')\rangle = \langle \eta(t-t')\eta(0)\rangle$. If $\langle \eta(t)\eta(t')\rangle \propto \delta(t-t')$, the resulting $S(\omega)$ is a constant function, and such noise is known as white noise. For scenarios in which $\left\|\hat{H}_{\mathrm{sys}}\right\| \gg \left\|\hat{H}_{\mathrm{bath}}\right\|$, $\eta(t)$ has slow fluctuations compare to the system, such that $\langle \eta(t)\eta(t')\rangle$ displays a relatively long-time correlation. In this case, $S(\omega)$ concentrates near zero frequency. In the limit of $\eta(t)$ being a constant, $S(\omega)$ appears to be a Dirac delta function centered at $\omega = 0$.

Finally, a limitation of analytically describing the dynamics of time-dependent noise $\eta(t)$ comes from the multi-point correlation function, such as $\langle \eta(x_1,t_1)\eta(x_2,t_2)\eta(x_3,t_3)\eta(x_4,t_4)\rangle$, where (x_i, t_i) is the spatial-temporal coordinate of the noise. Typically, Gaussian noise is assumed, due to the fact that its statistical dynamics is dictated by merely $\langle \eta(t)\rangle$ and $\langle \eta(t_1)\eta(t_2)\rangle$. However, practical stochastic noise generally has independent correlation functions at different orders, which affect the principal quantum system independently. A full description of the stochastic process $\eta(t)$ requires the data of all these independent functions, which is operationally inaccessible. As we investigate the quantum system in a more precise way, it will be more challenging to include such non-Gaussian effects [38, 39].

2.2 Quantum Control

2.2.1 Dynamical Decoupling and Dynamical Error-Correcting Gate

To preserve the coherence of quantum information as much as possible for practical use, researchers have found that the perturbation from the bath can be suppressed if the quantum system is controlled in a proper way. Dynamical decoupling (DD) and dynamical error-correcting gates (DECG) are open-loop techniques that mitigate the perturbation from the bath by applying special maneuvers on quantum systems. By definition, open-loop control inputs a control signal that is independent of the system's state. One should distinguish it from quantum error-correcting codes mentioned in the following sections, in which one will correct the error depending to what has been detected. Some famous experimental techniques for DD [13] like Hahn spin-echo [40] and the Carr–Purcell sequence [41] have been known in the field of nuclear magnetic resonance (NMR) since as early as the 1950s when the idea of quantum information science was as yet unformed. These schemes significantly suppress the dephasing effect on the nuclear spins, which has referential significance for quantum control. As for a quantum system, such as a single qubit, we usually have to consider not only the dephasing noise but also the bit-flip noise: the former decreases the coherence time T_2 and the latter decreases the coherence time T_1. In other words, developing new DD methods for universal noise is imperative.

We will use the following example of a DD sequence to demonstrate it is possible to decouple universal static noise [16]. Consider the following qubit Hamiltonian with the quasi-static noise approximation:

$$\hat{H}(t) = \frac{1}{2}\boldsymbol{\Omega}(t) \cdot \boldsymbol{\sigma} + \lambda \widehat{\mathbf{n}} \cdot \boldsymbol{\sigma} \tag{2.16}$$

where $\widehat{\mathbf{n}}$ is a random unit vector, λ is an unknown small number, and $\boldsymbol{\Omega}(t)$ is the control

pulse. With general λ, the Hamiltonian $\hat{H}(t)$ yields unitary evolution $U(t)$. On the other hand, if $\lambda = 0$, the unitary evolution is given by $U_0(t)$, which is supposed to be the target rotation at $t = T$. We can use these ingredients to study the influence of noise by switching to the interaction picture, where the evolution operator $U_I(t) := U_0^\dagger(t)U(t)$ is governed by the equation of motion:

$$i\frac{\mathrm{d}U_I}{\mathrm{d}t} = \hat{H}_I U_I \qquad \text{with} \qquad \hat{H}_I = \frac{\lambda}{2} U_0^\dagger \left(\widehat{\mathbf{n}} \cdot \boldsymbol{\sigma}\right) U_0 \tag{2.17}$$

The condition of decoupling the noise at time $t = T$ is $U_0(T) \approx U(T) \Rightarrow U_I(T) \approx \mathbb{1}$. Viola *et al*, [16, 17] showed that $U_I(T) = \mathbb{1} + \mathcal{O}(\lambda^2)$ can be satisfied if $\hat{H}_I(t)$ is a sequence consisting of Dirac delta functions. Specifically, if one sets $\hat{H}_I(t) \equiv \hat{H}_k \propto U_0^\dagger(t_k)\left(\widehat{\mathbf{n}} \cdot \boldsymbol{\sigma}\right) U_0(t_k)$ for $t_k \leq t < t_k + \tau$ ($t_k = k\tau$), then by the Magnus expansion:

$$U_I(T) = \exp\left[-i\tau(\hat{H}_1 + \hat{H}_2 + \cdots) + \mathcal{O}(\lambda^2)\right] . \tag{2.18}$$

Regardless of what system we are considering, as long as $\{U_0(t_k)\}$ forms a finite group[6] $\mathcal{G}$, $\hat{H}_1 + \hat{H}_2 + \cdots$ is proportional to the *center* of $\mathcal{G}$ with a factor λ. Thus, once we find $\{U_0(t_k)\}$ that trivializes the center (i.e. $\hat{H}_1 + \hat{H}_2 + \cdots \propto \mathbb{1}$), we have decoupled $U_I(T) = e^{i\phi}e^{i\mathcal{O}(\lambda^2)}$ (ϕ is a global phase). The center of $\mathcal{G}$ argument is useful in generalizing to a larger system of higher dimensions. More examples can be found in [16]. Returning to our model of a single qubit (2.17),

$$U_0(t_0) = \mathbb{1}, \quad U_0(t_1) = X, \quad U_0(t_2) = iZ, \quad U_0(t_3) = Y, \quad U_0(t_4) = \mathbb{1} \tag{2.19}$$

suffices to yield $H_1 + H_2 + H_3 + H_4 = 0 \propto \mathbb{1}$ and target rotation $U_0(T) = \mathbb{1}$. Accordingly, the required unitary operation at t_k is given by $U_0(t_k)U_0^\dagger(t_{k-1})$, namely, the control field function

[6] In this section, the global phase is omitted here for its matrix representation.

in Eq. (2.17) is

$$\mathbf{\Omega}(t) = \pi\left[\widehat{\mathbf{x}}\delta(t-t_1) + \widehat{\mathbf{y}}\delta(t-t_2) + \widehat{\mathbf{x}}\delta(t-t_3) + \widehat{\mathbf{y}}\delta(t-t_4)\right] \tag{2.20}$$

with $0 \leq t < 4\tau = T$, where $\widehat{\mathbf{x}}$ and $\widehat{\mathbf{y}}$ are unit vectors along the x and y directions. Eq. (2.20) is known as XY-4 DD sequence [15]. Even though infinitely fast and accurate pulses are required, the higher-order error $\mathcal{O}(\lambda^2)$ is actually eliminated in this single qubit case of Eq. (2.16). Implementing a DD sequence with bounded control field with $U_I(T) = e^{i\phi}e^{i\mathcal{O}(\lambda^2)}$ is possible by analyzing the *Eulerian cycle*, one of the outcomes is also known as XY-8 sequence [15, 18]. We will not cover the technical details here.

As for the DECG, the goal is to implement a unitary operation on the quantum system, in the way that is robust to noise. The analysis will be as similar as in Eq. (2.17), except for replacing $U_0(T) = \mathbb{1}$ by a non-identity unitary $U_0(T) = U_{\text{gate}}$. Depending on what operation resource one can have in the lab, the design of the pulse can be challenging and may heavily rely on numerics (e.g. the Gradient Ascent Pulse Engineering (GRAPE) method [42]). Under the assumption that we can still fully control an arbitrary bounded $\hat{H}_{\text{sys}}$, a remarkable systematic approach is given by [43], although current devices are still too noisy to gain advantages from this protocol.

Once we have a robust control pulse that outperforms the naive pulse, better quantum devices can be built upon these building blocks. How do we characterize the performance of DD and DECG? There are many different measures [3, 44]. A convenient and fair measure is utilizing the average Uhlmann-Jozsa fidelity between two quantum states $\hat{\rho}_1, \hat{\rho}_2$ [45–47]:

$$F(\hat{\rho}_1, \hat{\rho}_2) = \left[\text{tr}\left(\sqrt{\sqrt{\hat{\rho}_1}\hat{\rho}_2\sqrt{\hat{\rho}_1}}\right)\right]^2 . \tag{2.21}$$

We expect that a perfect unitary operation $U_0(T)$ will transform an initial pure state $|\psi_0\rangle\langle\psi_0|$

to a target state $\hat{\rho}_1 = U_0(T)\,|\psi\rangle\langle\psi|\,U_0(T)^\dagger$. For comparison, the actual control outcome is given by a linear CPTP map $\hat{\rho}_2 = \mathcal{M}[|\psi_0\rangle\langle\psi_0|]$. Thus, we can represent the performance of a control pulse by averaging $F(\hat{\rho}_1, \hat{\rho}_2)$ for initial state $|\psi_0\rangle\langle\psi_0|$:

$$\overline{\mathcal{F}} = \overline{F(\hat{\rho}_1, \hat{\rho}_2)} = \overline{\langle\psi_0|\,U_0^\dagger(T)\mathcal{M}[|\psi_0\rangle\langle\psi_0|]U_0(T)\,|\psi_0\rangle}\ . \tag{2.22}$$

The average can be conveniently found by using the notion of a *unitary 1-design* with a Weingarten function [48]. Namely, the average of $F(\hat{\rho}_1, \hat{\rho}_2)$ can be equivalently taken on a finite discrete set of $|\psi_0\rangle$. Specifically, for a single qubit $|\psi_0\rangle$, this finite discrete set of states can be generated by applying the single-qubit Clifford group, and the calculation of $\overline{\mathcal{F}}$ can be simplified as [47]

$$\overline{\mathcal{F}} = \frac{1}{2} + \frac{1}{12}\sum_{j=x,y,z} \mathrm{tr}\left(U_0(T)\sigma_j U_0^\dagger(T)\mathcal{M}\left[\sigma_j\right]\right)\ . \tag{2.23}$$

In the special case of Eq. (2.17), where we would like to use an instance of randomly perturbed $U(T)$ to represent the linear map, that is, $\mathcal{M}[|\psi_0\rangle\langle\psi_0|] = U(T)\,|\psi_0\rangle\langle\psi_0|\,U^\dagger(T)$. Then

$$\overline{\mathcal{F}} = \frac{1}{2} + \frac{1}{12}\sum_{j=x,y,z} \mathrm{tr}\left(U_I\sigma_j U_I^\dagger\sigma_j\right) = \frac{2 + |\mathrm{tr}(U_I)|^2}{6}\ , \tag{2.24}$$

where $U_I = U_0^\dagger(T)U(T)$ is the same unitary operator in the interaction picture Eq. (2.17).

2.2.2 Filter Function

We have to admit that Eq. (2.17) is an oversimplified model with time-independent classical noise. As has been discussed in the previous sections, the external environment, whether it is classical or quantum mechanical, typically has complicated dynamics. This sub-section will

introduce the filter function and explain its role in dealing with time-dependent noise. The precise definition of this quantity varies depending on the type of observable one considers. In this dissertation, we start with the approximation of time-dependent classical noise, and rewrite the single qubit Hamiltonian $\hat{H}_I$ in Eq. (2.17) as:

$$\hat{H}_I(t) = \lambda U_0^\dagger(t) \left(\boldsymbol{\sigma} \cdot \boldsymbol{\eta}(t)\right) U_0(t) \ . \tag{2.25}$$

The resulting evolution operator $U_I(t)$ can be expanded using a Magnus expansion:

$$\begin{aligned} U_I &= \mathcal{T} \exp\left[-i \int_0^t \hat{H}_I(t) \mathrm{d}t\right] = e^{-i\left(M_1(t)+M_2(t)+\mathcal{O}(\lambda^3)\cdots\right)} \\ &= \mathbb{1} - i\left[M_1(t) + M_2(t)\right] - \frac{1}{2} M_1(t)^2 + \mathcal{O}(\lambda^3) \ , \end{aligned} \tag{2.26}$$

where $M_1(t) = \int_0^t \hat{H}_I(\tau)\mathrm{d}\tau$, $M_2(t) = \frac{1}{2}\int_0^t \mathrm{d}\tau \int_0^\tau \mathrm{d}\tau' [\hat{H}_I(\tau), \hat{H}_I(\tau')]$. The performance of $U_I(t)$ at $t = T$ can be quantified by the average fidelity $\overline{\mathcal{F}}$ in Eq. (2.24):

$$\begin{aligned} \overline{\mathcal{F}} &= \frac{1}{3} + \frac{1}{6} \left\langle \left| \mathrm{tr}\left[\mathbb{1} - i\left[M_1(T) + M_2(T)\right] - \frac{1}{2} M_1(T)^2 + \mathcal{O}(\lambda^3)\right] \right|^2 \right\rangle \ . \\ &= 1 - \frac{1}{3} \langle \mathrm{tr}\left(M_1^2\right)\rangle + \mathcal{O}(\lambda^3) \end{aligned} \tag{2.27}$$

From the above equation, the average infidelity $1 - \overline{\mathcal{F}}$ is dominated ($\lambda \ll 1$) by:

$$\begin{aligned} \frac{1}{3}\langle \mathrm{tr}\left(M_1^2\right)\rangle &= \frac{\lambda^2}{3} \int_0^T \mathrm{d}\tau \int_0^T \mathrm{d}\tau' \left\langle \mathrm{tr}\left[\left(\boldsymbol{\sigma}(\tau) \cdot \boldsymbol{\eta}(\tau)\right)\left(\boldsymbol{\sigma}(\tau') \cdot \boldsymbol{\eta}(\tau')\right)\right]\right\rangle \\ &= \frac{2\lambda^2}{3} \int_0^T \mathrm{d}\tau \int_0^T \mathrm{d}\tau' \sum_{i,j=1}^{3} M_{ij}(\tau - \tau') \left\langle \eta_i(\tau)\eta_j(\tau')\right\rangle \\ &= \frac{1}{3} \sum_{i,j=1}^{3} \int_{-\infty}^{\infty} \frac{\mathrm{d}\omega}{2\pi} F_{ij}(\omega, T) S_{ij}(\omega) \ , \end{aligned} \tag{2.28}$$

in which $\boldsymbol{\sigma}(\tau) := U_0(\tau)\boldsymbol{\sigma}U_0^\dagger(t)$ and $M_{ij}(\tau-\tau')$ is given by

$$M_{ij}(\tau-\tau') := \frac{1}{2}\mathrm{tr}\left[\sigma_i U_0^\dagger(\tau-\tau')\sigma_j U_0(\tau-\tau')\right] . \tag{2.29}$$

The last equal sign of Eq. (2.28) is obtained by Fourier transformation — as mentioned in Eq. (2.15), $S_{ij}(\omega) = \int_{-\infty}^{\infty} \langle \eta_i(\tau)\eta_j(0)\rangle\, e^{i\omega\tau}\mathrm{d}\tau$ is the (tensorial) noise power spectral density, while $F_{ij}(\omega, T)$ is the filter function that we are looking for:

$$F(\omega, T) := \int_0^T \mathrm{d}\tau \int_0^T \mathrm{d}\tau' M(\tau-\tau')e^{-i\omega(\tau-\tau')}. \tag{2.30}$$

Note that in Eq. (2.28), if $\boldsymbol{\eta}(t)$ describes white noise such that $\langle \eta_i(\tau)\eta_j(\tau')\rangle \propto \delta(\tau-\tau')$, then $\langle \mathrm{tr}\,(M_1^2)\rangle \propto \lambda^2 \int_0^T \mathrm{tr}(\mathbb{1})\mathrm{d}\tau = 2\lambda^2 T$ regardless of $U_0(t)$. Therefore, there is no control pulse that can improve the fidelity on average under white noise. On the other hand, for slow fluctuating noise where $S_{ij}(\omega)$ concentrates near $\omega = 0$, one may manage to manipulate $F_{ij}(\omega, T)$ by using a proper $U_0(t)$, thereby diminishing the integral appearing in $\langle \mathrm{tr}\,(M_1^2)\rangle$. Yet, this leading term will not completely vanish as long as the noise fluctuates.

The filter function also appears as one considers quantum noise [3, 49]. A similar computation can be found in [2]. Qualitatively speaking, a faster and denser control pulse gives better filtration for the noise because higher frequency noise usually can be suppressed by concatenating the DD sequence within the original control sequence during the free evolution, which is known as concatenated dynamical decoupling (CDD) [50]. As one increases the concatenation levels, the filter function has a shallower and wider filtration window near $\omega = 0$. Uhrig later derived with a more efficient pulse sequence [3, 51] known as UDD, which gives an analytical filter function while outperforming CDD with fewer operations. Since there has been a massive usage of filter functions in classical information processing, there are plenty of recent works regarding quantum control, which attempt to optimize control

pulses based on traditional techniques, like Slepian functions [52–54].

2.3 Geometric Formalism for Gate Design

2.3.1 Overview

In this section, we will describe an intuitive way of understanding quantum dynamical correcting pulses. The approach known as "geometric formalism" or "space curve quantum control (SCQC)" allows us to design control fields that dynamically correct errors while implementing different operations, by manipulating space curves. This overview subsection is partially based on the published review paper [1]: Edwin Barnes, Fernando A Calderon-Vargas, Wenzheng Dong, **Bikun Li**, Junkai Zeng, and Fei Zhuang, "Dynamically corrected gates from geometric space curves" *Quantum Science and Technology* 7 023001 (2022).

As we have discussed and demonstrated in the previous section, it is possible to drive a system with external control pulses that are engineered to produce an automatic self-cancellation of errors due to the environment or driving imperfections without the need for precise knowledge of these errors, as was discovered several decades ago.

There has also been substantial progress in developing control schemes that not only remove errors but also simultaneously rotate the quantum state of the system in some desired way [14, 55–65]. The analytical tractability of ideal pulse waveforms such as delta-functions and square pulses make them attractive as building blocks in such methods. However, the use of such waveforms can also potentially limit their applicability. This is because idealized waveforms are experimentally infeasible in many quantum systems, where the need for ultrafast microsecond or nanosecond control pushes the limits of state-of-the-art waveform generators to the point where these pulse shapes cannot be reliably created, incurring large

driving errors. Moreover, restricting to the use of only a few specialized pulse shapes can lead to unnecessarily long pulse sequences that quickly run up against limitations set by additional decoherence or loss mechanisms.

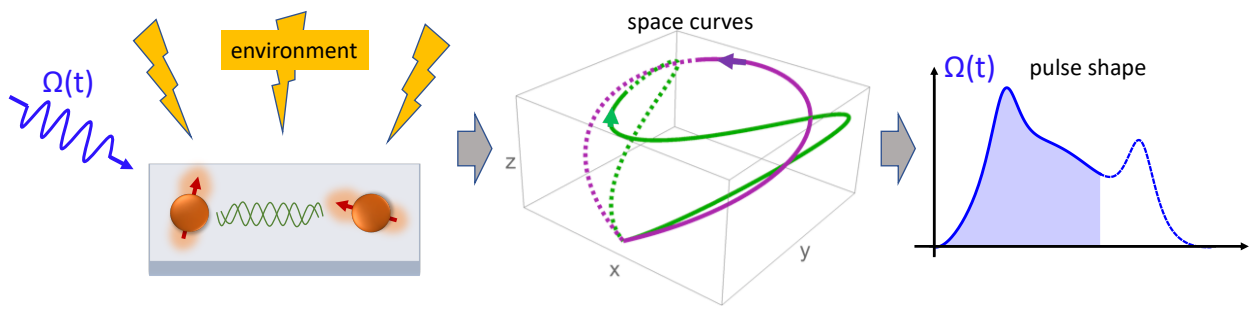

Figure 2.1: Geometric space curves provide a general method to design quantum gates that are robust to environmental noise and other sources of error. The evolution of a system subject to noise can be mapped onto a space curve. We can reverse engineer this evolution by starting from a space curve and extracting the control Hamiltonian from its generalized curvatures. Choosing the space curve to be closed yields noise-cancelling control pulses. (This figure is adapted from [1])

This section gives an overview of SCQC [2, 19–22]. This framework relies on a geometric structure underlying the Schrödinger equation that can be exploited to overcome limitations of existing approaches. In the SCQC method, one visualizes the evolution error caused by noise as a geometric space curve. This curve lives in a space of operators that depends on the form of the control Hamiltonian and on the way in which the noise affects the system. As the system evolves in time, the curve winds through this space with constant velocity. The net displacement between the initial and final points of the curve quantify the deviation from the system's ideal evolution. Any dynamically corrected gate therefore corresponds to a closed space curve, providing a global view of the solution space of robust gates. We show how one can systematically design robust gate operations by starting from closed space curves and computing control fields from their generalized curvatures [22]. The general strategy is illustrated in Fig. 2.1. As we describe in this work, this approach can be applied to a variety of contexts, including the design of single- or multi-qubit gates and Landau-Zener

interferometry, both for quasistatic and time-dependent noise. Moreover, it can be combined with holonomic methods to suppress multiple noise sources simultaneously. Space curves also provide a natural way to obtain dynamically corrected gates that operate near the quantum speed limit. While here we focus on correcting noise errors, the method can be applied to any situation in which reverse-engineering the evolution of a quantum system is needed.

We illustrate how SCQC works by reusing the model of Eq. (2.16). For simplicity, let $\widehat{\mathbf{n}} = \widehat{\mathbf{z}}$ and $\mathbf{\Omega}(t) = (\Omega_x(t), 0, 0)$, which is the setup in [20]. The Magnus expansion of the unitary in the interaction picture is $U_I(t) = e^{-i\left(M_1(t)+M_2(t)+\mathcal{O}(\lambda^3)\cdots\right)}$, with:

$$\begin{aligned}
M_1(t) &= \lambda \int_0^t e^{i\frac{\phi(\tau)}{2}\sigma_x}\sigma_z e^{-i\frac{\phi(\tau)}{2}\sigma_x}\mathrm{d}\tau = \lambda \int_0^t \left[\sigma_z \cos\phi(\tau) + \sigma_y \sin\phi(\tau)\right]\mathrm{d}\tau \\
M_2(t) &= \frac{\lambda^2}{2}\int_0^t \mathrm{d}\tau \left[e^{i\frac{\phi(\tau)}{2}\sigma_x}\sigma_z e^{-i\frac{\phi(\tau)}{2}\sigma_x}, \int_0^\tau \mathrm{d}\tau' e^{i\frac{\phi(\tau')}{2}\sigma_x}\sigma_z e^{-i\frac{\phi(\tau')}{2}\sigma_x}\right] \\
&= \frac{\lambda}{2}\int_0^t \mathrm{d}\tau \left[e^{i\frac{\phi(\tau)}{2}\sigma_x}\sigma_z e^{-i\frac{\phi(\tau)}{2}\sigma_x}, M_1(\tau)\right] \\
&\vdots
\end{aligned} \tag{2.31}$$

where $\phi(\tau) = \int_0^t \Omega_x(s)\mathrm{d}s$. Let us observe $M_1(t)$ closely: If one interprets $(\cos\phi, \sin\phi)$ as a unit tangent vector, then operator M_1 can be treated as a planar curve C: $\int_0^t (\cos\phi, \sin\phi)\mathrm{d}\tau$. Concretely, with "control time" T, $C : [0, T] \to \mathfrak{su}(2)$, in which we also replace $\mathfrak{su}(2)$ by $\mathbb{R}^3$ for convenience. The geometric interpretation of $C(t)$ is clear:

1. The arc length of $C(t)$ is the control time T, since it is parameterized such that $\left|\frac{\mathrm{d}C}{\mathrm{d}t}\right| = 1$.

2. The curvature of $C(t)$ is the control field $\Omega_x(t)$, since the angle $\phi(t)$ in the tangent vector $\frac{\mathrm{d}C}{\mathrm{d}t}$ is steered by the rate $\Omega(t) = \dot{\phi}(t)$.

3. The angle between $\frac{\mathrm{d}C(0)}{\mathrm{d}t}$ and $\frac{\mathrm{d}C(T)}{\mathrm{d}t}$ corresponds to the target rotation of $U_0(T) = \exp\left(-i\frac{\phi(T)}{2}\sigma_x\right)$.

Thus, a vanishing $M_1(T) = 0$ requires $C(t)$ be a closed curve: $C(T) = C(0)$. That is to say, given a closed curve $C(t)$, which probably has a cusp at $t = 0$ (or $t = T$), one can find the DECG pulse $\Omega(t)$ by reading its curvature.

After we treat $M_1(t)$ as a curve $C(t)$, it is easy to recognize that M_2 is proportional to the signed area enclosed by $C(t)$. This is due to the conversion of the commutator to cross-product:

$$[\mathbf{a} \cdot \boldsymbol{\sigma}, \mathbf{b} \cdot \boldsymbol{\sigma}] = (\mathbf{a} \times \mathbf{b}) \cdot \boldsymbol{\sigma} \ , \tag{2.32}$$

from which one can use Green's theorem (or Stoke's theorem) $A = \int \mathrm{d}x\mathrm{d}y = \frac{1}{2} \oint \mathbf{r} \times \dot{\mathbf{r}} \mathrm{d}t$ to find out M_2 is proportional to area A. As for M_k $(k > 2)$, the geometric interpretations are not obvious, but further discussion can be found in [20].

For such a single qubit control problem, if it allows multi-axial control, then $C(t)$ is usually placed in a 3-dimensional space [21], since its tangent vector can be steered into multiple directions. More degrees of freedom for $C(t)$ is required if we are dealing with a multi-qubit system [22]. It is natural to generalize the geometric interpretations of M_1 and M_2 to higher dimensional cases: A curve $\mathbf{r}(t)$ in d-dimensional Euclidean space defines a set of Frenet-Serret basis vectors $\{\mathbf{e}_n\}$, $n = 1, ..., d$. As in the single-qubit case described above, each point along the curve $\mathbf{r}(t)$ is labeled by the evolution time t. For each value of t, the Frenet-Serret vectors form an orthonormal basis: $\mathbf{e}_m(t) \cdot \mathbf{e}_n(t) = \delta_{nm}$. The first vector, $\mathbf{e}_1(t)$, is chosen to be the tangent vector of the curve at time t: $\mathbf{e}_1(t) = \dot{\mathbf{r}}(t)$. Thus, the Frenet-Serret frame rigidly rotates with the curve as time progresses. The orthonormality condition immediately implies that $\dot{\mathbf{e}}_m \cdot \mathbf{e}_n = -\mathbf{e}_m \cdot \dot{\mathbf{e}}_n$. In the case $m = n$, it follows that $\dot{\mathbf{e}}_n \cdot \mathbf{e}_n = 0$, or in other words $\dot{\mathbf{e}}_n$ lies in a direction orthogonal to $\mathbf{e}_n$. In the case of the first vector, this direction *defines* $\mathbf{e}_2$: $\dot{\mathbf{e}}_1 = \kappa_1 \mathbf{e}_2$, where κ_1 is the magnitude of $\dot{\mathbf{e}}_1$. The time derivative of $\mathbf{e}_2$ can then be written as $\dot{\mathbf{e}}_2 = -\kappa_1 \mathbf{e}_1 + \kappa_2 \mathbf{e}_3$, where the first term is included to ensure that $\dot{\mathbf{e}}_1 \cdot \mathbf{e}_2 = -\mathbf{e}_1 \cdot \dot{\mathbf{e}}_2$ is satisfied, and where $\mathbf{e}_3$ is defined to be the component of $\dot{\mathbf{e}}_2$ that is orthogonal to both $\mathbf{e}_1$

and $\mathbf{e}_2$. Continuing on to $\dot{\mathbf{e}}_3$, etc., and following the same logic then leads to definitions of the remaining $\mathbf{e}_n$, as well as to a set of self-consistency conditions known as the Frenet-Serret equations:

$$\dot{\mathbf{e}}_n = -\kappa_{n-1}\mathbf{e}_{n-1} + \kappa_n \mathbf{e}_{n+1}, \tag{2.33}$$

where the κ_n are referred to as generalized curvatures, and $\mathbf{e}_0 = 0 = \mathbf{e}_{d+1}$. If we return to the special case of $d = 3$ dimensions, then we recognize κ_1 as the usual curvature, while κ_2 is the torsion.

2.3.2 Counteracting Time-Dependent Noise with SCQC

This subsection is partially based on the paper [2]: **Bikun Li**, Fernando A. Calderon-Vargas, Junkai Zeng and Edwin Barnes, "Designing arbitrary single-axis rotations robust against perpendicular time-dependent noise" *New Journal of Physics* 23 093032 (2021)

The purpose of this subsection is to show the connection between the filter function formalism and the geometric formalism [20], and combining them together with numerical techniques to cancel noise using a simple single-axis controlled dephasing model. We show that these smooth error-correcting pulses are equivalent to sequences of closed curves in the geometric formalism. The flexibility and efficacy of our method is demonstrated for both classical $1/f$ noise and noise modeled by a quantum bath. Moreover, our method can be used in systems with restrictive control fields like the non-negative-only control available in singlet-triplet spin qubits [66, 67].

We start with a general two-level system, coupled to an external quantum bath, with initial state $|\psi_0\rangle\langle\psi_0| \otimes \rho_B$ and Hamiltonian of the form Eq. (2.4):

$$H(t) = \frac{\Omega(t)}{2}\sigma_x \otimes \mathbb{1} + \lambda\sigma_z \otimes B + \mathbb{1} \otimes H_B \ , \tag{2.34}$$

where $\Omega(t)$ is the control field. The bounded operators B and $H_B \propto \omega_B$ act on the environment, i.e. a generic quantum bath. The coupling to the environment (λ) is assumed sufficiently small that it induces a slow coherence decay within a determined time interval $t \in [0, T]$. Here, T is the time it takes to implement a target operation $U_{\text{gate}} \equiv U(T)$, where $U(t)$ is the evolution operator generated by $H(t)$. Ideally, the target operation without noise is an x rotation of any desired angle. Note that such rotations can be combined with a single rotation about another axis to form a universal set of single-qubit gates [68, 69]. We want to determine what functions $\Omega(t)$ can implement a desired operation while suppressing the leading-order errors due to the coupling λ. To that end, it is convenient to work in the interaction picture. Thus, a similar outcome as Eq. (2.17) is written as:

$$H_I(t) = \lambda e^{i\frac{\phi(t)}{2}\sigma_x}\sigma_z e^{-i\frac{\phi(t)}{2}\sigma_x} \otimes B_I(t), \tag{2.35}$$

where $B_I(t) = e^{iH_B t} B e^{-iH_B t}$, which sometimes is simply replaced by a classical random time-dependent noise term [38, 70]. The dynamics of $B_I(t)$ is assumed to be 'slow', i.e., the Fourier transform $S(\omega)$ of the two-point noise correlation function $\langle B_I(t) B_I(0)\rangle$ should concentrate around $\omega = 0$, with a bandwidth $\omega_B \ll T^{-1}$. We are interested in suppressing the leading-order effect of noise, and so we treat the interaction Hamiltonian H_I as a perturbation. We can then perform a Magnus expansion of $U_I(T)$ similar as Eq. (2.31). Specifically, if $B_I(t)$ is time-independent $M_1(t)$ is proportional to the integral of $\sigma_z \cos\phi + \sigma_y \sin\phi$, and then a planar curve $C(t) \propto M_1(t)$ is obtained with tangent vector $(\cos\phi, \sin\phi)$ and curvature $\Omega(t) = \dot{\phi}$. When $B_I(t)$ cannot be approximated as quasi-static, its fluctuations modulate the tangent vector $(\cos\phi, \sin\phi)$, which hampers the direct application of the geometric formalism. However, by considering the average gate fidelity (cf. Eq. (2.24) and section 2.2.2),

we have

$$\begin{aligned}\mathcal{F} &= \frac{1}{2} + \frac{1}{12}\sum_{\alpha=x,y,z} \mathrm{Tr}[(\sigma_\alpha \otimes \mathbb{1})U_I(T)(\sigma_\alpha \otimes \rho_B)U_I^\dagger(T)] \\ &\approx 1 - \frac{2\lambda^2}{3}\int_0^T \mathrm{d}\tau_1 \int_0^T \mathrm{d}\tau_2 \cos[\phi(\tau_1) - \phi(\tau_2)] \left\langle B_I(\tau_1)B_I(\tau_2)\right\rangle ,\end{aligned} \tag{2.36}$$

where we have omitted higher-order ($\mathcal{O}(\lambda^3)$) terms. Here, the quantum correlator $\langle B_I(\tau_1)B_I(\tau_2)\rangle \equiv \mathrm{tr}(B_I(\tau_1)B_I(\tau_2)\rho_B)$ has a short correlation time $\sim \omega_B^{-1}$. Using the Fourier transform of the two-point correlation function, $\lambda^2 \langle B_I(\tau_1)B_I(\tau_2)\rangle = \int_{-\infty}^{\infty} \frac{\mathrm{d}\omega}{2\pi} S(\omega) e^{-i\omega(\tau_1-\tau_2)}$ (where we assume that the correlator is time local), the gate infidelity $(1-\mathcal{F})$ can be approximated as

$$1 - \mathcal{F} \approx \frac{1}{3}\int_{-\infty}^{\infty} \frac{\mathrm{d}\omega}{2\pi} S(\omega) F(\omega, T), \tag{2.37}$$

in which $F(\omega, T) \equiv |f(\omega, T)|^2 + |f(-\omega, T)|^2$ with

$$f(\omega, T) \equiv \int_0^T e^{i[\phi(\tau)-\omega\tau]}\mathrm{d}\tau, \tag{2.38}$$

is the filter function. This result can also be given by Eq. (2.29) in section 2.2.2, because we have

$$M_{zz}(\tau - \tau') = \frac{1}{2}\mathrm{tr}\left[\sigma_z e^{i\frac{\phi(\tau)-\phi(\tau')}{2}\sigma_x}(\tau - \tau')\sigma_z e^{-i\frac{\phi(\tau)-\phi(\tau')}{2}\sigma_x}\right] = \cos\left[\phi(\tau) - \phi(\tau')\right] . \tag{2.39}$$

Note that the filter function in Eq. (2.37) encapsulates only the lowest-order nontrivial effect of the control field on the gate infidelity in an ever-changing noisy environment, whereas for Gaussian noise the filter function gives an exact representation [38]. In order to minimize Eq. (2.37), we need to make the filter function, $F(\omega, T)$, as small as possible at frequencies where $S(\omega)$ is maximal. Hereafter, we consider the case where the noise power spectrum has its maximum at $\omega_0 = 0$, but it can be easily generalized to a non-zero ω_0.

Minimizing the filter function implies the minimization of $f(\omega, T)$, Eq. (2.38), i.e. making

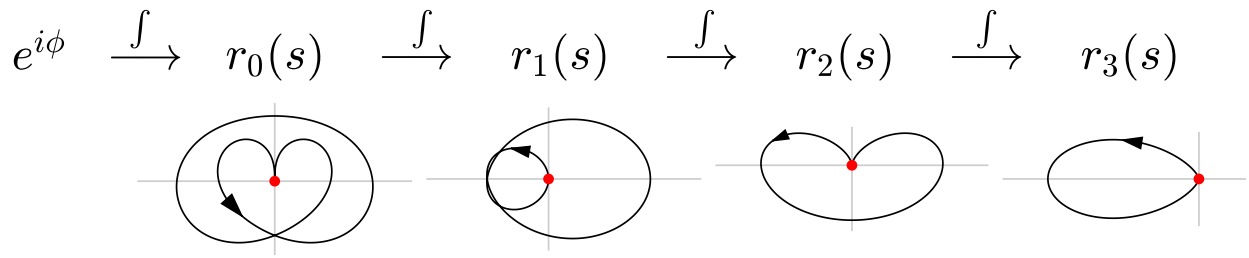

Figure 2.2: An illustration of a sequence of closed curves $\{r_m\}$, where the red dots represent the starting and ending points of each curve. Each curve in the sequence is obtained by integrating the previous. $r_0(s)$ is given by the integral of $e^{i\phi(Ts)}$. In this example, the integral of $r_3(s)$ is no longer a closed curve, so the sequence terminates and thus contains four curves in total (This figure is adapted from [2].)

$f(\omega, T)$ as small as $\mathcal{O}(\omega^k T^{k+1})$ around $\omega = 0$, where k is a positive integer. To this end, we want the first k-th derivatives of $f(\omega, T)$ to vanish at the origin:

$$\begin{aligned} 0 &= (i\partial_{\omega T})^\ell [T^{-1} f(\omega, T)]_{\omega T=0} \\ &= \int_0^1 s^\ell e^{i\phi(Ts)} \mathrm{d}s = \sum_{m=0}^{\ell} \frac{(-1)^m \ell!}{(\ell - m)!} r_m(1), \end{aligned} \tag{2.40}$$

with $0 \leq \ell < k$. The third equality is obtained via integration by parts, where $r_m(s)$ $(0 \leq s \leq 1)$ is a complex function defined as

$$r_m(s) = \int_0^{s_0} \mathrm{d}s_1 \int_0^{s_1} \mathrm{d}s_2 \cdots \int_0^{s_m} \mathrm{d}s_{m+1} e^{i\phi(Ts_{m+1})}, \tag{2.41}$$

where $s_0 \equiv s$. All $r_m(s)$ are required to be zero at $s = 1$ in order to fulfill Eq. (2.40). This expression motivates introducing a modified version of the geometric formalism in which we treat each $r_m(s)$ in Eq. (2.41) as a closed curve on a complex plane (see Fig. 2.2). The filter function $F \sim |f|^2$ is suppressed up to order $\mathcal{O}(\omega^{2k} T^{2k+2})$ about $\omega = 0$ if and only if the k curves in this sequence are all closed. Thus, requiring the integrals in Eq. (2.41) to vanish can be viewed as an extension of the closed curve argument for quasi-static noise [20], which simply requires that the first integral $(m = 0)$ vanishes. Notice that the curves in

this sequence are all related through differentiation: $r'_\ell(s) = r_{\ell-1}(s)$. Therefore, the task of finding pulses that implement gates while canceling low-frequency noise to order $\mathcal{O}(\omega^{2k}T^{2k+2})$ is equivalent to finding a closed curve $r_{k-1}(s)$ such that its first $k-1$ derivatives are also themselves closed curves. In addition to being closed, the last curve obtained from this sequence of derivatives, $r_0(s)$, must also have the property that $|r'_0(s)| = 1$, since $r_0(s)$ is supposed to be the integral of the phase $e^{i\phi}$ (see Eq. (2.41)). If such a sequence of closed curves can be found, then a robust pulse can be obtained from the curvature of r_0. Moreover, a desired target rotation can be obtained by designing the hierarchy such that r_0 exhibits a cusp at the origin. The opening angle of this cusp determines the rotation angle θ about the x-axis [20]. For arbitrary k, it is not a simple task to find such curve sequences. While it is relatively straightforward to find closed curves $r_{k-1}(s)$ such that the first $k-1$ derivatives are also closed, it is more challenging to design $r_{k-1}(s)$ such that $|r'_0(s)| = 1$ is satisfied. In the next section, we show how this problem can be circumvented by parameterizing $\phi(t)$ appropriately and using a numerical recipe to obtain control fields that suppress low-frequency noise to arbitrary order k.

In [2], we develop a numerical method to obtain pulses that satisfy the closed-curve constraints in Eqs. (2.40) and (2.41). We start by setting $x = 2s - 1$ and combining terms in Eq. (2.40), which converts the error-cancellation constraints into a more convenient form: $\eta_\ell = \int_{-1}^{1} x^\ell e^{i\phi[T(x+1)/2]}\mathrm{d}x = 0$, with $0 \leq \ell < k$. Now, the key ansatz of this work is to treat the target rotation as an odd polynomial with N unknown coefficients:

$$\phi\big[T(x+1)/2\big] = p_1 x + p_3 x^3 + \cdots + p_{2N-1}x^{2N-1}. \tag{2.42}$$

The advantage of this ansatz is twofold: first, the control field $\Omega(t)$ is symmetric about $t = T/2$, which makes η_ℓ a real function of the p_i up to a global phase, and second, there is a recursive derivative relation, $\partial\eta_\ell/\partial p_{2j-1} = i\eta_{\ell+2j-1}$, that is useful in what follows. The

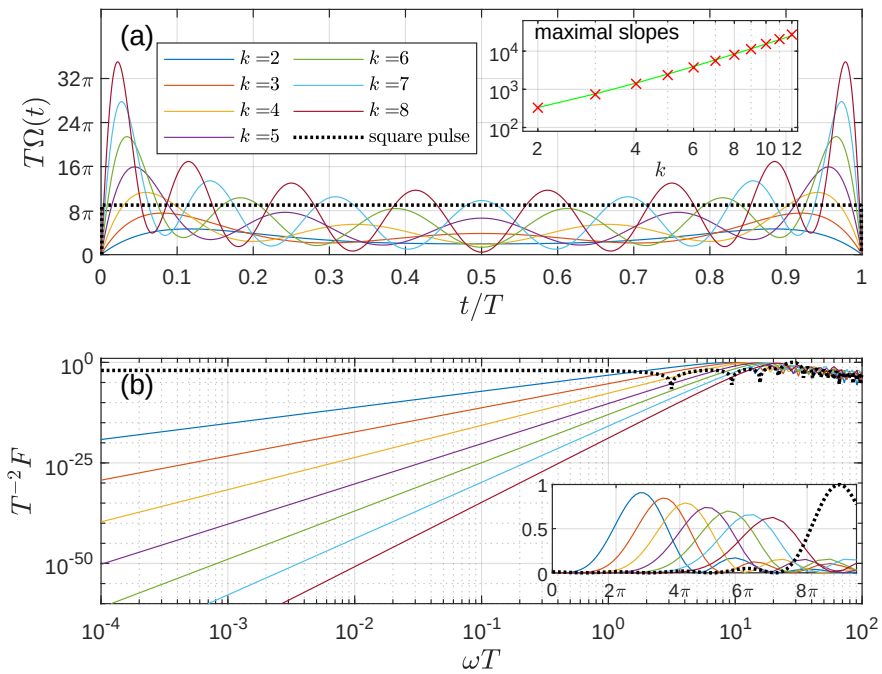

Figure 2.3: (a) Seven control pulses (colored lines) that achieve $T^{-1}f(\omega,T) = \mathcal{O}(\omega^k T^k)$ noise cancellation. The kth pulse implements an x-rotation by angle $(k+1)\pi$. A square pulse that achieves a 9π rotation (black dotted line) is shown for comparison. The inset shows the maximum slopes (bandwidths) that are required for different k. These exhibit a $\sim k^3$ dependence at small k (green line). (b) The filter functions for the control pulses in (a) (colored lines). The asymptotic slopes of the filter functions are $\approx 2k$, indicating the $\mathcal{O}(\omega^{2k}T^{2k+2})$ suppression near $\omega T = 0$. The inset shows the same filter functions on a linear scale. (This figure is adapted from [2].)

pulses should implement arbitrary X_θ gates in a time frame $0 < t < T$ and, therefore, ϕ must satisfy the boundary conditions $\phi|_{x=1} = \theta/2$ and $\partial_x\phi|_{x=1} = 0$. In total, we therefore have $k+2$ real functions involving p_{2j-1} unknowns:

$$
\begin{aligned}
G_\ell &= i^{\ell-1}\eta_{\ell-1}, \quad \text{with} \quad 1 \le \ell \le k \\
G_{k+1} &= \left(\sum_{j=1}^{N} p_{2j-1}\right) - \frac{\theta}{2}, \\
G_{k+2} &= \sum_{j=1}^{N} (2j-1)p_{2j-1},
\end{aligned}
\tag{2.43}
$$

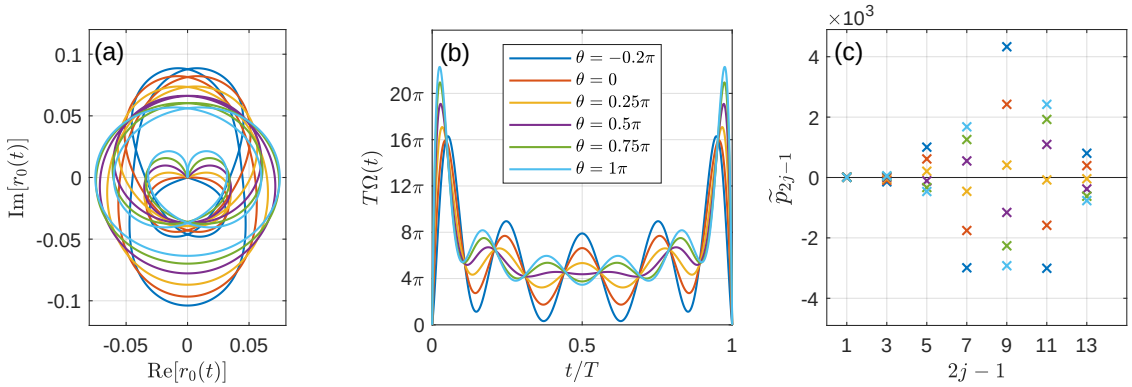

Figure 2.4: (a) Closed curves $r_0(t)$ that generate a hierarchy of closed curves $r_k(t)$ up to $r_4(t)$ (see e.g., Fig. 2.2). The opening angles of the cusps at the origin determine the rotation angles θ. (b) Pulses that implement x-rotations of various angles with $k = 5$ time-dependent noise suppression. (c) The polynomial coefficients that define the control pulses shown in (b).

which are all required to vanish. Notice that by setting $N = k + 2$, the numerical solutions can be obtained efficiently through iteration (damped Newton method):

$$p_{2j-1}^{(n+1)} = p_{2j-1}^{(n)} - \alpha \sum_{m=1}^{N} [J(p^{(n)})]_{j,m}^{-1} G_m(p^{(n)}), \tag{2.44}$$

where $0 < \alpha \leq 1$ is the damping parameter, and J is the non-singular Jacobian (square) matrix $J_{\ell,j} = \partial G_\ell / \partial p_{2j-1}$, which can be easily evaluated via the aforementioned recursive derivative relation, $\partial \eta_\ell / \partial p_{2j-1} = i\eta_{\ell+2j-1}$. Now, if a proper value for α is chosen and the initial guess for $p^{(0)}$ is suitable, then after some number of iterations the term $\|G_m(p^{(n_f)})\|$ will inevitably fall under a predefined convergence threshold ϵ, signaling that the concomitant $\widetilde{p}_{2j-1} \equiv p_{2j-1}^{(n_f)}$ is a valid solution. The control pulse is then finally given by $\Omega(\tau) = \partial_\tau \phi(\tau)|_{p=\widetilde{p}}$, which is a polynomial of degree $2k + 2$.

With the numerical scheme introduced above, one can easily obtain solutions for different sets of parameters. Even though we have extensively explored the solution space, here we focus on solutions that are obtained from the initial values $p_j^{(0)} = \delta_{1j}[(k+1)\pi + \theta]/2$, which

correspond to a square pulse. Choosing $k \leq 5$, $\alpha = 1$, and threshold $\epsilon = 10^{-30}$, iteration of Eq. (2.44) converges to valid solutions within 100 steps. For k larger than 5, we find that the damping parameter α must be reduced to obtain suitable solutions. Overall, these types of solutions converge into non-negative control pulses, which are important for qubit systems with constrained control like singlet-triplet qubits [66, 67]. Fig. 2.3(a) shows several non-negative control pulses obtained with $\theta = (k+1)\pi$ and $2 \leq k \leq 8$. The inset of Fig. 2.3(a) presents, as a function of k, the maximal slopes of the pulses, which are related to the maximum bandwidth needed to implement them with a waveform generator. Their rate of change is proportional to $\sim k^3$. Fig. 2.3(b) and its inset present the filter functions, on both logarithmic and linear scales, of the control pulses presented in Fig. 2.3(a). Note that the asymptotic slopes of the filter functions are approximately equal to $2k$, which indicates the suppression of $\mathcal{O}(\omega^{2k}T^{2k+2})$ terms near $\omega T = 0$. Finally, Fig. 2.4 showcases the flexibility of our scheme in producing arbitrary x-rotations. Setting $k = 5$, we repeat the above iterative procedure to obtain noise-suppressing pulses for a range of rotation angles θ. In Fig. 2.4(a), we show the resulting set of curves $r_0(t)$, from which the pulses in Fig. 2.4(b) can be obtained from the curvatures. Each of these curves is at the bottom of a closed curve hierarchy that starts at the top with $r_4(t)$, analogous to what is shown in Fig. 2.2 for $k = 3$. Fig. 2.4(b) also shows that the pulses remain non-negative across a wide range of rotation angles θ. The parameters $\tilde{p}_{2j-1}$ used to construct these curves and pulses are given in Fig. 2.4(c).

We must point out that although with our method one can find solutions for a wide range of parameters, the solution space is rather complicated due to the nonlinear form of the equations in (2.43). Moreover, as k increases, it becomes more difficult to obtain good solutions even after setting the damping parameter to $\alpha < 10^{-2}$. This is partly because the Jacobian matrix becomes almost singular for large k, which in turn requires an increase in precision to retain accuracy in the calculations. In experimental implementations, the value

of k that is chosen will ultimately be determined by bandwidth limitations of waveform generators. This is because larger values of k require pulses with faster rise times, as is evident from Fig. 2.3(a). In practice, there is thus a tradeoff between cancelling higher-order environmental noise and maintaining pulse accuracy, which is also necessary for achieving high gate fidelities. The effect of pulse errors is considered further in the next section.

2.3.2.1 Numerical Simulations

We have shown, so far, that smooth continuous control pulses can be designed to perform arbitrary x-rotations and, at the same time, shield the system from time-dependent noise. In this section we characterize the performance of the smooth control pulses against realistic noise power spectra. To this end, we calculate the gate infidelity in the presence of, first, a random quantum bath and, then, a classical $1/f^{\alpha}$ noise source.

Virtual Random Quantum Bath. Since the actual environment surrounding the qubit system is usually a complicated many body quantum system, we use a bounded operator (m-levels) to simulate the quantum bath. Therefore, we take two independent $m \times m$ random matrices W_1, W_2 from a Gaussian unitary ensemble and use them to define the bounded operators $B = W_1/\sqrt{m}$ and $H_B = \omega_B W_2/\sqrt{m}$, where the bath density operator is $\rho_B \propto e^{-\beta H_B}$. Regardless of the complicated dynamics of $B_I(t)$, the statistical property of the noise power spectrum has an analytic form in the thermodynamic limit $m \to \infty$ (see section 2.3.2.2):

$$S(\omega) = \frac{2\pi\lambda^2}{Z\omega_B} \int_{-\infty}^{\infty} p(u)p(u - \omega/\omega_B)e^{-\beta\omega_B u}\mathrm{d}u, \tag{2.45}$$

where $p(u) = (2\pi)^{-1}\sqrt{4-u^2}$ with $|u| < 2$, and $p(u) = 0$ with $|u| \geq 2$ are given by *Wigner's semicircle law.* $Z \equiv \int_{-2}^{2} \mathrm{d}\lambda p(\lambda)e^{-\beta\omega_B\lambda}$ is a normalization factor. Due to the piecewise $p(\omega)$ distribution, there are hard high-frequency cutoffs at $\omega = \pm 4\omega_B$.

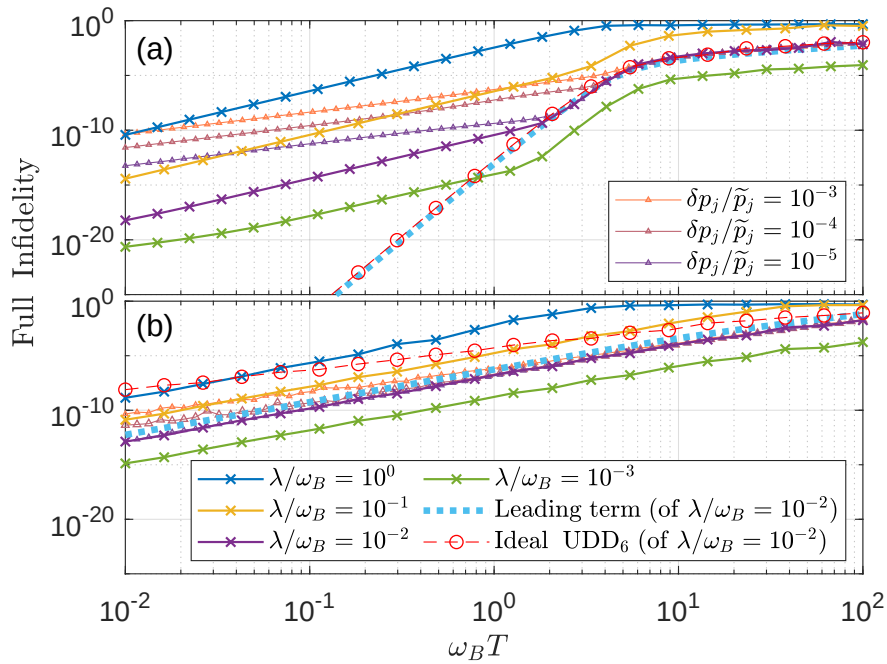

Figure 2.5: The full infidelities of the pulse with $k = 6$ for (a) a virtual random quantum bath, and (b) classical noise $\eta(t)$ with a soft high-frequency cutoff. Each curve is plotted with varying control gate time T, but fixed ω_B and λ/ω_B. The dashed curve shows the leading-order contribution of the infidelity for $\lambda/\omega_B = 10^{-2}$, which has an asymptotic slope $2k + 2 = 14$. The target operation is chosen to be an identity gate ($\theta = 8\pi$) so that we can compare with the Uhrig dynamical decoupling sequence (UDD$_6$) [3], which is also included in the figure. Results that include errors in $\Omega(t)$ are also displayed by data points with triangles (with coupling $\lambda/\omega_B = 10^{-2}$), where $\widetilde{p}_j$ is implemented with small fluctuations, whose standard deviation is δp_j. (This figure is adapted from [2].)

In Fig. 2.5(a), the results with infinite temperature ($\beta = 0$) are computed for the $k = 6$ pulse presented in Fig. 2.3, where full infidelities (including all orders of the bath coupling) are presented together with the leading infidelity term, Eq. (2.37). According to dimensional analysis, each term in the expansion of the infidelity has the form: $\propto \lambda^\nu T^\mu \omega_B^{\mu-\nu} (\nu \geq 2)$; our leading term, Eq. (2.37), only involves terms with $\nu = 2$, and $\mu \geq 2k + 2$ due to our optimized filter function $\mathcal{O}(\omega^{2k} T^{2k+2})$. As a result, these $\nu = 2$ terms dominate when $\lambda/\omega_B \ll 1$ and $T \gg \omega_B^{-1}$. One can clearly see in Fig. 2.5(a) that in the region $T > \omega_B^{-1}$, the full infidelity closely follows Eq. (2.37). On the other hand, the leading-order expression deviates sharply from the full fidelity when $T \ll \omega_B^{-1}$, reflecting the fact that higher-order

noise terms dominate in this regime. Although our shaped pulse is not designed to suppress these errors, the fidelity remains high because these terms are very small. These findings thus confirm the validity of truncating the Magnus expansion to facilitate the design of robust pulses.

These trends persist when the pulse $\Omega(t)$ is not accurately implemented. We can study the effect of pulse errors by including fluctuations δp_j in the solutions for the pulse parameters $\tilde{p}_j$. As we can see from Fig. 2.5(a), pulse errors of 0.1% or less have essentially no effect on the fidelity in the region $T > \omega_B^{-1}$ where the $\nu = 2$ terms dominate. Although pulse errors have a stronger effect for smaller gate time T, the infidelity still remains very low due to the overall low-T suppression. However, if the pulse errors are significantly larger than 0.1%, the performance becomes significantly worse. This is due both to the presence of the additional noise source and to the fact that pulse errors will cause the closed-curve condition to be violated, weakening the suppression of environmental noise errors. This is consistent with previous studies on continuous dynamical decoupling that found a heightened sensitivity to driving field noise [71].

Classical $1/f^\alpha$ ***Noise.*** In almost all solid-state qubit platforms, fluctuations of various system parameters characterized by a $1/f$ power spectral density have been observed. Here, we consider a $1/f^\alpha$ power spectral density that remains nonzero in the high-frequency domain. To efficiently simulate the soft high-frequency cutoff of the noise power spectrum, we replace $B_I(t)$ with a real stochastic function $\eta(t)$. The stochastic noise is then constructed from a set of independent random telegraph noise (RTN) sources: $\eta(t) = C\int_{\nu_a}^{\nu_b} \nu_0^{-1/2}\eta_0(t,\nu_0)\mathrm{d}\nu_0$, where $\eta_0(t,\nu_0)$ describes a single RTN that switches between ± 1 with frequency ν_0. Here $C^2 = 1/\log(\nu_b/\nu_a)$ is a normalizing factor such that $\overline{\eta(t)^2} = 1$, and the integrand weight

$\nu_0^{-1/2}$ yields a desired noise power spectrum:

$$S(\omega) = \frac{2\lambda^2 C^2}{\omega}\left[\arctan\left(\frac{2\nu_b}{\omega}\right) - \arctan\left(\frac{2\nu_a}{\omega}\right)\right] . \tag{2.46}$$

For $0 < \omega \ll \nu_a$, $S(\omega) \propto$ constant; for $\nu_a \ll \omega \ll \nu_b$, $S(\omega) \propto 1/\omega$; for $\omega \gg \nu_b$, $S(\omega) \propto 1/\omega^2$. In our simulation, we simply set $\nu_b = 100\nu_a = \omega_B$, and thus $S(\omega)$ has a soft high-frequency cutoff. It is evident that our filter function cannot effectively filtrate the 'long tail' of $S(\omega)$, and no decoupling technique can do so as established by the no-go theorem in Ref. [70]. Specifically, following the previous argument about the infidelity expansion, the leading terms $\lambda^2 T^\mu \omega_B^{\mu-2}$ can have a small μ, due to the integral $\int_{\omega_B}^{\infty} S(\omega)F(\omega,T)\mathrm{d}\omega$ being nonzero in the soft-cutoff case. Therefore, the full infidelity does not experience a $\mathcal{O}(T^{2k+2})$ suppression for any $\omega_B T$. This in turn means that including pulse errors at the 0.1% level has only a very small effect on the fidelity across all values of T, as shown in Fig. 2.5(b). Despite the absence of a low-T suppression, which is a consequence of the long high-frequency tail in the noise power spectrum in this case, as is evident from the figure, our smooth pulse ($k = 6$) outperforms the ideal UDD_6 at small $\omega_B T$. This is due to the always-on nature of our pulse, which constantly suppresses the time-dependent perturbation.

2.3.2.2 Supplement: Derivation of Eq. (2.45)

Suppose our virtual random quantum bath has m levels ($m \gg 1$), and the coupling operator and the Hamiltonian are separately given by $B = W_1/\sqrt{m}$ and $H_B = \omega_B W_2/\sqrt{m}$, where W_1, W_2 are random matrices sampled from Gaussian unitary ensemble (GUE). In this case, the density of eigenvalues λ distribution of $W_i/\sqrt{m}$ is given by Wigner's semi-circle law $p(\lambda) = (2\pi)^{-1}\sqrt{4-\lambda^2}$ with $\lambda^2 \leq 4$, and $p(\lambda) = 0$ for otherwise λ. Therefore, assume the quantum bath is in equilibrium with density operator $\rho_B = e^{-\beta H_B}/Z$, the power spectrum

density for particular instance of B and H_B is:

$$\begin{aligned} S(\omega) &= \frac{\lambda^2}{Z}\int_{-\infty}^{\infty}\mathrm{tr}[e^{iH_Bt}Be^{-iH_Bt-\beta H_B}B]e^{-i\omega t}\mathrm{d}t \\ &= \frac{\lambda^2}{Z}\sum_{k,\ell=1}^{m}\int_{-\infty}^{\infty}|B_{k\ell}|^2 e^{i\omega_B(\lambda_k-\lambda_\ell)t-\beta\omega_B\lambda_\ell}e^{-i\omega t}\mathrm{d}t \\ &= \frac{2\pi\lambda^2}{\omega_B Z}\sum_{k,\ell=1}^{m}|B_{k\ell}|^2 e^{-\beta\omega_B\lambda_\ell}\delta\Big(\lambda_k-\lambda_\ell-\frac{\omega}{\omega_B}\Big) \end{aligned} \tag{2.47}$$

In which we obtain the second equal sign via taking the trace under the eigenvector basis of H_B, and $B_{k\ell}$ are the matrix entries under this basis. Finally, utilizing $\overline{|B_{k\ell}|^2} = \overline{|(W_1)_{k\ell}|^2}/m = 1$ and *Wigner's semicircle law* [164], the statistical average of $S(\omega)$ given by:

$$\begin{aligned} \overline{S(\omega)} &= \frac{2\pi\lambda^2}{\omega_B Z}\int_{-\infty}^{\infty}\mathrm{d}\lambda'\int_{-\infty}^{\infty}\mathrm{d}\lambda\; p(\lambda')p(\lambda) \\ &\qquad\times e^{-\beta\omega_B\lambda}\delta\Big(\lambda_k-\lambda_\ell-\frac{\omega}{\omega_B}\Big) \\ &= \frac{2\pi\lambda^2}{\omega_B Z}\int\mathrm{d}\lambda\; p(\lambda)p\Big(\lambda-\frac{\omega}{\omega_B}\Big)e^{-\beta\omega_B\lambda} \end{aligned} \tag{2.48}$$

where the normalizing factor is $Z \equiv \int_{-2}^{2}\mathrm{d}\lambda p(\lambda)e^{-\beta\omega_B\lambda}$ under thermodynamics limit. The hard cut-off property of $p(\lambda)$ indicates $S(\omega)$ statistically vanishes at $|\omega| \geq 4\omega_B$.

2.4 Time Optimal Control with SCQC

In control theory, the optimization problem is always an attractive topic for real applications. Researchers often focus on problem-specific cost functions, such as fuel consumption of a spacecraft, or profit gain during stock trading. When we are dealing with quantum engineering problems where coherence is a resource, control time is a candidate cost function [72]. The control strategy that minimizes or maximizes a cost function is preferred due to its

superior performance. Optimal control theory is a mature field that has been under devolopment since the last century. There is a vast literature on this subject, so it is challenging to show the whole picture. In this section, we will briefly introduce how the Pontryagin minimum principle[7] (PMP) can deal with free-time and fixed-end problems in section 2.4.1, which is a particular category that suits the DECG design. Section 2.4.2 gives an analytical derivation of the shortest planar closed path with bounded curvature, which recovers the result in [19] in an alternative way. Section 2.4.3 displays some preliminary exploration of solving optimized bounded controls with a physics-informed neural network.

2.4.1 PMP for Free-time and Fixed-End Problem

Suppose we describe the state of a system by $\mathbf{x} \in \mathbb{R}^n$, for which dynamics is governed by

$$\dot{\mathbf{x}}(t) = \mathbf{f}(\mathbf{x}, \mathbf{u}) \quad (0 \leq t \leq T) \tag{2.49}$$

with initial condition $\mathbf{x}(0) = \mathbf{x}_0$, and final condition $\mathbf{x}(T) = \mathbf{x}_f$, T is an undetermined smallest time such that $\mathbf{x}(T)$ hits $\mathbf{x}_f$ for the first time. Additionally, $\mathbf{u} \in \mathcal{U}$ is the control function, where $\mathcal{U}$ is the set of *admissible controls* [73]. Normally, the functions in $\mathcal{U}$ are bounded by some maximum and minimum throughout $[0, T]$. Yet, mathematically, $\mathbf{u} \in \mathcal{U}$ is not necessarily continuous —- a measure-zero subset $\omega \subset [0, T]$ of exceptions is allowed, which differentiates control theory problems from regular variational problems. Under the above dynamical system, we wish to *minimize* the following objective function:

$$J[\mathbf{u}] = K(\mathbf{x}(T)) + \int_0^T L(\mathbf{x}, \mathbf{u}) \mathrm{d}t \ , \tag{2.50}$$

[7] In some context, we call it Pontryagin maximum principle, the only difference is flipping the sign of cost function.

in which K is the terminal payoff and the second integral term is the running payoff. As this section focuses on the fixed-end problem, $K(\cdot)$ is a constant cost that can be ignored.

Let $\mathbf{u}^*(t) \in \mathcal{U}$ $(0 \leq t \leq T)$ be an (globally) optimal control and $\mathbf{x}^*(t) \in \mathbb{R}^n$ be the corresponding optimal state trajectory. Then there exists a function $\mathbf{p}^*(t) \in \mathbb{R}^n$ (costate) and a constant (abnormal multiplier) $p_0^* \leq 0$ satisfying $(\mathbf{p}, p_0) \neq (0, 0)$, $\forall 0 \leq t \leq T$ and having the following properties (Also see Theorem 5 of [73] for a rigorous description):

(1) The optimal state and costate satisfy canonical equations:

$$\begin{cases} \dot{\mathbf{x}}^* = \nabla_{\mathbf{p}} H_P(\mathbf{x}^*, \mathbf{u}^*, \mathbf{p}^*, p_0^*) = \mathbf{f}(\mathbf{x}^*, \mathbf{u}^*) \\ \dot{\mathbf{p}}^* = -\nabla_{\mathbf{x}} H_P(\mathbf{x}^*, \mathbf{u}^*, \mathbf{p}^*, p_0^*) \end{cases}, \tag{2.51}$$

where H_P is the (pseudo-)Hamiltonian, defined as:

$$H_P(\mathbf{x}, \mathbf{u}, \mathbf{p}, p_0) = \mathbf{p} \cdot \mathbf{f}(\mathbf{x}, \mathbf{u}) + p_0 L(\mathbf{x}, \mathbf{u}) \ . \tag{2.52}$$

(2) For each fixed t, $H_P(\mathbf{x}^*(t), \mathbf{u}, \mathbf{p}^*(t), p_0^*)$ has a *global maximum* at $\mathbf{u} = \mathbf{u}^*(t)$:

$$H_P(\mathbf{x}^*(t), \mathbf{u}^*, \mathbf{p}^*(t), p_0^*) \geq H_P(\mathbf{x}^*(t), \mathbf{u}, \mathbf{p}^*(t), p_0^*) \quad \forall 0 \leq t \leq T, \ u \in \mathcal{U} \ . \tag{2.53}$$

(3) The optimal Hamiltonian is constantly zero:

$$H_P(\mathbf{x}^*(t), \mathbf{u}^*(t), \mathbf{p}^*(t), p_0^*) = 0, \quad \forall 0 \leq t \leq T \ . \tag{2.54}$$

This section mainly focuses on the case of *minimizing* the control time T, which means we can set:

$$L(\mathbf{x}, \mathbf{u}) \equiv 1, \qquad p_0^* = -1 \tag{2.55}$$

These above necessary conditions are known as the conditions for PMP, but they are only feasible for free-time and fixed-end problems. For other boundary constraints (e.g. fixed-time and free-end problems), and the mechanism/proof behind PMP, please look up Chapter 3 and 4 of [74] for more details.

2.4.2 Demonstration of Deriving 2D Dubins Curve

There are many illuminating examples [74] that exemplify how to use PMP. This dissertation provides an analytical solution closely related to quantum control —- the shortest closed path on a 2D plane, which is also known as a Dubins curve [75].

In this subsection, we are using PMP to study the optimization problem in [19]. The trajectory $\mathbf{x}(t)$ here is a planar curve $(x(t), y(t))$, with (unit) tangent vector $(v_x(t), v_y(t))$ steered by $\Omega(t)$:

$$\dot{\mathbf{x}}(t) = \frac{\mathrm{d}}{\mathrm{d}t}\begin{bmatrix} x(t) \\ y(t) \\ v_x(t) \\ v_y(t) \end{bmatrix} = \mathbf{f}(\mathbf{x}, \Omega) = \begin{bmatrix} v_x(t) \\ v_y(t) \\ -\Omega(t)v_y(t) \\ +\Omega(t)v_x(t) \end{bmatrix} . \tag{2.56}$$

We try to minimize the curve length $\int_0^T 1\mathrm{d}T$ under confined control field $\Omega(t) \in [-1, 1]$. Since we need a closed curve with proper initial and final tangent vectors, the initial conditions and final conditions are written as:

$$\mathbf{x}(0) = (0, 0, 1, 0)^T, \qquad \mathbf{x}(T) = (0, 0, \cos\theta, \sin\theta)^T . \tag{2.57}$$

in which θ is a constant that gives target rotation $U_{\text{gate}} = e^{-i\frac{\theta}{2}\sigma_x}$. The pseudo-Hamiltonian

Eq. (2.52) is written as:

$$H_P = v_x p_1 + v_y p_2 + \Omega \cdot [v_x p_4 - v_y p_3] - 1 \ , \tag{2.58}$$

then we can apply properties (1,2,3) in the previous section: Using property (1) in section 2.4.1, the state solutions are given by:

$$x^*(t) = \int_0^t v_x^*(s)\mathrm{d}s, \qquad y^*(t) = \int_0^t v_y^*(s)\mathrm{d}s, \qquad \begin{bmatrix} v_x^*(t) \\ v_y^*(t) \end{bmatrix} = R(t) \begin{bmatrix} 1 \\ 0 \end{bmatrix} \ , \tag{2.59}$$

where

$$R(t) := \begin{bmatrix} \cos\Phi(t) & -\sin\Phi(t) \\ \sin\Phi(t) & \cos\Phi(t) \end{bmatrix} \qquad \Phi(t) = \int_0^t \Omega^*(s)\mathrm{d}s \ . \tag{2.60}$$

On the other hand, the costate equations and solutions are given by:

$$\begin{cases} \dot{p}_1^* = 0, \quad \dot{p}_2^* = 0 \\ \begin{bmatrix} \dot{p}_3^* \\ \dot{p}_4^* \end{bmatrix} = \Omega^* \begin{bmatrix} -p_4^* \\ p_3^* \end{bmatrix} - \begin{bmatrix} p_1^* \\ p_2^* \end{bmatrix} \end{cases} \Rightarrow \begin{cases} p_1^* = c_1, \quad p_2^* = c_2 \\ \begin{bmatrix} p_3^*(t) \\ p_4^*(t) \end{bmatrix} = R(t) \begin{bmatrix} c_3 \\ c_4 \end{bmatrix} - \left[R(t) \int_0^t R(s)^{-1}\mathrm{d}s \right] \begin{bmatrix} c_1 \\ c_2 \end{bmatrix} \end{cases} \tag{2.61}$$

where c_1, c_2, c_3, c_4 are undetermined constants.

Using property (2): If we are fortunate enough to *avoid* the singular case[8], where $v_x^* p_4^* - v_y^* p_3^*$ vanishes in a measurable subset of $[0, T]$, then the $\Omega^*(t)$ that maximizes $H_P(\mathbf{x}^*, \Omega, \mathbf{p}^*, -1)$ is

$$\Omega^*(t) = \mathrm{sgn}\left[v_x^*(t)p_4^*(t) - v_y^*(t)p_3^*(t)\right] = \mathrm{sgn}[-x^*(t)c_2 + y^*(t)c_1 + c_4] \ , \tag{2.62}$$

which means the sign switching of $v_x^* p_4^* - v_y^* p_3^*$ determines the value switching of $\Omega(t)$. For

[8]Normally, it is not a priori knowledge.

this reason, when the pseudo-Hamiltonian H_P is a linear function of $\Omega(t)$, the factor of $\Omega(t)$ is known as the switching function.

Before we move on, let us perform a sanity check for PMP: We verify that $H_P|_*$ stays as a constant when $\Omega^*(t)$ stays as a constant. Let control field $\Omega^*(t) = \Omega_0$ be a constant within $t_1 \leq t \leq t_2$, we have

$$v_x^* p_1^* + v_y^* p_2^* = \begin{bmatrix} v_x^*(t_1) & v_y^*(t_1) \end{bmatrix} \begin{bmatrix} c & s \\ -s & c \end{bmatrix} \begin{bmatrix} c_1 \\ c_2 \end{bmatrix} ,$$

$$\begin{aligned} v_x^* p_4^* - v_y^* p_3^* &= \begin{bmatrix} -v_y^*(0) & v_x^*(0) \end{bmatrix} \left\{ \begin{bmatrix} c_3 \\ c_4 \end{bmatrix} - \left(\int_0^{t_1} + \int_{t_1}^{t} \right) R^{-1}(s) \mathrm{d}s \begin{bmatrix} c_1 \\ c_2 \end{bmatrix} \right\} \\ &= \begin{bmatrix} -v_y^*(t_1) & v_x^*(t_1) \end{bmatrix} \left\{ R(t_1) \begin{bmatrix} c_3 \\ c_4 \end{bmatrix} - \left(R(t_1) \int_0^{t_1} R^{-1}(s) \mathrm{d}s + \frac{1}{\Omega_0} \begin{bmatrix} s & -c+1 \\ c-1 & s \end{bmatrix} \right) \begin{bmatrix} c_1 \\ c_2 \end{bmatrix} \right\} , \end{aligned}$$

in which $c \equiv \cos[\Omega_0 \cdot (t - t_1)]$, $s \equiv \sin[\Omega_0 \cdot (t - t_1)]$ $(t_1 \leq t \leq t_2)$. Plugging them into Eq. (2.58), one can see the variable t is eliminated in the Hamiltonian:

$$\begin{aligned} H_P|_*(t) = \Omega_0 \begin{bmatrix} -v_y^*(0) & v_x^*(0) \end{bmatrix} \left(\begin{bmatrix} c_3 \\ c_4 \end{bmatrix} - \int_0^{t_1} R^{-1}(s) \mathrm{d}s \begin{bmatrix} c_1 \\ c_2 \end{bmatrix} \right) \\ + [c_1 v_x^*(t_1) + c_2 v_y^*(t_1)] - 1 = H_P|_*(t_1) . \end{aligned}$$

Similarly, we can also continue to verify that $\frac{\partial}{\partial t_1} H_P|_*(t_1) = 0$ from the above equation.

Using property (3): With $(x^*(T) - x^*(0), y(T)^* - y^*(0)) = 0 \Rightarrow \int_0^T R^{-1}(s) \mathrm{d}s = 0$, we must have

$$\begin{aligned} H_P|_*(0) &= \Omega^*(0) c_4 + c_1 v_x^*(0) + c_2 v_y^*(0) - 1 = 0 , \\ H_P|_*(T) &= \Omega^*(T) c_4 + c_1 v_x^*(T) + c_2 v_y^*(T) - 1 = 0 . \end{aligned} \tag{2.63}$$

With the outcome of Eq. (2.62): $\Omega^*(0) = \Omega^*(T) = \mathrm{sgn}(c_4)$, subtracting the equations in Eq. (2.63) gives:

$$\begin{bmatrix} c_1 & c_2 \end{bmatrix} \begin{bmatrix} v_x^*(T) - v_x^*(0) \\ v_y^*(T) - v_y^*(0) \end{bmatrix} = 0 \;\Rightarrow\; \begin{bmatrix} c_1 & c_2 \end{bmatrix} = C \begin{bmatrix} \cos\frac{\theta}{2} & \sin\frac{\theta}{2} \end{bmatrix} \quad C = \mathrm{const}\ . \tag{2.64}$$

Denote $t_1 \in [0, T]$ as the moment when Ω^* switches from ± 1 to ∓ 1 for the first time. From Eq. (2.62), we obtain a line ℓ on the x-y plane for such control field switching (as shown in Fig. 2.6):

$$\ell: \quad -xC\sin\frac{\theta}{2} + yC\cos\frac{\theta}{2} + c_4 = 0\ , \tag{2.65}$$

which divides the x-y plane into two domains, the trajectory curve $(x^*(t), y^*(t))$ (blue) as shown in Fig. 2.6 has to take maximum curvature $+1$ in one domain and minimum curvature -1 in another. $\Omega^*(t)$ will maintain its value[9] in when (x^*, y^*) is staying in one domain until it cross line ℓ. As displayed in Fig. 2.6, these conditions tell us that the solution of the trajectory must be some continuously concatenated arcs. Therefore, c_4 can be determined in terms of θ by geometric relations. Observe that from Eq. (2.64), we can simply set $C = 1$, then $c_1 = \cos\frac{\theta}{2}$, $c_2 = \sin\frac{\theta}{2}$, and c_4 is merely the distance from the origin to line ℓ, from which follows:

$$\begin{aligned} c_4 = |OF| &= |BG|\sin\angle BGF \cdot \cot\angle BOF = -\sin\left(\alpha + \frac{\theta}{2}\right)\tan\left(\frac{\alpha+\theta}{2}\right) \\ &= \frac{|OA|\sin\alpha}{\sin\angle BGF} - \cos\angle BGF = \frac{\sin\alpha}{\sin\left(\alpha + \frac{\theta}{2}\right)} + \cos\left(\alpha + \frac{\theta}{2}\right)\ , \end{aligned} \tag{2.66}$$

where the definitions of α, $\angle BGF$, and $\angle BOF$ are shown in Fig. 2.6. Thus, the solution of

[9] In some singular cases, (x^*, y^*) may move along the border line ℓ.

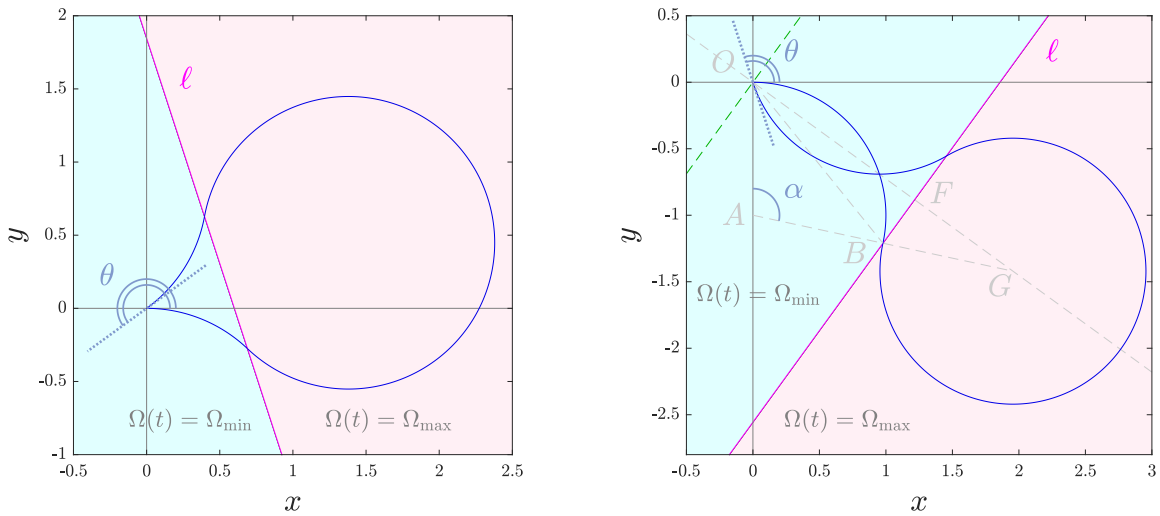

Figure 2.6: Optimized closed Dubins curve examples (blue curves) under the assumptions of $|\Omega(t)| \leq 1$, $\Omega^*(0) = \Omega^*(T) = -1$. The values of θ are taken as 1.2π and 0.6π for the left and right panels separately. The curves start at the origin tangential to the x-axis. In both figures, divided by purple line ℓ (Eq. (2.65)), the pink half-plane requires the trajectories' curvature being $+1$, and the cyan half-plane requires the trajectories' curvature being -1.

c_4 can be obtained by eliminating α:

$$c_4 = \cos\frac{\theta}{2} + \frac{1}{8}\left|\sec\frac{\theta}{2}\right|\sqrt{30 + 32\cos\theta + 2\cos 2\theta}\ , \tag{2.67}$$

for $0 < \theta < 2\pi$. Finally, since the solution of the trajectory has been determined, the last constant c_3 can be found by combining $v_x^*(\alpha)p_4^*(\alpha) - v_y^*(\alpha)p_3^*(\alpha) = 0$ with Eq. (2.61). Hence, the optimal solution of state $\mathbf{x}^*(t)$ and costate $\mathbf{p}^*(t)$ has been found.

2.4.3 Discovering Time-Optimal Pulses by Machine Learning

When facing real engineering problems, we are looking for admissible control functions which fulfill the constraints of noise decoupling, control time optimization, pulse limitation. Although there are mature theories such as PMP [73], solving the highly coupled differential equations in this framework with constraint is challenging and tricky [72], as one can get a

glimpse of section 2.4.2.

What about using numerical approaches? The challenge of finding control pulses mainly comes from searching the functional space. A good parameterization or good initial guess of the target function can drastically simplify the complexity. It would be great if the machine can discover the solution by itself without too much prior knowledge from the human. With the rapid development of algorithms in the machine learning community, artificial neural networks (ANN) have been known to be a promising way of solving such complicated problems. Noticeably, there have been some recent works showing the power of ANN in tackling quantum control problems [76–80]. Inspired by [80], but with a different goal, in this section, we combine the numerical approach of a physics-informed neural network (PINN) [81] and the geometric formalism [1] to discover appropriate control pulses. Technically, instead of feeding PINN with plenty of experimental data, one needs to feed it with the physical law – usually differential equation (e.g. $\dot{\mathbf{x}} = \mathbf{f}(\mathbf{x}, \mathbf{u})$) into the loss function of ANN: Loss $:=$ MSE $[\dot{\mathbf{x}} - \mathbf{f}(\mathbf{x}, \mathbf{u})] + \cdots$, where MSE$(\cdot)$ is the mean squared error during the evolution. Once the loss function is minimized to nearly zero, the outputs of the ANN ($\mathbf{x}$ and $\mathbf{u}$) are a good approximation of the solution that follows the equations of motion.

2.4.3.1 Example

This subsection provides a numerical test, which suggests that this approach could be a promising way of finding DECG in the gigantic admissible control function space. Concretely, we are finding DECG for the following quantum Hamiltonian:

$$\hat{H}(t) = \frac{1}{2}\Omega(t)\sigma_x + \frac{1}{2}\Delta\sigma_z + \lambda\sigma_z \ , \tag{2.68}$$

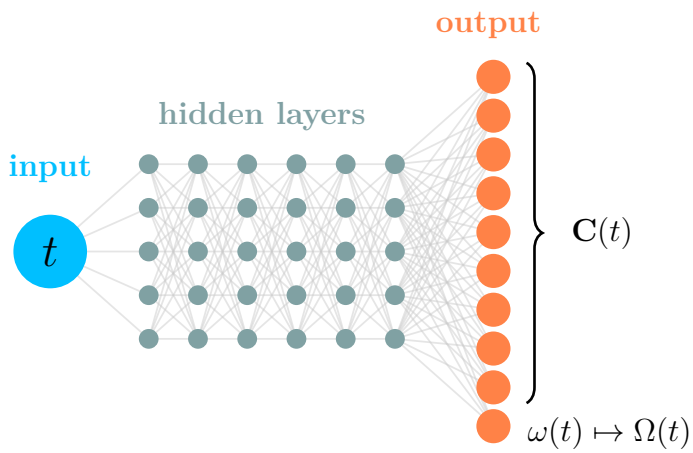

Figure 2.7: The ANN structure that this section uses for a PINN. The outputs are the expected trajectory and control function, while the input here is a single variable. As long as the activation functions in the hidden layers are continuous, the output will be a continuous function with respect to the input. To obtain the result in Fig. 2.8, our models use $\tanh(\cdot)$ as the activation function by default. The ANN has a fully connected layout with 6 hidden layers, each of them with 256 nodes. 10 outputs are needed for a 3×3 matrix $\mathbf{C}(t)$ and a control field $\Omega(t)$.

in which λ is a time-independent small constant ($\lambda \ll 1$). This Hamiltonian is practical, especially for semiconductor double quantum dot systems with constant detuning [35, 76, 82]. In such scenarios, $\Omega(t)$ has the physical meaning of spin-spin exchange energy, which is presumably controllable through tuning a potential well barrier, and Δ is a fixed constant for detuning. In this case, we will treat $\lambda\sigma_z$ as the perturbation, and use $H_0(t) = \frac{1}{2}\left[\Omega(t)\sigma_x + \Delta\sigma_z\right]$ as the control Hamiltonian. Despite the fact that only one control field is available, theoretically, any $SU(2)$ rotation can be achieved with non-zero Δ. Nevertheless, the fixed Δ is undoubtedly unhandy for designing DECG, since [76] had already attempted to deal with the same problem with ANN, we will further show that the application of PINN is more powerful and flexible. Again, after switching to the interaction picture, we have $\hat{H}_I(t) = \lambda U_0^\dagger(t)\sigma_z U_0(t)$,

where $U_0(t)$ can be parameterized by the $SO(3)$ rotation matrix[10]:

$$R_{ij}(t) = \frac{1}{2}\mathrm{tr}\left[\sigma_i U_0^\dagger \sigma_j U_0\right] \Rightarrow R(t) = \begin{bmatrix} -B_x & N_x & T_x \\ -B_y & N_y & T_y \\ -B_z & N_z & T_z \end{bmatrix} . \tag{2.69}$$

Here we use symbols $\mathbf{T}$, $\mathbf{N}$ and $\mathbf{B}$ to represent the tangent vector, normal vector and binormal vector, since under this notation, $R(t)$ fulfills "Frenet–Serret formulas":

$$\begin{bmatrix} \dot{\mathbf{T}} \\ \dot{\mathbf{N}} \\ \dot{\mathbf{B}} \end{bmatrix} = \begin{bmatrix} 0 & \Omega(t) & 0 \\ -\Omega(t) & 0 & -\Delta \\ 0 & \Delta & 0 \end{bmatrix} \begin{bmatrix} \mathbf{T} \\ \mathbf{N} \\ \mathbf{B} \end{bmatrix} , \tag{2.70}$$

which generates an integrated curve of $\mathbf{T}$ with constant torsion Δ and curvature $\Omega(t)$. To avoid using a time-consuming integral on ANN, we will parameterize these curves via the matrix $\mathbf{C}(t)$:

$$\left.\begin{aligned} \mathbf{C}_{1i}(t) &:= \int_0^t \mathbf{T}_i(\tau)\mathrm{d}\tau \\ \mathbf{C}_{2i}(t) &:= \int_0^t \mathbf{N}_i(\tau)\mathrm{d}\tau \\ \mathbf{C}_{3i}(t) &:= \int_0^t \mathbf{B}_i(\tau)\mathrm{d}\tau \end{aligned}\right\} \quad i = 1, 2, 3 \ , \Leftrightarrow \dot{\mathbf{C}} = [\mathbf{T}, \mathbf{N}, \mathbf{B}] \tag{2.71}$$

which is treated as part of the output of the ANN (See Fig. 2.7). The remaining output of the ANN is $\omega(t)$, which is reserved for the control function $\Omega(t)$. We do not treat the output directly as $\Omega(t)$, since the real system always possesses bounded $\Omega(t)$, otherwise, not only the infinite large spin exchange interaction is unreal, an ultra-fast Dirac-delta-like $\Omega(t)$ function will also trivialize the problem. Since the direct output of ANN is generally un-bounded, we can convert $\omega(t)$ to $\Omega(t)$ by

$$\Omega(t) = u_{\min} + (u_{\max} - u_{\min}) \sin^2[\omega(t)] \ , \tag{2.72}$$

[10]The global phase of U_0 is negligible.

such that $\Omega(t)$ is confined in the interval $[u_{\min}, u_{\max}]$.

With all these above ingredients, we can train our ANN with following loss function:

$$\text{Loss} = \text{MSE}_{\text{eom}} + \text{MSE}_{bc} + \text{MSE}_p \ , \tag{2.73}$$

where in order to satisfy the constraints of the equation of motion, the first term is

$$\begin{aligned}\text{MSE}_{\text{eom}} = \frac{1}{M}\sum_{j=1}^{M} &\left\| \begin{bmatrix} \dot{\mathbf{T}}(t_j) \\ \dot{\mathbf{N}}(t_j) \\ \dot{\mathbf{B}}(t_j) \end{bmatrix} - \begin{bmatrix} 0 & \Omega(t_j) & 0 \\ -\Omega(t_j) & 0 & -\Delta \\ 0 & \Delta & 0 \end{bmatrix} \begin{bmatrix} \mathbf{T}(t_j) \\ \mathbf{N}(t_j) \\ \mathbf{B}(t_j) \end{bmatrix} \right\|^2 \\ &+ \left\| |\mathbf{T}(t_j)| - 1 \right\|^2 + \left\| |\mathbf{N}(t_j)| - 1 \right\|^2 + \left\| |\mathbf{B}(t_j)| - 1 \right\|^2 \\ &+ \left\| \mathbf{T}(t_j) \times \mathbf{N}(t_j) - \mathbf{B}(t_j) \right\|^2 \end{aligned} . \tag{2.74}$$

So as to yield an identity gate DECG and a closed curve $\int_0^t \mathbf{T}(\tau)\mathrm{d}\tau$, the second term is for imposing boundary conditions:

$$\text{MSE}_{bc} = \left\| \dot{\mathbf{C}}(0) - \mathbb{I} \right\|^2 + \left\| \dot{\mathbf{C}}(T) - \mathbb{I} \right\|^2 + \sum_{i=1}^{3} \left\| \mathbf{C}_{1i}(0) \right\|^2 + \left\| \mathbf{C}_{1i}(T) \right\|^2 \ . \tag{2.75}$$

Finally, we hope to obtain a symmetric pulse that has both ends being zero, which is sometimes preferred in the experiment, thus, the third term is:

$$\text{MSE}_p = \left\| \Omega(0) \right\| + \left\| \Omega(T) \right\| + \frac{1}{M}\sum_{j=1}^{M} \left\| \Omega(t_j) - \Omega(T - t_j) \right\|^2 \ . \tag{2.76}$$

In Eq. (2.74) and (2.76), $\{t_i : 0 \leq t_i \leq T, 1 \leq i \leq M\}$ is a random set updated throughout the training, with $M \sim 10^2$. Training our ANN is done by minimizing the loss function under a given T, via updating the weights and bias in the network. We find that the ADAM optimizer [83] has a robust performance in finding the minimum. Specifically, the

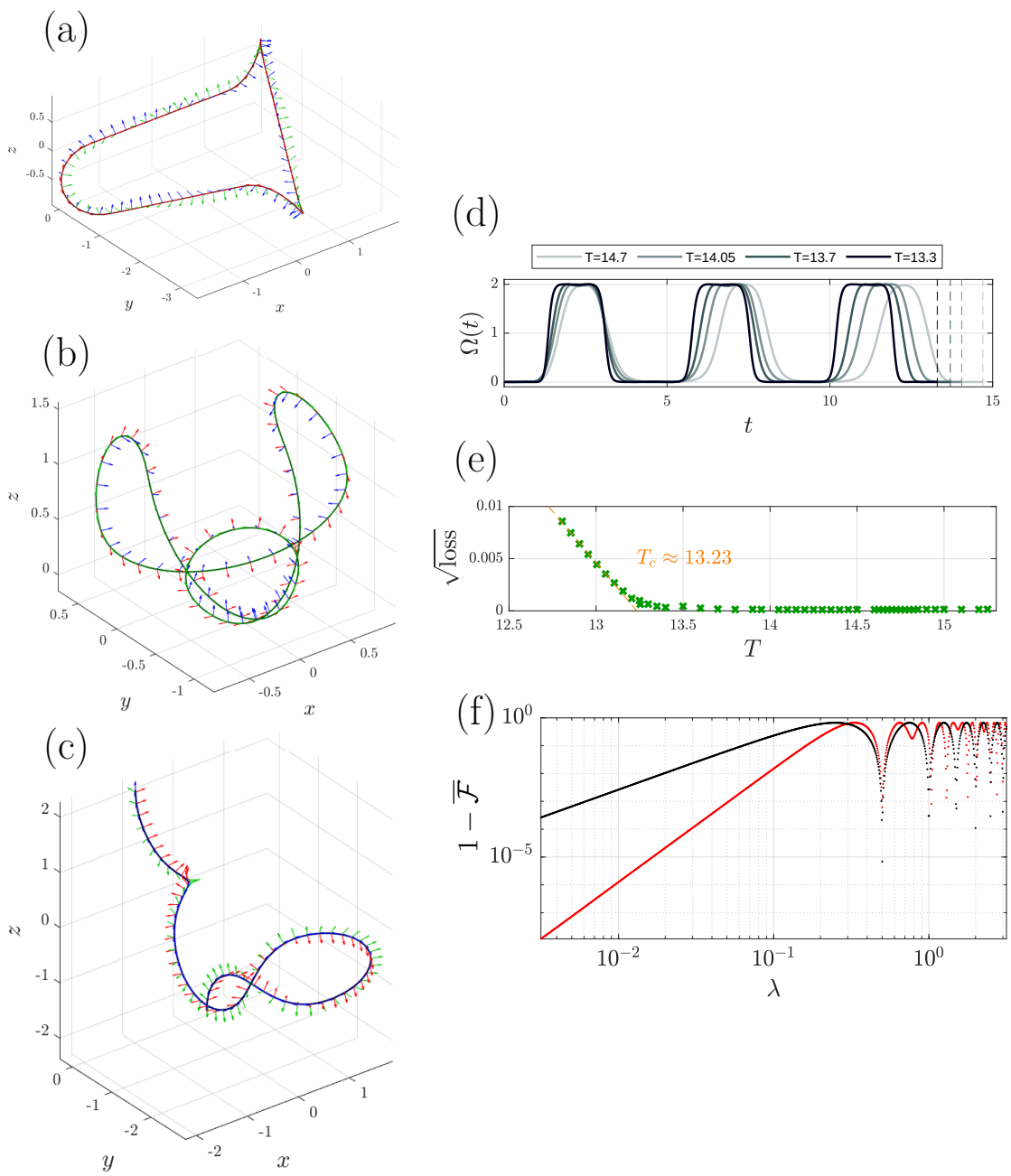

Figure 2.8: A near-optimal curve design outcome instance found by PINN. In the first 3 panels, red, green and green arrows represent $\mathbf{T}$, $\mathbf{N}$ and $\mathbf{B}$ separately. Panel (a,b,c) display the integrated curves of $\mathbf{T}$, $\mathbf{N}$ and $\mathbf{B}$. Under $T = 13.3$ and $\Delta = 1$. Panel (d) displays the control pulse at different T found by PINN, which value is bounded by $[0, 2]$. Panel (e) displays the square root of loss function v.s. different control time T, after $> 10^6$ steps of ANN training. The turning point in panel (e) implies a critical (optimum) control time $T_c \approx 13.23$. (f) presents the infidelity comparison between the result with the $T = 13.3$ pulse given in (d), and the result with $\Omega(t) \equiv 0$, $\Delta \cdot T = 2\pi$.

optimizer learning rate is set to be 10^{-3}, with decay rate 0.9 every $\sim 10^3$ steps, for most of our experiments. Since our loss function only consists of MSE of constraints, the criterion of successful training is clear that the loss function should be minimized to nearly 0 or hitting the machine precision, which is $\sim 10^{-8}$ for double-precision floating-point numbers[11]. Fig. 2.8(a,b,c) illustrate one of the training outcomes with $\Delta = 1$, $[u_{\min}, u_{\max}] = [0, 2]$ and near optimum control time $T = 13.3$, where the loss function is $\sim 10^{-7}$. Fig. 2.8(a) displays a closed curve integrated from $\mathbf{T}$, as it is confined by the loss function. Fig. 2.8(b) accidentally gives a closed curve because of

$$\int_0^T \mathbf{N}(\tau)\mathrm{d}\tau = \frac{1}{\Delta}\int_0^T \dot{\mathbf{B}}(\tau)\mathrm{d}\tau = \frac{\mathbf{B}(T) - \mathbf{B}(0)}{\Delta} = 0\ . \tag{2.77}$$

Fig. 2.8(f) shows the infidelity of this $T = 13.3$ pulse, which has behavior $1 - \mathcal{O}(\lambda^4)$. To give a fair comparison, the infidelity of no-control $\Omega(t) \equiv 0$ and $\Delta \cdot T = 2\pi$ is given in this panel, which has inferior behavior $1 - \mathcal{O}(\lambda^2)$. In Fig. 2.8(d), as one decreases T, the pulse shape gets closer and closer to a sequence of square pulses, which suggests that the perfect optimized $\Omega(t)$ can be parameterized by square pulses. More of our numerical experiments show that, empirically, if the minimal T is *near* T_c, then the loss function behaves like $\mathcal{O}((T_c - T)^2)$ when $T < T_c$. On the other hand, the convergence rate becomes slow as T is in the right neighborhood of T_c. Moreover, after the same long time of training, the *final* loss function at different $T > T_c$ approximately scales as $e^{-c(T-T_c)}$, until the loss gets too small and hits the machine precision.

[11] There are extra MSE terms included in [80], that fails this criterion.

2.5 Quantum Error Correcting Code

Another essential approach of counteracting noise in the quantum system is using quantum error correcting codes (QECC) to protect quantum information. It is one of the cornerstones that the fault-tolerant universal quantum computation built upon. Taking qubit stabilizer code as the example [12, 84, 85], so long as all of the devices at the bottom level are under the error threshold, one can get rid of the noise and perform the arbitrary quantum computation to arbitrary accuracy, by combining fault tolerant Clifford operations and injecting distilled magic states [86]. Although it is theoretically feasible, when this dissertation was written, people had not yet shown that a qubit protected by QECC could significantly outperform an unprotected one, with the current noisy device, not to mention that improving the efficiency of the magic state distillation is still a frontier theoretical problem [87, 88].

The following sections will briefly introduce the QECC and stabilizer formalism. Section 2.5.1 is just an overview of the basics of how QECC works. Section 2.5.2 will be particularly useful for the next chapter.

2.5.1 Introduction of QECC

Let us start with a toy model of quantum bit-flip channel $\mathcal{E}[\hat{\rho}] := (1-p)\hat{\rho} + pX\hat{\rho}X$ and three-qubit repetition code:

$$|0_L\rangle := |000\rangle\,, \quad |1\rangle_L := |1\rangle\,. \tag{2.78}$$

Eq. (2.78) shows the encoding method: the logical state $|0\rangle_L$ ($|1\rangle_L$) is encoded by 3 physical qubits state $|000\rangle$ ($|111\rangle$). That is, any single qubit state $|\psi\rangle := \alpha|0\rangle + \beta|1\rangle$ is encoded as:

$$|\psi_L\rangle := \alpha|0_L\rangle + \beta|1_L\rangle = \alpha|000\rangle + \beta|111\rangle \ . \tag{2.79}$$

Denote the bit-flipped single qubit state as $|\psi'\rangle := \alpha|1\rangle + \beta|0\rangle$, then the bit-flip channel maps $\hat{\rho} := |\psi\rangle\langle\psi|$ to

$$\mathcal{E}[|\psi\rangle\langle\psi|] := (1-p)|\psi\rangle\langle\psi| + p|\psi'\rangle\langle\psi'| \ , \tag{2.80}$$

which causes decoherence. In the worst case with $\alpha = 1, \beta = 0$, the minimal fidelity of the channel is given by $\langle\psi|\mathcal{E}[\hat{\rho}]|\psi\rangle = 1-p$. However, it can be shown that, using the logical state in Eq. (2.78), we can suppress the error [89] if p is below some threshold. Specifically, the worst fidelity can be improved as $1-3p^2+2p^3$. To demonstrate how it works, we assume the state $|\psi_L\rangle\langle\psi_L|$ has been transmitted through channel $\mathcal{E}^{\otimes 3}[\cdot] := \mathcal{E}\otimes\mathcal{E}\otimes\mathcal{E}[\cdot]$, which means each physical qubit is experiencing independent bit-flip channel. First, we project the noisy state to the eigen-subspace of Pauli-operators[12] Z_1Z_2 and Z_2Z_3. Such projection can be physically realized as multi-qubit measurements, whose readouts are called *error syndromes* and can only be ± 1 in this case. If we denote the syndrome of Z_1Z_2 as $(-1)^{s_1}$ and the syndrome of Z_2Z_3 as $(-1)^{s_3}$ ($s_1, s_3 \in \{0,1\}$). then we know the error occurs when the read out of s_1 or s_3 becomes 1. Lastly, the state should be corrected by bit-flip unitary $X_1^{s_1}X_3^{s_3}$. This procedure is imitating the classical repetition code, where one uses multiple 0's and 1's to represent logical 0 and 1. Error detection and correction can be understood as "majority voting" (e.g. $001 \to 000$, $110 \to 111$). On the quantum repetition code side, the projections of Z_1Z_2 and Z_2Z_3 forcing the system to stay in a two-dimensional logical subspace (i.e., code space), spanned by $\{|0_L\rangle, |1_L\rangle\}$. Any single qubit bit-flip simply change this subspace to

[12] In this dissertation adopts the notation that Z_1 stands for $Z\otimes\mathbb{1}\otimes\mathbb{1}\otimes\cdots$, and likewise X_2 stands for $\mathbb{1}\otimes X\otimes\mathbb{1}\otimes\cdots$, *et al.*

an orthogonal one, without messing up the information inside. Hence, one can suppress the error when the bit-flip rate $p \ll 1$, in which the total perturbation is dominated by single bit-flip error.

The contribution of Shor [89] is showing that by concatenating the repetition code (2.78):

$$|0_L\rangle := 2^{-3/2}\left(|000\rangle + |111\rangle\right)^{\otimes 3}, \quad |1\rangle_L := 2^{-3/2}\left(|000\rangle - |111\rangle\right)^{\otimes 3} , \tag{2.81}$$

one can both counter both single bit-flip and phase-flip error by detecting syndrome and correction. Although using 9 physical qubit to encode 1 logical qubit is inefficient, it was the first QECC that can correct any single qubit error. This procedure of detecting syndrome and correcting error soon become a paradigm. The criterion of designing QECC is given by Knill–Laflamme condition [90]: Let the projection operator to the code space be $\mathcal{P}_C$, then a set of error $\{\hat{E}_i\}$ is correctable if and only if

$$\mathcal{P}_C \hat{E}_i^\dagger \hat{E}_j \mathcal{P}_C = c_{ij} \mathcal{P}_C \tag{2.82}$$

for some Hermitian matrix c_{ij}. Under this framework, various QECC with different interesting features are proposed in the past decades. Such as five-qubit code[91] is the smallest code that counter any single qubit error, Calderbank-Shor-Steane (CSS) code [92] is a category of "good QECC" that can be construct from classical binary linear code, Surface code [93, 94] utilize topology of the lattice to protect logical quantum data from any local error, *et al.* One can find an abundant collection of QECC in error correction zoo (`https://errorcorrectionzoo.org/`). To realize these tempting and promising schemes, people have also invested a great amount of effort in the experiments of QECC [95–97]. Any experimental breakthrough will be extremely meaningful for the quantum information science.

2.5.2 Stabilizer Formalism

Notice that in the previous example of three-qubit repetition code (2.78), the code space projector can be written as $\mathcal{P}_C = \frac{1+Z_1Z_2}{2}\frac{1+Z_2Z_3}{2}$. In other words, any pure logical state encoded this way is a eigenstate of the following operators

$$g_1 = Z_1Z_2, \quad g_2 = Z_2Z_3 \tag{2.83}$$

with eigenvalue +1. These operators known as *stabilizer* operators generate a group $\mathscr{G} = \langle\{g_1, g_2\}\rangle$ known as the *stabilizer group*. We emphasize that stabilizers are commutative, thus, $\mathscr{G}$ is simply an Abelian group. In this section, we only discussion qubit stabilizer formalism[13], thus, when we assign m $(0 \leq m \leq n)$ independent stabilizer generators for n qubits, $|\mathscr{G}| = 2^m$, and a subspace of dimension 2^{n-m} is determined. If $m = n$, then these stabilizer generators determine a pure stabilizer state, which is the common eigenstate of all elements in $\mathscr{G}$.

Returning back to the Knill-Laflamme condition in section 2.5.1, once $\mathcal{P}_C$ is determined by a stabilizer group $\mathscr{G}$, the *un-correctable* errors are those Pauli operator in $N(\mathscr{G}) \setminus \mathscr{G}$, in which $N(\mathscr{G})$ is the normalizer of $\mathscr{G}$ in Pauli group. This framework or formalism with stabilizer operators provides a way of neat representation for some special quantum states. For examples, the code space of nine-qubit Shor code [89] is given by following stablizers:

$$\begin{aligned} &S_1 = Z_1Z_2, \quad S_2 = Z_2Z_3, \quad S_3 = X_1X_2X_3X_4X_5X_6, \\ &S_4 = Z_4Z_5, \quad S_5 = Z_5Z_6, \quad S_6 = X_4X_5X_6X_7X_8X_9, \\ &S_7 = Z_7Z_8, \quad S_8 = Z_8Z_9, \end{aligned} \tag{2.84}$$

[13] See [98] for multi-level stabilizer formalism.

and the five-qubit code [91] has the following stabilizers:

$$S_1 = Z_1X_2X_3Z_4, \quad S_2 = Z_2X_3X_4Z_5, \quad S_3 = Z_3X_4X_5Z_1, \quad S_4 = Z_4X_5X_1Z_2 \quad . \tag{2.85}$$

Such stabilizer formalism has simplified the theoretical analysis in a great extent [84], which brought the booming of QECC [99] in the early 2000s. The nice tractability of stabilizer formalism is sometimes known as Gottesman-Knill theorem [100, 101]: A quantum circuit that

1. preparing the initial state in computational basis,
2. performing unitary operation through Clifford gates (generated by H, P, and CNOT gates),
3. and performing measurements in computational basis,

can be simulated with classical computer efficiently. Here, efficient simulation means the only polynomially many steps and classical bits are needed to finish the computation.

We will first explain how the first two elements can be efficiently simulated by classical computer. The Clifford gate generators mentioned above are defined as follows:

$$H := \frac{X+Z}{\sqrt{2}}, \quad P := \mathrm{diag}(1, i), \quad \mathrm{CNOT}_{ij} := |0\rangle\langle 0|_i + |1\rangle\langle 1|_i \, X_j \; . \tag{2.86}$$

On the n-qubit system, the closed set of all possible unitary operations generated by Eq. (2.86) is called *Clifford group* $\mathscr{C}_n$. One of the significant features of $\mathscr{C}_n$ is that it is the *normalizer* of n-qubit Pauli group in $U(2^n)$. In other words, $U \in \mathscr{C}_n$ always converts a Pauli operator $i^s\sigma_{\alpha_1} \otimes \sigma_{\alpha_2} \otimes \cdots$ to another $i^{s'}\sigma_{\beta_1} \otimes \sigma_{\beta_2} \otimes \cdots$ by conjugation $U^\dagger(\cdots)U$, where $s, s' \in \mathbb{Z}$, $\alpha_i, \beta_i \in \{0, 1, 2, 3\}$. Particularly, the transformation rules for unitaries in Eq. (2.86) can be

found in [102] or table 2.1. Utilizing this feature, any $U \in \mathscr{C}_n$ can be *uniquely* represented

$U = H$	
$\hat{\sigma}$	$U\hat{\sigma}U^\dagger$
X	Z
Y	$-Y$
Z	X

,

$U = P$	
$\hat{\sigma}$	$U\hat{\sigma}U^\dagger$
X	Y
Y	$-X$
Z	Z

,

$U = \mathrm{CNOT}_{12}$			
$\hat{\sigma}_1\hat{\sigma}_2$	$U\hat{\sigma}_1\hat{\sigma}_2U^\dagger$	$\hat{\sigma}_1\hat{\sigma}_2$	$U\hat{\sigma}_1\hat{\sigma}_2U^\dagger$
II	II	YI	YX
IX	IX	YX	YI
IY	ZY	YY	$-XZ$
IZ	ZZ	YZ	XY
XI	XX	ZI	ZI
XX	XI	ZX	ZX
XY	YX	ZY	IY
XZ	$-YY$	ZZ	IZ

.

Table 2.1: The transformation rules for Hadamard H, phase gate P and controlled-NOT operation CNOT.

by n stabilizers S_i and n destabilizers D_i [101]:

$$D_i := U^\dagger X_i U, \qquad S_i := U^\dagger Z_i U, \quad i = 1, 2, \cdots, n\ . \tag{2.87}$$

Let's prove that such representation is unique: If representation with $\{D_i, S_i\}$ is not unique, such that there is a pair of $U, U' \in \mathscr{C}_n$ ($U \neq U'$) producing the same set of $\{D_i, S_i\}$ by Eq. (2.87), then the Clifford unitary $U'' := U^\dagger U' \in \mathscr{C}_n$ *centralizes* the Pauli group. Yet, the centralizer of Pauli group in $U(2^n)$ is nothing but a trivial operation $\propto \mathbb{1}$, which proves the uniqueness that $U = U'$ up to an ignorable global phase. $\square$

A further question is: How do we represent the set of $\{D_i, S_i\}$? D_i and S_i are just some signed Pauli string of X, Y and Z, that can be represented by a $2n \times 2n$ binary matrix and

a $2n$-component binary sign vector:

$$\mathbf{T}(U) := \left[\begin{array}{ccc|ccc} x_{1,1} & \cdots & x_{1,n} & z_{1,1} & \cdots & z_{1,n} \\ \vdots & \ddots & \vdots & \vdots & \ddots & \vdots \\ x_{n,1} & \cdots & x_{n,n} & z_{n,1} & \cdots & z_{n,n} \\ \hline x_{n+1,1} & \cdots & x_{n+1,n} & z_{n+1,1} & \cdots & z_{n+1,n} \\ \vdots & \ddots & \vdots & \vdots & \ddots & \vdots \\ x_{2n,1} & \cdots & x_{2n,n} & z_{2n,1} & \cdots & z_{2n,n} \end{array}\right], \quad \mathbf{r}(U) := \left[\begin{array}{c} r_1 \\ \vdots \\ r_n \\ \hline r_{n+1} \\ \vdots \\ r_{2n} \end{array}\right], \tag{2.88}$$

such that the destabilizer D_i and the stabilizer S_i are written as:

$$\begin{aligned} D_i &= (-1)^{r_i} \cdot \sigma^{(x_{i,1},z_{i,1})} \otimes \sigma^{(x_{i,1},z_{i,1})} \otimes \cdots \otimes \sigma^{(x_{i,n},z_{i,n})} \\ S_i &= (-1)^{r_{i+n}} \cdot \sigma^{(x_{i+n,1},z_{i+n,1})} \otimes \sigma^{(x_{i+n,1},z_{i+n,1})} \otimes \cdots \otimes \sigma^{(x_{i+n,n},z_{i+n,n})} \end{aligned}, \tag{2.89}$$

with

$$\sigma^{(0,0)} := I, \quad \sigma^{(1,0)} := X, \quad \sigma^{(1,1)} := Y, \quad \sigma^{(0,1)} := Z. \tag{2.90}$$

One of the advantages of Eq. (2.88) is that it only takes Poly(n) steps to simulate the multiplication of Clifford unitaries $U_1, U_2 \in \mathscr{C}_n \subset U(2^n)$. The approach in [101] can be summarized as:

$$\mathbf{T}(U_1U_2) = \mathbf{T}(U_2)\mathbf{T}(U_1) \mod 2, \quad \forall U_1, U_2 \in \mathscr{C}_n \ , \tag{2.91}$$

and $\mathbf{r}(U_1U_2)$ is given in a non-linear fashion:

$$\begin{aligned} \mathbf{r}_i(H_aU) = \mathbf{r}_i(P_aU) &= \mathbf{r}_i(U) + \mathbf{T}_{i,a}(U)\mathbf{T}_{i,a+n}(U) \mod 2 \ , \\ \mathbf{r}_i(\mathrm{CNOT}_{ab}U) &= \mathbf{r}_i(U) + \mathbf{T}_{i,a}(U)\mathbf{T}_{i,b+n}(U)(\mathbf{T}_{i,a}(U) + \mathbf{T}_{i,b+n}(U) + 1) \mod 2 \ . \end{aligned} \tag{2.92}$$

Similarly, the code space defined by projector $\mathcal{P}_C$ represented by m independent stabilizers ($m \leq n$) can be written as a $m \times 2n$ binary matrix $\mathbf{T}[\mathcal{P}_C]$ and a m component sign vector

$\mathbf{r}[\mathcal{P}_C]$. The representation of $U\mathcal{P}_C U^\dagger$ is given by

$$\mathbf{T}[U\mathcal{P}_C U^\dagger] = \mathbf{T}[\mathcal{P}_C]\mathbf{T}(U) \mod 2, \quad \forall U \in \mathscr{C}_n \ , \tag{2.93}$$

and likewise the Eq. (2.92) will be called to find $\mathbf{r}[U\mathcal{P}_C U^\dagger]$:

$$\begin{aligned} \mathbf{r}_i[H_a\mathcal{P}_C H_a^\dagger] = \mathbf{r}_i[P_a\mathcal{P}_C P_a^\dagger] &= \mathbf{r}_i[\mathcal{P}_C] + \mathbf{T}_{i,a}[\mathcal{P}_C]\mathbf{T}_{i,a+n}[\mathcal{P}_C] \mod 2 \ , \\ \mathbf{r}_i[\mathrm{CNOT}_{ab}\mathcal{P}_C\mathrm{CNOT}_{ab}^\dagger] &= \mathbf{r}_i[\mathcal{P}_C] + \mathbf{T}_{i,a}[\mathcal{P}_C]\mathbf{T}_{i,b+n}[\mathcal{P}_C]\left(\mathbf{T}_{i,a}[\mathcal{P}_C] + \mathbf{T}_{i,b+n}[\mathcal{P}_C] + 1\right) \mod 2 \ . \end{aligned} \tag{2.94}$$

We demonstrate the ideas above by the example of a three-qubit Greenberger–Horne–Zeilinger (GHZ) state, whose state vector

$$|\mathrm{GHZ}_3\rangle := \frac{|000\rangle + |111\rangle}{\sqrt{2}} = U_{\mathrm{GHZ}}\,|000\rangle = \mathrm{CNOT}_{23}\mathrm{CNOT}_{12}H_1\,|000\rangle \tag{2.95}$$

can be represented by stabilizers

$$S_1 = X_1X_2X_3, \quad S_2 = Z_1Z_2, \quad S_3 = Z_2Z_3 \ , \tag{2.96}$$

One can also represent $|\mathrm{GHZ}_3\rangle$ with density matrix or projector $\hat{\rho}_{\mathrm{GHZ}} = |\mathrm{GHZ}_3\rangle\langle\mathrm{GHZ}_3| = U_{\mathrm{GHZ}}\hat{\rho}_0 U_{\mathrm{GHZ}}^\dagger = \mathcal{P}_C = \prod_{i=1}^3 \frac{1+S_i}{2}$, where $\hat{\rho}_0 := |000\rangle\langle 000|$ is a state prepared in computational basis. Starting with

$$\mathbf{T}[\hat{\rho}_0] = \left[\begin{array}{ccc|ccc} 0 & 0 & 0 & 1 & 0 & 0 \\ 0 & 0 & 0 & 0 & 1 & 0 \\ 0 & 0 & 0 & 0 & 0 & 1 \end{array}\right] \ , \quad \mathbf{r}[\hat{\rho}_0] = \mathbf{0} \ , \tag{2.97}$$

and

$$\mathbf{T}(H_1) = \left[\begin{array}{ccc|ccc} 0 & 0 & 0 & 1 & 0 & 0 \\ 0 & 1 & 0 & 0 & 0 & 0 \\ 0 & 0 & 1 & 0 & 0 & 0 \\ \hline 1 & 0 & 0 & 0 & 0 & 0 \\ 0 & 0 & 0 & 0 & 1 & 0 \\ 0 & 0 & 0 & 0 & 0 & 1 \end{array}\right], \quad \mathbf{T}(\mathrm{CNOT}_{12}) = \left[\begin{array}{ccc|ccc} 1 & 1 & 0 & 0 & 0 & 0 \\ 0 & 1 & 0 & 0 & 0 & 0 \\ 0 & 0 & 1 & 0 & 0 & 0 \\ \hline 0 & 0 & 0 & 1 & 0 & 0 \\ 0 & 0 & 0 & 1 & 1 & 0 \\ 0 & 0 & 0 & 0 & 0 & 1 \end{array}\right],$$

$$\mathbf{T}(\mathrm{CNOT}_{23}) = \left[\begin{array}{ccc|ccc} 1 & 0 & 0 & 0 & 0 & 0 \\ 0 & 1 & 1 & 0 & 0 & 0 \\ 0 & 0 & 1 & 0 & 0 & 0 \\ \hline 0 & 0 & 0 & 1 & 0 & 0 \\ 0 & 0 & 0 & 0 & 1 & 0 \\ 0 & 0 & 0 & 0 & 1 & 1 \end{array}\right],$$

there is $\mathbf{T}(U_{\mathrm{GHZ}}) = \mathbf{T}(\mathrm{CNOT}_{23}\mathrm{CNOT}_{12}H_1) = \mathbf{T}(H_1)\mathbf{T}(\mathrm{CNOT}_{12})\mathbf{T}(\mathrm{CNOT}_{23})$:

$$\mathbf{T}(U_{\mathrm{GHZ}}) = \left[\begin{array}{ccc|ccc} 0 & 0 & 0 & 1 & 0 & 0 \\ 0 & 1 & 1 & 0 & 0 & 0 \\ 0 & 0 & 1 & 0 & 0 & 0 \\ \hline 1 & 1 & 1 & 0 & 0 & 0 \\ 0 & 0 & 0 & 1 & 1 & 0 \\ 0 & 0 & 0 & 0 & 1 & 1 \end{array}\right]. \tag{2.98}$$

Meanwhile, the Eq. (2.92) acts trivially in this case: $\mathbf{r}(U_{\mathrm{GHZ}}) = 0$. Hence, one finds that

$$\mathbf{T}[\hat{\rho}_{\mathrm{GHZ}}] = \mathbf{T}[\hat{\rho}_0]\mathbf{T}(U_{\mathrm{GHZ}}) = \left[\begin{array}{ccc|ccc} 1 & 1 & 1 & 0 & 0 & 0 \\ 0 & 0 & 0 & 1 & 1 & 0 \\ 0 & 0 & 0 & 0 & 1 & 1 \end{array}\right], \quad \mathbf{r}[\hat{\rho}_{\mathrm{GHZ}}] = \mathbf{0}\,, \tag{2.99}$$

which correspond to the stabilizers S_i of $|\mathrm{GHZ}_3\rangle$ as shown in Eq. (2.96).

In the remain part of this section will explain how describe computation basis measurement under stabilizer formalism. Consider a n-qubit stabilizer state $\hat{\rho}$ (not necessarily pure), and its m independent stabilizers. Denote its stabilizer group by $\mathscr{G} := \langle\{S_i\}\rangle$. As one measures $\hat{\rho}$ on qubit i along z-axis, $\hat{\rho}$ is either projected to a eigen-subspace of Z_i, with eigenvalue

either $+1$ or -1. The stabilizer generator set $\{S_i\}$ is updated in different ways depending on the following cases:

1. Either Z_i or $-Z_i$ is a member of $\langle\{S_i\}\rangle$, then keep the generator set $\{S_i\}$ unchanged.

2. Both Z_i and $-Z_i$ are not the member of $\langle\{S_i\}\rangle$, and Z_i commute with all members in $\{S_i\}$, then add Z_i or $-Z_i$ to the generator set $\{S_i\}$ with equal probability.

3. Both Z_i and $-Z_i$ are not the member of $\langle\{S_i\}\rangle$, but there is $S'_k \in \{S_i\}$ that $\{S'_k, Z_i\} = 0$, then replace the first S'_1 with $\pm Z_i$ with equal probability. For the other S'_k (if there is any), perform replacement: $S'_2 \to S'_1 S'_2$, $S'_3 \to S'_1 S'_3$, *et al.*

In the first two cases, determining whether $\pm Z_i$ is a member of $\langle\{S_i\}\rangle$ can be done by finding whether the row space of $\mathbf{T}[\rho]$ contains the vector $[0\cdots010\cdots0]$, whose only element 1 appears at the i-th component. This procedure is the same as Gaussian elimination, which can be done efficiently in polynomial steps.

As a summary, this subsection has demonstrated how to use the stabilizer formalism to efficiently simulate a large Clifford circuit. It does not only improve our understanding of the complexity hierarchy of quantum computation [103], but also facilitates and enlightens different research areas like code design [104, 105], protocol design [5], and even quantum chaos and random quantum circuits [106–108].

Chapter 3

Entangling Photonic Qubits

Most classical information processing heavily relies on the signal carried by the electromagnetic wave. Thus, it is not surprising for one to associate the quantized electromagnetic wave, or photon, with the carrier of quantum information. In fact, the first quantum cryptography protocol, BB84 [9], which utilizes the fundamental rules of quantum mechanics to share secret information reliably, can be realized with the transmission of photons among different distant parties [10]. Although there is a unified mathematical framework for describing quantum information processing, the photon has its own unique physical feature compared to the immobile matter-based qubits, such as transmons. Usually, a photonic qubit can be encoded by different optical modes (e.g. polarizations) that propagate at the speed of light in optical fibers, wave guides or free space. The mobility makes photons the perfect candidate for delivering quantum information across distant locations, which enables the applications such as quantum networks [9, 109], quantum sensing [110, 111] and distributed quantum computation. Moreover, even though photons cease to exist after measurement, photonic qubits can be produced at a low cost. This implies that the scalability of the photonic quantum system may outperform its matter qubit counterpart. The recent development of integrated photonic circuits is bringing a prospective revolution to quantum optics [25, 26]. Operating quantum optics on microscopic chips has become a future trend.

However, the amplitude of the photonic mode attenuates exponentially due to absorption or scattering. One has to apply loss-tolerant mechanisms to prolong the photon transmis-

sion distance or recapture the information [112–114]. Another well-known challenge is that photons also do not interact with each other under linear optics. Entangled photons produced by constrained experimental approaches can be treated as an important quantum resource [115], because quantum non-locality and correlation is an indispensable primitive in quantum information processing. Therefore, developing efficient entanglement approaches and exploring what we can practically do in quantum optics is imperative.

This chapter focuses on the graph state representation of multipartite entangled photons. Some interesting properties and application examples regarding graph states will be introduced. In the end, we present a theoretical work about an efficient protocol for generating such resources state using minimal light source overhead.

3.1 Multipartite Entangled Photonic State: Graph State

Quantum entanglement allows for quantum non-locality, also known as "spooky action at a distance" for a quantum system. A qubit EPR pair[1], or Bell state $|00\rangle + |11\rangle$, is such a bipartite maximally entangled state that enables quantum teleportation and many other applications [11]. The situation becomes more complicated [116, 117], as one considers the entanglement relation among multiple parties. To understand how quantum correlation can spread across different parties, this section will focus on a special pure state known as qubit graph state, which uses an un-directed graph to represent such an entanglement structure [30][2]. Specifically, given a simple connected graph $G(V, E)$ (see example Fig. 3.1) with set of vertices V ($|V| = n$) and set of edges E, we can use the adjacency matrix $\Gamma_{ij} \in \{0, 1\}^{n\times n}$ to represent $G(V, E)$, where $\Gamma_{ij} = 1$ if $(i, j) \in E$, and $\Gamma_{ij} = 0$ otherwise.

[1]The name of EPR is taken from the last name initials of A. Einstein, B. Podolsky, and N. Rosen.

[2]Quantum graph state defined on qudit case[118], weighted graph [119], and hypergraph [120] are also possible, but they are beyond the scope of this dissertation.

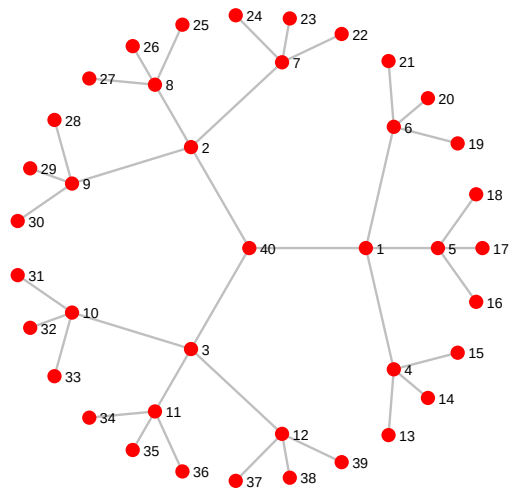

Figure 3.1: A simple connected graph example $G(V, E)$, with $V = \{1, 2, \cdots, 40\}$, and $E = \{(1, 5), (6, 20), (11, 35), \cdots\}$.

With Γ_{ij}, one can defined a commutative set of stabilizers:

$$S_i := X_i \prod_{j \in V} Z_j^{\Gamma_{ij}}, \quad i \in V \ , \tag{3.1}$$

which uniquely determine a pure quantum state $|G\rangle$ known as graph state. One can also define graph state $|G\rangle$ through Clifford operations (see section 2.5.2) by

$$|G\rangle := \prod_{(i,j) \in E} \mathrm{CZ}_{ij} \, |+\rangle^n \ , \tag{3.2}$$

where the controlled-Z gate is defined by $\mathrm{CZ}_{ij} := H_j \mathrm{CNOT}_{ij} H_j$, and $|+\rangle := H \, |0\rangle$. Since the state information is encapsulated in the graph, it is convenient to explore different possibilities by considering different graph configurations.

One of the remarkable results was given by [24], which proposed that universal quantum computation can be done on a cluster state (lattice-like graph state) shown in Fig. 3.2. The required operations are merely local qubit measurements on the x-y plane on the Bloch sphere on this lattice structure, which is sufficient to teleport and manipulate the quantum state

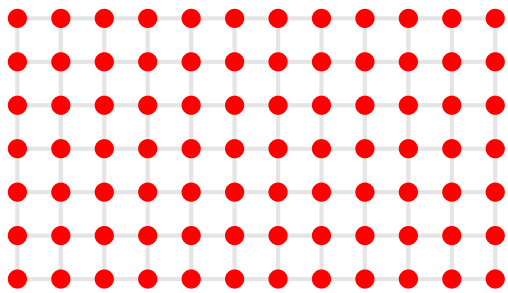

Figure 3.2: Universal computation can be done on the square lattice cluster state shown in this figure, which is known as MBQC.

across the lattice. Such a scheme is known as measurement-based quantum computation (MBQC). Since only short-range correlations are present on cluster state, one can perform such local measurements when the state is half produced. It is generally accepted that photonic states are ideal platform for MBQC, not only because photons are inexpensive but also because reading out photonic qubits is relatively easy, and feed-forward can be done relatively fast.

There are lots of connections between graph states and graph theory. We will present a few examples within the limit of this dissertation. It is known that any pure stabilizer state is local Clifford (LC) equivalent to some graph states. The LC equivalence means one state can be converted to the other by a set of LC unitaries and the conversion recipe is presented in [121]. For example, a three-qubit GHZ state is LC equivalent to a triangular graph state of three vertices. It is also worth noting that this correspondence is not unique, because different graph states can be LC equivalent to each other [30] (a pair of LC equivalent graph states are shown in Fig. 3.3). To see the rule of LC equivalence, denote a set of LC unitaries as

$$U_{LC}^{(a)} := \sqrt{-iX_a} \prod_{b \in N_G(a)} \sqrt{iZ_b}\,, \tag{3.3}$$

where $\sqrt{iZ_b} \equiv P_b^\dagger$ and $\sqrt{-iX_a} \equiv Z_a P_a H_a P_a^\dagger$, whose transformation rule is given in table 3.1. $N_G(a)$ is the set of vertices that are neighbors of vertex a. It can be shown that the graph G

$U = \sqrt{-iX}$	
$\hat{\sigma}$	$U\hat{\sigma}U^\dagger$
X	X
Y	Z
Z	$-Y$

,

$U = \sqrt{iZ}$	
$\hat{\sigma}$	$U\hat{\sigma}U^\dagger$
X	$-Y$
Y	X
Z	Z

Table 3.1: The transformation rules for unitary operation $U = \sqrt{-iX} \equiv ZPHP^\dagger$ and $U = \sqrt{iZ} \equiv P^\dagger$, which are useful for local graph complementation (Eq. (3.3)).

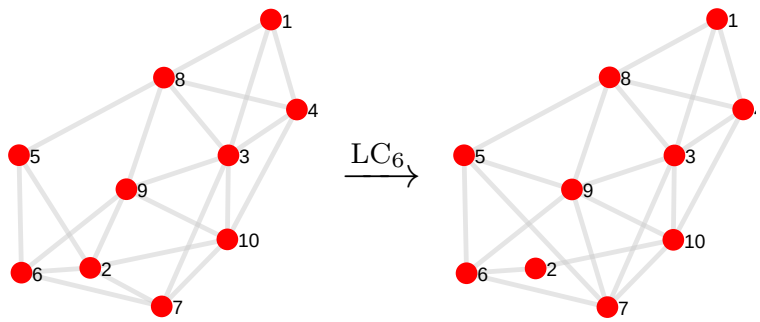

Figure 3.3: An example of applying local graph complementation LC_a, with $a = 6$. The graph state given by the left graph is LC equivalent to the right one by LC unitary $U_{LC}^{(6)}$.

for graph state $|G\rangle$ and the graph G' for graph state $|G'\rangle := U_{LC}^{(a)}|G\rangle$ are differed by graph *local complementation* on vertex a [30]. The operation of local complementation LC_a is given by adding the edges e in $N_G(a)$, if $e \notin E$, and removing e if $e \in E$. Fig 3.3 provides an example of such an operation. For any given two large graphs G and G', one can efficiently determine whether they are equivalent under multiple local complementations [122, 123]. However, classifying all LC equivalent graphs for large $|V|$ is challenging. LC operation or graph local complementation is also valuable when studying the post-measurement state from $|G\rangle$, after measuring a qubit on x, y, or z basis. Firstly, it is easy to conclude that measuring qubit a of $|G\rangle$ in the z-basis will give a post-measurement state $|s\rangle_a |G'\rangle$, with $G' = G \setminus \{a\}$, which means G' is given by removing vertex a and all of the edges attached to it from graph G. Here $|s\rangle_a$ is the measured qubit with $s = 0$ or 1 with equal probability.

To study the case with measurement x or y-basis, we can utilize transformation rules:

$$U_{LC}^{(a)} U_{LC}^{(b)} X_a U_{LC}^{(b)\dagger} U_{LC}^{(a)\dagger} = -Z_a \ , \quad U_{LC}^{(a)} Y_a U_{LC}^{(a)\dagger} = Z_a \ , \tag{3.4}$$

in which b is chosen as any member of $N_G(a)$. Therefore, the post-measurement state of measuring X_a on $|G\rangle$ is given by $U_{LC}^{(b)\dagger} U_{LC}^{(a)\dagger} |s\rangle_a |G'\rangle$ with $G' = (\mathrm{LC}_a \circ \mathrm{LC}_b(G)) \setminus \{a\}$, and the post-measurement state of measuring Y_a on $|G\rangle$ is given by by $U_{LC}^{(a)\dagger} |s\rangle_a |G'\rangle$ with $G' = \mathrm{LC}_a(G) \setminus \{a\}$. This technique of alternating edges by graph local complementation is useful in designing graph state protocols [124, 125].

3.2 Photonic Stabilizer State Generation Protocols

In order to obtain entangled photonic qubits for practical usage, one has to establish entanglement among photons efficiently. In this section we will concentrate on the scheme where matter qubits are used as mediators [4, 27, 28](Fig. 3.4). Particularly, we are interested in the sequential photon emission scenario, where once photons are prepared, no re-interference with matter qubits is allowed. The latter schemes can be found in [29, 126, 127]. As shown in Fig. 3.4, the photon-matter interaction is given by photon emission of a pumped quantum emitter. Formally, the emission can be described as:

$$\alpha |0\rangle_e + \beta |1\rangle_e \longrightarrow \alpha |0\rangle_p |0\rangle_e + \beta |1\rangle_p |1\rangle_e \ , \tag{3.5}$$

where the subscript e and p stand for "emitter" and "photon" separately. One can equivalently treat the un-emitted state as $|0\rangle_p (\alpha |0\rangle_e + \beta |1\rangle_e)$ with an un-emitted fiducial photon, and the emission is given by a CNOT_{ep} operation. With this mechanism, a maximally entangled Bell state can be produced with $\alpha = \beta = 1/\sqrt{2}$. When multiple interacting matter

qubits are involved, one may generate more complicated photonic states, since the quantum correlation within matter qubits may be teleported to the photonic side. We demonstrate

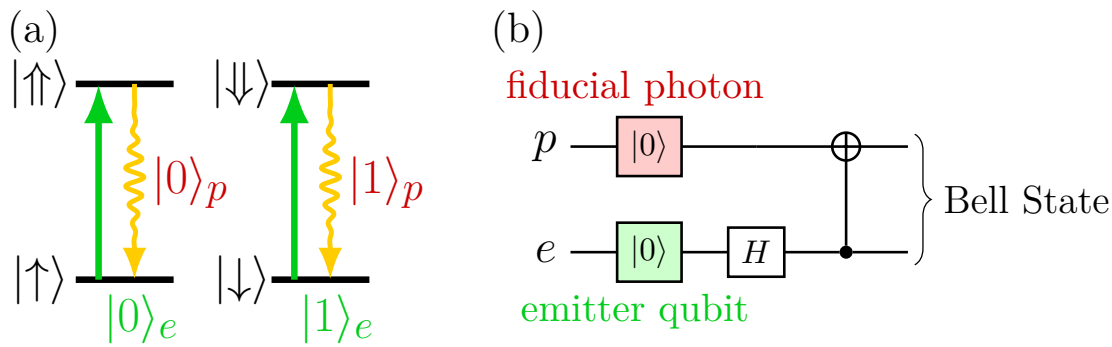

Figure 3.4: The quantum emission scheme presented in [4]. Panel (a) shows a possible level structure of a quantum emitter. The green arrows stand for pumping group state subspace, and release a photon by spontaneous emission. Panel (b) shows the circuit representation of this emission process.

that how the quantum correlation for any quantum graph states, or local equivalently, pure stabilizer states, can be built up with minimal number of quantum emitters, with this no-feedback scheme. It will be meaningful since experiments with fewer resource are usually preferred, and photon feedback in real devices can be challenging.

The following sections are based on the paper [5]: **Bikun Li**, Sophia E. Economou and Edwin Barnes, "Photonic resource state generation from a minimal number of quantum emitters" *npj Quantum Information* 8, 11 (2022)

3.2.1 Introduction

Entanglement is widely recognized as playing a critical role in quantum computation, error correction, communication, and sensing. A family of entangled states that features prominently in these applications are graph (or cluster) states. They are key resources in one-way quantum computing paradigms [24, 25] and in quantum error correction [85, 89, 93, 128].

In addition, many quantum repeater schemes [112, 129–132] and quantum sensing protocols [111, 133] rely on graph states. Photonic graph states are especially important because photons are the predominant platform for measurement- and fusion-based computing, and, as flying qubits, they are the only viable choice for quantum networks [109] and quantum imaging [110, 134].

Unfortunately, creating photonic resource states is fundamentally difficult. Because photons do not interact with each other, most attempts have focused on probabilistic generation schemes using linear optics and postselection [135], which are very resource-intensive, severely limiting the size of the resulting states [136, 137]. This bottleneck can in principle be overcome by instead using a deterministic approach in which entangled photons are produced directly from quantum emitters (i.e., matter qubits). One possibility would be to prepare a graph state on emitters [138, 139] and transduce it to photons, but this requires a number of emitters equal to the size of the target photonic graph state. This daunting resource overhead can be avoided by instead using sequential generation schemes. Refs. [140, 141] put forward such an approach that works well for one-dimensional (1D) graph states [142] and has led to experimental demonstrations [4, 143]. However, in the general case where the entanglement structure is more complicated, this method scales exponentially in the size of the target state and can lead to long generation circuits, motivating the search for more efficient approaches. Refs. [144, 145] put forward protocols for 2D lattice graphs that leverage the principle that entangled emitters can emit entangled photons. This idea was extended further to develop protocols that deterministically generate resource states for quantum repeaters [124, 126, 146, 147]—tailored to color centers in Refs. [148, 149]—and one-way computing [29, 150]. Refs. [29, 126] allowed for the re-interference of photons with emitters to further enhance flexibility in entanglement creation.

Despite this progress and the intense interest this approach has generated among experi-

mentalists, existing graph state generation protocols are limited to a small subset of graphs or require a number of emitters that scales linearly with the graph size [150, 151]. This is extremely resource-intensive, especially in light of the schemes for generating repeater graph states presented in Refs. [124, 147], which require only two emitters regardless of the number of photons. The required resources (number of emitters and entangling gates) is a critical factor that determines the practical feasibility of the protocol. For a general graph state, finding resource-efficient generation protocols in polynomial time remains an open problem.

Here, we address this challenge by presenting a general approach to generating arbitrary photonic graph states from quantum emitters. Given a target graph state, we show how to determine in polynomial time both the minimal number of emitters required to create it and an explicit generation protocol. The latter consists of a sequence of gate operations and measurements performed on the emitters. Moreover, our protocol naturally takes into account the order in which photons should be emitted, which can be an important consideration for applications, as it is generally preferable to emit photons in the order they are measured to avoid photon storage. Our method provides a recipe for doing this. The broad applicability of our method, its practical relevance, and its efficient use of resources make it ideally suited to the generation of any photonic graph state from various types of quantum emitters.

3.2.2 Results and Discussion

3.2.2.1 Overview of the algorithm

Determining how to efficiently generate an arbitrary photonic graph state from a set of quantum emitters is highly nontrivial and markedly distinct from the problem of finding an efficient quantum circuit that creates a target state on a register of qubits [152]. Several

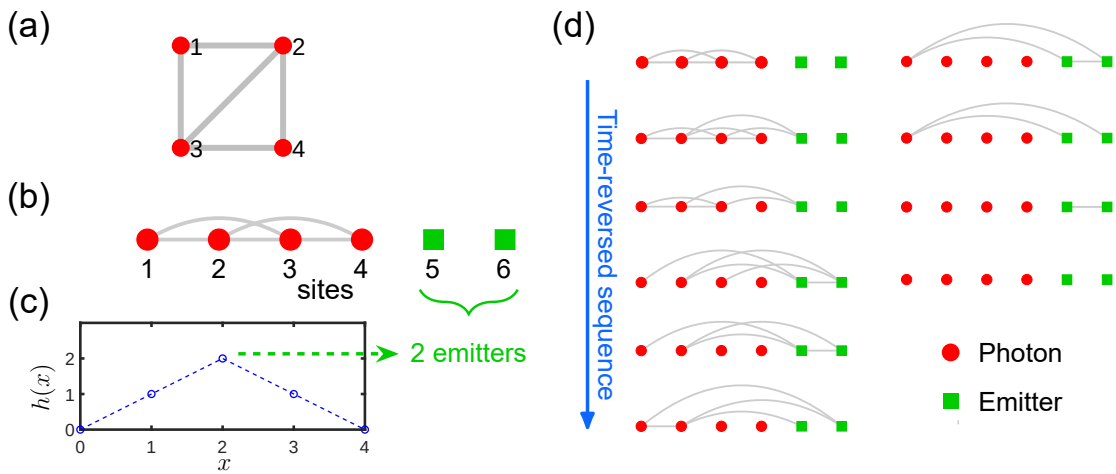

Figure 3.5: Illustration of the protocol solver algorithm. (a) An example of a 4-photon graph state. (b) The graph is mapped to a 1D lattice. (c) The height function is computed and found to have maximum value 2, implying 2 emitters are needed. These are added to the 1D lattice. (d) Starting from the target state and decoupled emitters, a time-reversed sequence of emitter gates, photon absorption events, and time-reversed emitter measurements is constructed, until all qubits are disentangled. Further details about this example can be found in the section 3.2.4. (This figure is adapted from [5].)

additional challenges arise in the former, including the fact that qubits are both created and removed, and that different types of qubits (photons vs. emitters), with different roles and allowed gates, are involved. Depending on the experimental setup, there may also be further restrictions, e.g., emitted photons cannot interact with any other qubits following their emission (although schemes that re-interfere photons with emitters have been proposed [29, 126]). Our method addresses these challenges by leveraging three main ingredients: the notion of the height function (which is related to the entanglement entropy), the stabilizer formalism, and the concept of time-reversed emission events and measurements, which we introduce here.

The first insight is to utilize the so-called height function, which is the entanglement entropy of the system as a function of the partition point when the system is arranged in a 1D lattice and partitioned into two subsystems [106, 107]. This function provides information about

the entanglement structure of the target state as well as the number of emitters required to produce it. The latter is equal to the maximum value of the height function (see below), which depends on the photon emission order. Optimizing this order is NP-hard in general, although we show that heuristic approaches exist for more structured graphs. Moreover, the height function plays a crucial role in determining the sequence of operations (gates and measurements) needed to generate the target graph state from the emitters.

A second key ingredient is the use of gates from the Clifford group. Given that arbitrary graph states can be generated solely with Clifford gates [121, 153], which were also exclusively used in the protocols of Refs. [4, 124, 142, 144–147, 150], restricting ourselves to this set does not affect the generality of our approach. Clifford gates enable the use of the stabilizer formalism, such that we can manipulate Pauli operators instead of keeping track of the whole state. This makes the problem of finding the emission operation sequence tractable, reducing it from exponential to polynomial scaling due to the Gottesman-Knill theorem [100].

A final key element in our algorithm is that we time-reverse the emission sequence. That is, we start from a target multi-photon graph state and an appropriate number of decoupled emitters (obtained from the height function for the target state), and we determine a sequence of emitter gates, "time-reversed measurements", and "photon absorption" events such that the target state is converted to a product state. This is somewhat reminiscent of disentangling circuits used for quantum state tomography of 1D systems [154]. The final state is a product state because, without loss of generality, photons that have not yet been emitted can be described by qubits prepared in the computational basis state $|0\rangle$. Photon emission is then modeled as a two-qubit photon-emitter gate that brings the photon from $|0\rangle$ into an entangled state with the emitters [142]. Because the photon absorption steps are time-reversed versions of photon emission, these too are described by photon-emitter gates.

The run time of the protocol solver algorithm scales as $\mathcal{O}(n_p^4)$, where n_p is the number

of photons in the target graph state. This is a direct consequence of the fact that the algorithm is based on the stabilizer formalism (see Methods section). This is in contrast to previous methods [140, 141], which scale exponentially in n_p due to the need to perform singular value decompositions repeatedly. We also show that the number of gates in the final emission sequence scales at most as $\mathcal{O}(n_p^2)$ (see Methods). However, this assumes two-qubit gates can be applied between any pair of emitters. If this is not the case, then additional SWAP operations are needed, bringing the gate count up to $\mathcal{O}(n_p^3)$. Therefore, both the protocol solver and the resulting gate sequence it obtains scale polynomially in the size of the target graph state.

Now we provide a more detailed description of the protocol solver algorithm. We begin with a target graph state $|\psi_p\rangle$ of n_p photons and n_e decoupled emitters, so that the total state is $|\Psi\rangle = |\psi_p\rangle \otimes |0\rangle^{\otimes n_e}$. An $n_p = 4$ photon example graph is shown in Fig. 3.5(a). This is what the state of the total system should be at the end of the generation sequence. n_p is set by the size of the desired photonic graph state $|\psi_p\rangle$, while n_e remains to be determined. We assume the graph representing $|\psi_p\rangle$ is connected; if this is not the case, then the algorithm can be run separately for each connected subgraph. The state $|\Psi\rangle$ is fully described by a set of $n = n_p + n_e$ stabilizers g_m, $m = 1, \ldots, n$, defined such that $g_m |\Psi\rangle = |\Psi\rangle$. The full set of n qubits can be arranged in a 1D lattice with site index $x \in \{0, 1, 2, \ldots, n\}$ (see Fig. 3.5(b)). Sites $x = 1, \ldots, n_p$ correspond to the photons and are ordered according to the desired photon emission ordering, while the sites $x = n_p + 1, \ldots, n$ are the emitters. The additional $x = 0$ site is included as a matter of convention. We can now define the height function $h(x) = S_A$ to be the bipartite entanglement entropy when the 1D lattice is divided into the subregion $A = \{1, 2, \ldots, x\}$ and its complement. Note that $S_A = \frac{1}{1-\alpha} \log_2 \mathrm{Tr}(\rho_A^\alpha)$ can be any of the Rényi entropies; for stabilizer states, they are all equal [30]. In Ref. [140], it was shown that the state of the emitted photons, $|\psi_p\rangle$, can be represented by a matrix

product state (MPS) with bond dimension 2^{n_e}. Because the entanglement entropy of a MPS is given by the base-2 logarithm of the bond dimension [155], it follows that n_e is equal to the maximum value of $h(x)$. The height function for the graph in Fig. 3.5(a) is shown in Fig. 3.5(c). In this example, its maximum is 2, implying 2 emitters are needed. In general, the maximum of the height function is in fact the minimal number of emitters capable of generating the target graph state, as fewer emitters would be insufficient to match the bond dimension of any exact MPS representation.

The height function can be computed efficiently from the stabilizers. Because products of stabilizers are also stabilizers, there are many equivalent choices for the set $\{g_m\}$. Here, we focus on a particular choice of the stabilizers that we refer to as the echelon gauge [102], in which the stabilizer matrix has a row-reduced echelon form (see Methods). When the g_m are in this gauge, the height function can be expressed as [102]

$$h(x) = n - x - \#\{g_m | \mathtt{l}(g_m) > x\}, \tag{3.6}$$

where $\mathtt{l}(g_m)$ is the index of the left-most (smallest index) site on which g_m acts nontrivially. The last term in Eq. (3.6) counts the number of stabilizers that act nontrivially only on sites to the right of (i.e., larger than) x. Although Eq. (3.6) depends on n_e, this dependence cancels out for states like $|\Psi\rangle$ in which the emitters are decoupled. Therefore we can obtain n_e from the maximum of $h(x)$ on the photonic sites, using only the stabilizers of $|\psi_p\rangle$.

Once we have the number of emitters n_e, we can run the protocol solver algorithm to determine the sequence of gates, time-reversed measurements, and photon absorption events needed to transform the target state $|\Psi\rangle$ into the initial state $|0\rangle^{\otimes n}$, which corresponds to decoupled emitters and no photons. We first introduce a photon index j and initialize it to $j = n_p$. The algorithm then consists of four steps:

1. Transform the stabilizers g_m into echelon gauge if they are not already, then compute the height function $h(x)$.

2. If $h(j) \geq h(j-1)$, skip to step (iii). Otherwise apply a time-reversed measurement and update the g_m accordingly.

3. Apply a photon absorption operation on the j-th photon and update the g_m accordingly. If $j > 1$, then set $j \to j-1$ and go to step (i). Otherwise, go to step (iv).

4. All photons are now in state $|0\rangle$. Apply a series of gates on the emitters to disentangle them, bringing the total state to $|0\rangle^{\otimes n}$.

This algorithm involves repeated applications of two basic operational primitives: time-reversed measurement and photon absorption. During the algorithm, the height function of the current state tells us which of these we need to perform next to bring the state closer to $|0\rangle^{\otimes n}$. Each photon absorption step disentangles one photon qubit from the rest, starting with the last-emitted photon, $j = n_p$, and working down to the first photon, $j = 1$. For our 4-photon example, the graphs at intermediate steps of the algorithm are shown in Fig. 3.5(d). A step by step explanation of this example is given in the section 3.2.4. When the algorithm concludes, we can reverse the entire sequence to obtain an operation sequence that generates $|\psi_p\rangle$ starting from n_e decoupled emitters. We now describe each of the two operational primitives in more detail, the precise gates they introduce into the generation sequence, and their connection to the height function.

Photon absorption of the j-th photon refers to a time-reversed version of photon emission. For concreteness, we focus on the case where emission is described by a CNOT gate between the photon and its emitter (with the emitter as the control), as in Ref. [142] (also see Fig. 3.4), although our algorithm can be adapted to any Clifford gate describing photon emission. Mathematically, the task of absorbing photon j requires finding a stabilizer g_a

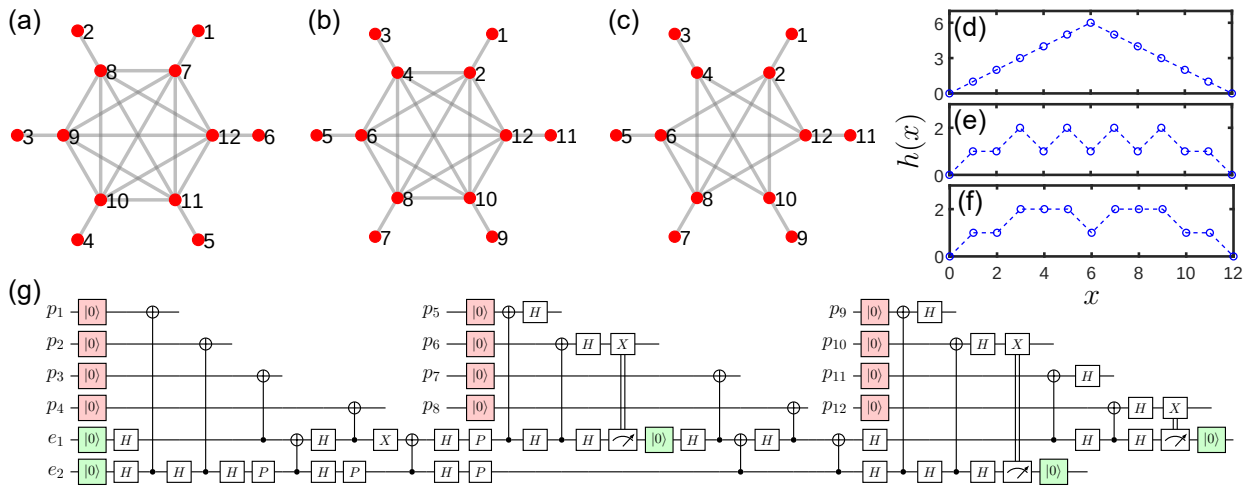

Figure 3.6: **Results for repeater graph states.** (a) 12-photon repeater graph state in which external photons are emitted first. (b) Same graph state as in (a), but with "natural" emission ordering. (c) Same graph state as in (b) but with some unnecessary edges deleted. (d), (e) and (f) show the height functions of the states in (a), (b) and (c), respectively. (g) Emission circuit for state shown in (c), where H is the Hadamard gate, $P = \mathrm{diag}(1, i)$ is the phase gate, and $X \equiv \sigma^x$. (This figure is adapted from [5].)

that can be transformed to σ_j^z by applying CNOT_{ij}, where i is an emitter site. It is possible to find such a stabilizer when $h(j) \geq h(j-1)$. From Eq. (3.6), we see that this condition implies there *must be* at least one stabilizer, g_a, such that $\mathtt{l}(g_a) = j$. This stabilizer has the form

$$g_a = \pm \sigma_j^{\alpha} \sigma_{i_1}^{\beta_1} \cdots \sigma_{i_s}^{\beta_s}, \tag{3.7}$$

where $\alpha, \beta_k \in \{x, y, z\}$ label the nontrivial Pauli operators, and $1 \leq j \leq n_p < i_1 < \cdots < i_s \leq n$. Note that we can assume g_a acts trivially on all photons with index larger than j since these have already been decoupled at this point in the algorithm. We also assume that g_a acts nontrivially on at least one emitter site; if this is not the case, then photon absorption is unnecessary since the j-th photon is then already disconnected. To transform g_a into σ_j^z, we can first apply a local Clifford operation on the j-th site and general Clifford operations on the emitters to transform $g_a \to \sigma_j^z \sigma_i^z$, where $i > n_p$ is an emitter site. This can be done

for example by applying local Clifford operations to transform g_a to $\sigma_j^z \sigma_{i_1}^z \cdots \sigma_{i_s}^z$, and then applying CNOT gates on pairs of emitters to transform this to $\sigma_j^z \sigma_i^z$. Applying CNOT_{ij} brings this to σ_j^z, completing the absorption of the j-th photon. Note that we can choose any emitter to absorb the photon; typically, the emitter that requires the shortest circuit to transform g_a into σ_j^z is preferred. The resulting circuit is included in the time-reversed generation sequence.

Time-reversed measurements are applied whenever $h(j) < h(j-1)$, in which case photon absorption is not possible. Indeed, in this case, Eq. (3.6) implies $\#\{g_m | \mathtt{l}(g_m) = j\} = 0$, or in other words, a suitable g_a does not exist. In order to absorb the next photon, we must therefore first find a way to increase $h(j)$ relative to $h(j-1)$. This can be accomplished with a time-reversed measurement on an emitter. To perform this operation, we first rotate the state to $|\Phi\rangle \otimes |0\rangle_i$, where $|\Phi\rangle$ is a stabilizer state involving photons $1, \ldots, j$ and emitters other than i. This can always be done using $\mathcal{O}(n_e)$ Clifford gates on emitters when $h(j) < h(j-1)$ (see Methods). Now notice that this state is obtained from the pre-measurement state $\mathrm{CNOT}_{ij} |\Phi\rangle \otimes |+\rangle_i$ when emitter i is measured to be in the state $|0\rangle_i$. Therefore, starting from $|\Phi\rangle \otimes |0\rangle_i$, if we perform a Hadamard gate on emitter i followed by the gate CNOT_{ij}, we effectively reverse the measurement on the emitter. These operations transform the stabilizers g_m in such a way that $h(j)$ now satisfies $h(j) \geq h(j-1)$ (see Methods), and we can proceed with the next photon absorption. The emitter gates, Hadamard on i, and CNOT_{ij} are all included in the time-reversed generation sequence.

3.2.2.2 Examples

We demonstrate our algorithm with several examples. The first is the important case of repeater graph states [112], where we use our algorithm to obtain generation protocols that are more efficient than previously known ones. As a second example, we consider random

graphs containing up to hundreds of photons and demonstrate the polynomial scaling of the resulting generation circuits. Additional examples, including modified repeater graph states, error correcting codes, and a simple example that illustrates the algorithm in detail can be found in section 3.2.4.

Next, we apply our algorithm to find operation sequences that produce repeater graph states [112]. In addition to its importance in quantum network applications, this example also illustrates how different photon emission orderings impact the required number of emitters. Ref. [124] presented a generation protocol for a particular ordering that was devised essentially through guesswork. Our algorithm can be used to systematically find protocols for any ordering. An example of a 12-photon repeater graph state is shown in Fig. 3.6(a). The graph contains a fully connected core of 6 photons, each of which is connected to a single external photon. Bell measurements are performed on pairs of these external photons, where the two photons in each pair come from different graph states. If a Bell measurement succeeds, then the two corresponding core photons are linked by an edge, and entanglement extends across two nodes of the repeater network. Having multiple external photons provides built-in redundancy that increases the likelihood that at least one Bell measurement between two repeater graph states is successful. Upon success, core photons are then measured in the z or x basis to remove photons connected to failed measurements or to create entanglement links between successful measurements, respectively. Because the external photons are measured first, it may be advantageous to emit these first when generating the graph state to reduce photon storage requirements. This corresponds to the photon ordering shown in Fig. 3.6(a). The height function for this graph and photon ordering is shown in Fig. 3.6(d), where it is evident that 6 emitters are needed to produce the state. However, if efficient photon storage is available, then the ordering shown in Fig. 3.6(b) may be preferable, where now external and core photons are emitted in an alternating sequence. This ordering reduces the number

of emitters down to only 2, as shown in Fig. 3.6(e). As we discuss further below, this illustrates our general finding that "natural" orderings in which neighboring vertices are emitted around the same time reduce the requisite number of emitters. This reduction in quantum resources becomes still more dramatic as the size of the graph increases; for orderings as shown in Fig. 3.6(a), the number of emitters scales linearly with photon number, while for the natural ordering of Fig. 3.6(b), the number of emitters remains at 2 regardless of the number of photons. This is shown explicitly in the section 3.2.4.

As discussed in Ref. [150], some of the edges in the repeater graph can be removed without affecting the functionality of the repeater. Fig. 3.6(c) shows an example of this in which 4 of the core edges are deleted. As shown in Fig. 3.6(f), the number of emitters is still 2. However, removing the redundant edges reduces the depth of the resulting generation circuit, which is shown in Fig. 3.6(g). This circuit contains 4 CNOTs between emitters and 1 intermediate measurement on an emitter, whereas the original protocol presented in Ref. [124] requires 5 two-qubit gates and 5 intermediate measurements.

To demonstrate how our algorithm scales with the number of photons in the target state, we run it for random graphs ranging in size from $n_p = 16$ to $n_p = 256$ photons. These graphs are produced randomly using the Erdös–Rényi model [156]. In this approach, each random graph is constructed by connecting n_p vertices randomly with fixed probability p. We discard any graphs that contain disconnected vertices when sampling these realizations. The likelihood that such graphs arise becomes very small if p is chosen sufficiently close to 1. In Fig. 3.7, we show the maximum value, $h_{\max}$, of the height function averaged over 1024 realizations for each value of n_p. Averaged measurement and gate counts are also shown. It is evident that $h_{\max}$, and hence the number of emitters, scales linearly with n_p as n_p becomes large. The same is also true of the number of measurements. On the other hand, the number of CNOTs and the total number of gates in the resulting generation circuits scale

quadratically with the number of photons in the target state. These results confirm both the polynomial scaling of our algorithm, which allows us to easily find generation protocols for graph states containing hundreds of photons, and the polynomial scaling of the resulting protocols, which makes them practical for near-term experiments.

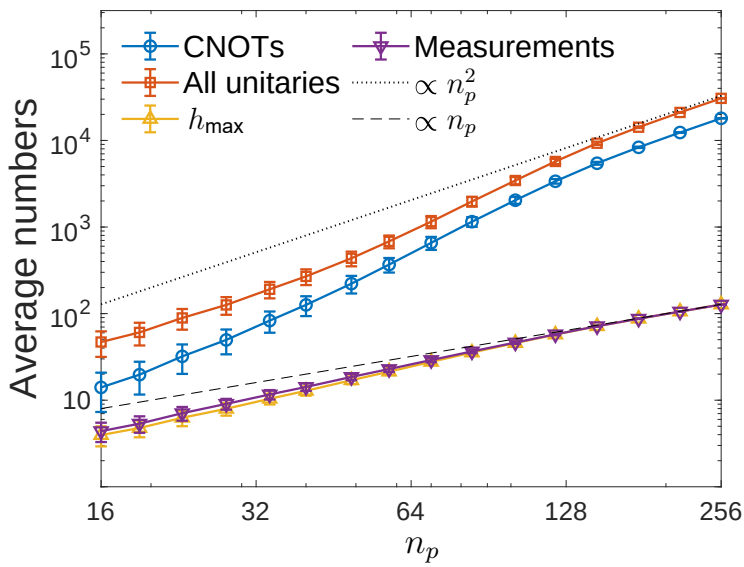

Figure 3.7: Scaling of emitter number and generation circuit depth. The maximum value of the height function $h_{\max}$, measurement counts, and gate counts needed to produce random graphs of size n_p are all averaged over 1024 graph realizations for each value of n_p drawn from an Erdös–Rényi ensemble with edge probability $p = 0.95$. Dashed curves are included to show the scaling with n_p and n_p^2. The error bars stand for the standard deviation of these realizations. (This figure is adapted from [5].)

3.2.2.3 Photon emission ordering

A powerful feature of our algorithm is that it readily incorporates a desired photon emission ordering. This is encoded when we arrange the photons and emitters in a 1D lattice to define the height function. If no specific ordering is preferred, then ideally we would want to choose the ordering that minimizes the number of emitters n_e. However, the task of finding this optimal ordering is NP-hard, as we show in Methods. Nevertheless, one can still look for

heuristic solutions to the problem. In fact, the expression for the height function in Eq. (3.6) makes it clear that this function is suppressed for orderings in which the stabilizers, when expressed in the echelon gauge, are supported predominantly on high-index sites on the right side of the 1D lattice. This tends to occur for "natural" orderings in which neighboring photons in the graph are emitted around the same time, because in this case the stabilizers are localized on the 1D lattice. This was illustrated with our repeater graph state example in the previous section. The extent to which the stabilizers can be localized in this way depends on the graph of course. For an $N \times M$ square lattice, it is inevitable that some neighboring vertices will be separated by M steps in the emission sequence (assuming $M < N$), and so the number of emitters is of order M. On the other hand, for other graph structures like those of the repeater graph states, far fewer emitters may be needed, provided a natural photon ordering is used. Note that in this example, as for many graphs, edges between remote vertices cannot be avoided (see Fig. 3.6(b)). Despite this, we showed that optimal orderings for which the height function remains small can still be found. Thus, emitting neighboring vertices around the same time is sufficient but not always necessary to keep the number of emitters small.

In summary, we presented an efficient algorithm to construct polynomial-depth operation sequences that produce arbitrary multi-photon graph states from a minimal number of quantum emitters. By reducing both the number of photon sources and the number of quantum operations that need to be performed on them, our method brings the wide range of quantum information applications that rely on entangled photon resource states closer to experimental reality.

3.2.3 Methods

3.2.3.1 Echelon gauge

The echelon gauge was first defined in [102], where it was called row reduced echelon form. In this gauge, the stabilizer tableau has a recursive row-reduced form based on the following three types of matrices:

$$\left(\begin{array}{c|c} \mathbb{1} & * \cdots * \\ \hline \mathbb{1} & \\ \vdots & M \\ \mathbb{1} & \end{array}\right), \quad \left(\begin{array}{c|c} \sigma & * \cdots * \\ \hline \mathbb{1} & \\ \vdots & M \\ \mathbb{1} & \end{array}\right), \quad \left(\begin{array}{c|c} \sigma_1 & * \cdots * \\ \sigma_2 & * \cdots * \\ \hline \mathbb{1} & \\ \vdots & M \\ \mathbb{1} & \end{array}\right), \tag{3.8}$$

where σ, σ_1, and σ_2 are nontrivial Pauli matrices, and $\sigma_1 \neq \sigma_2$. In this work, we always choose $\sigma_2 = \sigma^z$, and σ_1 can be either σ^x or σ^y. The full tableau cannot have the first form shown above (with only identities in the first column), because this case does not apply to pure states. However, the submatrix M can follow any of the above three patterns, and the structure iterates recursively. The stabilizers can be transformed into this gauge starting from any other by performing a series of row reductions, as described in Ref. [102]. In the echelon gauge, the independent stabilizers acting on $\bar{A} = \{x+1, \ldots, n\}$ appear at the bottom right of the tableau. Therefore, starting from the formula for the entanglement entropy for subregion $\bar{A}$ of a stabilizer state [157], $S_{\bar{A}} = n_{\bar{A}} - |\mathcal{G}_{\bar{A}}|$, where $n_{\bar{A}}$ is the size of $\bar{A}$ and $|\mathcal{G}_{\bar{A}}|$ is the number of independent stabilizers acting on $\bar{A}$, and using $h(x) = S_A = S_{\bar{A}}$, we obtain Eq. (3.6).

3.2.3.2 Time-reversed measurements

Above, we saw that when the total state of the system has the form $|\Phi\rangle \otimes |0\rangle_i$, where i is an emitter site, we can perform a time-reversed measurement to convert this to the pre-measurement state $\mathrm{CNOT}_{ij} |\Phi\rangle \otimes |+\rangle_i$. Here, we clarify two important questions regarding this process: (i) When and how can we bring the system into the state $|\Phi\rangle \otimes |0\rangle_i$? (ii) How can we see that a time-reversed measurement on this state increases $h(j)$, as needed for a subsequent photon absorption process?

Regarding question (i), when $h(j) < h(j-1)$, we can always find a set of Clifford gates that act purely on the emitters that will transform the state of the system into $|\Phi\rangle \otimes |0\rangle_i$. To see this, first note that $h(j) = h(n_p)$, as follows from Eq. (3.6) when photons $j+1$ through n_p are in state $|0\rangle$. Using that the height function is bounded from above by n_e, we then have $h(n_p) = h(j) < h(j-1) \leq n_e$. On the other hand, from Eq. (3.6) we have $h(n_p) = n_e - \#\{g_m | \mathtt{l}(g_m) > n_p\}$. Together, these results imply $\#\{g_m | \mathtt{l}(g_m) > n_p\} > 0$, or in other words, there is at least one stabilizer that is supported solely on the emitter sites. We can therefore transform this stabilizer into σ_i^z using at most $\mathcal{O}(n_e)$ Clifford gates on the emitters, bringing the state to $|\Phi\rangle \otimes |0\rangle_i$. We can then convert this stabilizer to σ_i^x by applying a Hadamard gate on site i. This prepares the system for the second part of the time-reversed measurement process, which is the gate CNOT_{ij}.

We answer question (ii) by proving the following theorem:

Theorem 3.1. *If $h(j) < h(j-1)$ and the i-th qubit $(i > j)$ is stabilized by σ_i^x, then applying CNOT_{ij} will boost $h(x) \to h(x) + 1$, $\forall x \in \{j, j+1, \cdots, i-1\}$.*

Proof We are assuming that $h(j) < h(j-1)$, which from Eq. (3.6) implies $\#\{g_m | \mathtt{l}(g_m) = j\} = 0$. Now consider how the stabilizers transform under CNOT_{ij}. If $\mathtt{l}(g_m) < j$ before the gate, then $\mathtt{l}(g_m)$ remains invariant, and the contributions of these stabilizers to $h(x)$ remain the same after the gate. The only potential changes to $h(x)$ come from stabilizers g_m for which $\mathtt{l}(g_m) > j$. These stabilizers necessarily have $\mathbb{1}$ on the j-th site. Stabilizers among this set that have $\mathbb{1}$ or σ_i^z on the i-th site will be unchanged by the CNOT_{ij} gate. However, if one or more of these stabilizers have σ_i^x or σ_i^y before the gate, then afterward, these stabilizers will contain σ_j^x. Consequently, $h(j)$ increases, while $h(j-1)$ remains the same. In the echelon gauge, there can only be one stabilizer with σ_j^x as the left-most nontrivial Pauli. Therefore, $h(j) \to h(j) + 1$ when CNOT_{ij} is applied. Moreover, if the i-th qubit is stabilized by σ_i^x, then this becomes $\sigma_j^x \sigma_i^x$ after the gate, and so the height function for all sites between $j-1$ and i increases: $h(x) \to h(x) + 1 \; \forall x \in \{j, j+1, \cdots, i-1\}$. $\square$

3.2.3.3 Scaling analyses

Here, we determine the complexity of both the protocol solver algorithm itself and the resulting graph state generation circuit. Regarding the algorithm, the main factor that determines the complexity is the need to restore the stabilizers to the echelon gauge after each operation is applied. Transforming a n-qubit stabilizer state into the echelon gauge generally requires $\mathcal{O}(n^3)$ steps, which is the complexity of Gaussian elimination. Another important factor is the process of determining which gates need to be applied in preparation for photon absorption or time-reversed measurement. Solving for each set of gates takes no more than $\mathcal{O}(n_e n)$ steps, which is the number of entries in the emitter part of the stabilizer tableau. Thus, the Gaussian eliminations needed to restore echelon gauge dominate the scaling. In the worst case where $n_e \propto n$, our algorithm will then take $\mathcal{O}(n^4)$ steps, where the additional factor of n comes from the fact that the algorithm requires $\mathcal{O}(n_p) \sim \mathcal{O}(n)$

iterations.

As for the complexity of the output generation circuit, there are at most $\mathcal{O}(n_e)$ operations between any two-photon emissions. For example, $\mathcal{O}(n_e)$ gates are needed to transform g_a into the appropriate form for photon absorption. Thus, the depth of the circuit acting on the emitter qubits is at most $\mathcal{O}(n_p n_e)$. In the worst case where $n_e \sim n_p$, the scaling is then $\mathcal{O}(n_p^2)$, which is consistent with Fig. 3.7. Nevertheless, due to the fact that some long-range two-qubit gates may arise, and given that these are usually decomposed as $\mathcal{O}(n_e)$ short-ranged two-qubit gates in real devices, the overall circuit depth may become $\mathcal{O}(n_p n_e^2)$.

3.2.3.4 Complexity of finding optimal photon emission orderings

We can show that the task of finding optimal emission orderings is NP-hard by mapping this to a known graph theory problem. Define Γ_{ij} to be the adjacency matrix of the graph representing the target state $|\Psi\rangle$. Ref. [30] showed that we can obtain the height function from Γ_{ij} using the formula $h(x) = \text{rank}_2(\Gamma_{A\bar{A}})$, where $\Gamma_{A\bar{A}}$ is the sub-matrix of Γ_{ij} with row indices $i \in A = \{1, 2, \cdots, x\}$ and column indices $j \in \bar{A}$. Note that this expression does not simplify the computation of $h(x)$; it can take more steps to find the maximum compared to using Eq. (3.6) since the former performs Gaussian eliminations for $\mathcal{O}(n_p)$ rounds, while the latter only takes one round. However, the optimized maximum value of this alternative expression for $h(x)$ (i.e., $\max_x h(x)$) is precisely equal to a graph theoretic property known as linear rank-width (LRW) [158]. The task of finding an optimal photon emission ordering is therefore equivalent to finding LRW through the graph isomorphism, which has long been studied in coding theory in the context of optimizing block code trellises [159]. Unfortunately, determining whether a simple connected graph has an LRW bounded from above by a positive integer k has been shown to be NP-complete [160, 161]. Therefore, it is unlikely this problem can be solved efficiently for large, arbitrary photonic graph states

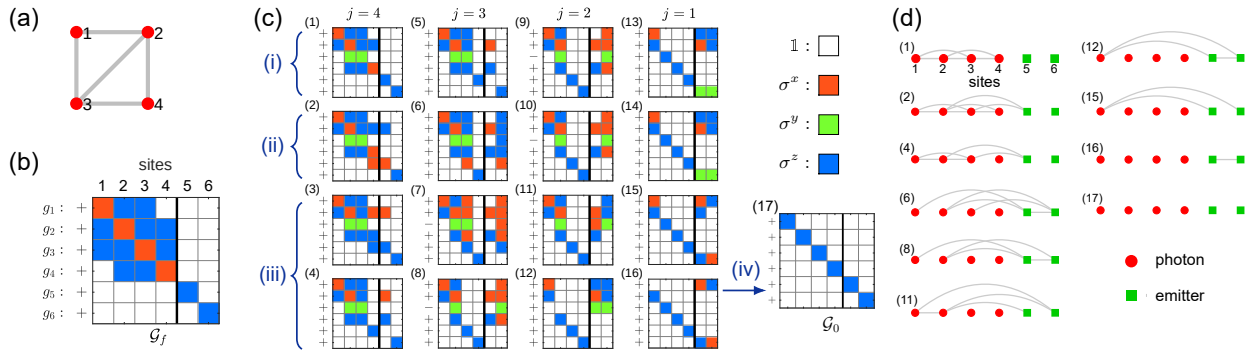

Figure 3.8: Step-by-step illustration of the protocol solver. (a) A target graph state with 4 photons. (b) The set of generators $\mathcal{G}_f = \{g_m\}$ is depicted as a tableau in which each row corresponds to one generator. Different colors correspond to different Pauli operators. The first 4 columns correspond to photonic qubits, and the last 2 columns correspond to emitters. (c) Step by step demonstration of how to obtain the time-reversed generation sequence, where $\mathcal{G}_0 = \{\sigma_i^z\}$ is finally obtained. Explanations are in the main text. (d) Local Clifford equivalent graph state representations of tableaux in (c). (This figure is adapted from [5].)

unless P = NP. Nevertheless, if the parameter k is set to 1, this problem can be answered in polynomial time [162]. If the parameter k is set to larger values, a recent work [161] showed that this problem can be reduced to a fixed parameter tractable problem. Specifically, its answer, along with the sequence solution (if it exists), can be determined in $\mathcal{O}(f(k)n_p^3)$ steps, where $f(k)$ is an exponentially large function of k. However, the growth of $f(k)$ is so rapid that this result is not likely to be of practical use for photonic graph state generation.

3.2.4 Supplemental Notes

3.2.4.1 Supplementary Note 1

This section contains several additional examples of generation protocols produced using our algorithm. We begin with a simple example that illustrates in detail how our algorithm works. We then provide solutions for more complicated examples of practical importance, including error correcting codes and repeater graph states of arbitrary size. These more

complicated examples are solved numerically using MATLAB codes that are available on GitHub [163]. This code expresses the generation sequence in terms of an MPS [140] for bookkeeping purposes:

$$|\Psi\rangle = U_{p,\text{tot.}}\langle\psi_f|\Big[\prod_{j=1}^{n_p}\Big(\hat{M}_j U_{e,j}\hat{E}_{\eta_j}\Big)\Big]W_0|\psi_0\rangle, \tag{3.9}$$

in which the initial and final states of emitter qubits are simply product states of $|0\rangle$: $|\psi_f\rangle = |\psi_0\rangle = |0\rangle^{\otimes n_e}$. We denote η_j as the emitter qubit that emits the j-th photon and μ_j as the emitter qubit that is measured after emitting the j-th photon. $\hat{E}_{\eta_j}$ is the emission tensor, $\hat{E}_{\eta_j} = |0\rangle_j\,|0\rangle_{\eta_j}\langle 0|_{\eta_j} + |1\rangle_j\,|1\rangle_{\eta_j}\langle 1|_{\eta_j}$, that describes emission of photon j from emitter η_j, which can be represented as $\text{CNOT}_{\eta_j,j}$. $U_{e,j}$ is the unitary operation obtained from the j-th photon absorption step, which transforms g_a as explained in the main text (Sec.II.A). $\hat{M}_j$ is identity if no measurement happens (μ_j is not assigned), otherwise, $\hat{M}_j = W_j H_{\mu_j} X_{\mu_j}^{s_j}\hat{\pi}_{\mu_j}$, with projection $\hat{\pi}_{\mu_j} \equiv \frac{1}{2}[\mathbb{1}+(-1)^{s_j}Z_{\mu_j}]$ and its random outcome $s_j \in \{0,1\}$. Here, W_j is the unitary operation that is obtained from time-reversed measurement (Sec.IV.B), and W_0 is the unitary operation that disentangles all emitters at the final stage of the time-reversed sequence. Finally, $U_{p,\text{tot}} = \prod_j \left(X_j^{s_j}U_{p,j}\right)$ is the local Clifford operation that acts on photons with conditional $X_j^{s_j}$ flipping. The profile of the solution is stored as $\{U_{e,j}, U_{p,j}, \mu_j, \eta_j, W_j, W_0\}$. We note that such a solution is usually not unique due to there being multiple choices for how to choose the emitter gates and emitter sites in each photon absorption and time-reversed measurement.

As discussed in the main text, the height function plays a central role in determining the number of emitters and the operation sequence needed to generate a target photonic graph state. As shown in Eq. (1) of the main text, when the stabilizers g_m are in the echelon gauge,

the height function can be expressed as

$$h(x) = n - x - \#\{g_m | \mathtt{l}(g_m) > x\}, \tag{3.10}$$

where $\mathtt{l}(g_m)$ is the index of the left-most (smallest index) site on which g_m acts nontrivially. In the main text, we showed that the difference in the height function across adjacent sites determines whether we perform a photon absorption or a time-reversed measurement at each step of the algorithm. Therefore, we define

$$\delta h(x) \equiv h(x) - h(x-1) = \#\{g_m | \mathtt{l}(g_m) = x\} - 1, \tag{3.11}$$

from which it is apparent that this difference only depends on the number of stabilizers (in the echelon gauge) that have a left-ending on site x.

We begin by demonstrating our protocol solver algorithm in the case of the simple 4-photon graph state displayed in Fig. 3.8(a). The stabilizers are given by

$$\begin{aligned} g_1 &= \sigma_1^x \sigma_2^z \sigma_3^z, \quad g_2 = \sigma_1^z \sigma_2^x \sigma_3^z \sigma_4^z, \\ g_3 &= \sigma_1^z \sigma_2^z \sigma_3^x \sigma_4^z, \quad g_4 = \sigma_2^z \sigma_3^z \sigma_4^x. \end{aligned} \tag{3.12}$$

We can switch to the echelon gauge by redefining $g_3 \to g_2 g_3$. We then calculate the height function using Eq. (3.10), finding that the maximum is 2. Therefore, at least $n_e = 2$ emitter qubits are needed, and so we assemble a 6-qubit lattice. We can depict the complete set of 6 stabilizers as a tableau, as shown in Fig. 3.8(b).

In Fig. 3.8(c), we first obtain inset (1) by transforming Fig. 3.8(b) to the echelon gauge. The upper left sub-block of the tableau is exactly Eq. (3.12) with $g_3 \to g_2 g_3$. Next we describe in detail how the generator set is updated from inset (1) to inset (17) step by step. The

column label j indicates which photon we are currently focusing on, and the labels (i),...,(iv) indicate the specific step of our algorithm. For each photon, we do the following steps:

- $j = 4$: (i) Obtain inset (1) by transforming to echelon gauge: $g_3 \to g_2 g_3$. (ii) Eq. (3.11) gives $\delta h(4) = -1$. Perform a time-reversed measurement on emitter site 5 by applying a Hadamard H_5 followed by CNOT_{54}, which yields inset (2). (iii) Let $g_a = g_5 = \sigma_4^x \sigma_5^x$ in inset (2). One gets inset (3) by performing Hadamards on sites 4 and 5. Then the 4-th photon is absorbed into the emitter on site 5 by applying CNOT_{54}. Replace $g_4 \to g_4 g_5$ to eliminate the redundant σ_4^z, yielding inset (4). ($\mu_4 = 5$, $\eta_4 = 5$, $U_{p,4} = H_4$, $U_{e,4} = H_5$, $W_4 = H_5$.)

- $j = 3$: (i) Skip this step since inset (4) is already in echelon gauge. (ii) Eq. (3.11) gives $\delta h(3) = -1$. Perform a time-reversed measurement on emitter site 6 by applying H_6 followed by CNOT_{63}. Inset (6) is then obtained by redefining $g_5 \leftrightarrow g_6$. (iii) Let $g_a = g_5 = \sigma_3^x \sigma_6^x$ in inset (6). One gets inset (7) by applying Hadamards on sites 3 and 6. Then the 3rd photon is absorbed by applying CNOT_{63}. Replace $g_3 \to g_3 g_5$ to eliminate the redundant σ_3^z. Thus, inset (7) becomes (8). ($\mu_j = 6$, $\eta_3 = 6$, $U_{p,3} = H_3$, $U_{e,3} = H_6$, $W_3 = H_6$.)

- $j = 2$: (i) Skip this step since inset (8) is already in echelon gauge. (ii) Skip this step since Eq. (3.11) gives $\delta h(2) = 1$. (iii) Choose $g_a = g_4 = \sigma_2^z \sigma_5^z \sigma_6^x$ in inset (10). One gets inset (11) by applying H_6 followed by CNOT_{65} on the emitters, so that $g_a \to \sigma_2^z \sigma_5^z$. Then the 2nd photon is absorbed into emitter 5 by applying CNOT_{52}. Redefine $g_k \to g_k g_4$ for $k = 1, 3$ to eliminate the redundant σ^z's. Thus, inset (11) becomes (12). ($\eta_2 = 5$, $U_{p,2} = \mathbb{1}$, $U_{e,2} = H_6 \text{CNOT}_{65}$, $\hat{M}_2 = \mathbb{1}$.)

- $j = 1$: (i) Obtain inset (13) from (12) by transforming to echelon gauge: $(g_3, g_4, g_5, g_6) \to (g_4, g_5, g_6, g_3)$. (ii) Skip this step since Eq. (3.11) gives $\delta h(1) = 1$. (iii) Choose

$g_a = g_2 = \sigma_1^z \sigma_5^x \sigma_6^z$ in inset (14). One gets inset (15) by applying H_5 and then CNOT_{65} to transform $g_a \to \sigma_1^z \sigma_5^z$. Then the 1st photon is absorbed into emitter site 5 by applying CNOT_{51}. Thus, inset (15) becomes (16). ($\eta_1 = 5$, $U_{p,1} = \mathbb{1}$, $U_{e,1} = H_5 \text{CNOT}_{65}$, $\hat{M}_1 = \mathbb{1}$.)

- (iv) Finally, to recover the state $|0\rangle^{\otimes n}$, one needs to disentangle the emitter qubits. This can be done with the following gate sequence: $H_5 \text{CNOT}_{56} H_5$. In the last step, we permute the g_m to obtain inset (17). ($W_0 = H_6 \text{CNOT}_{56} H_5$.)

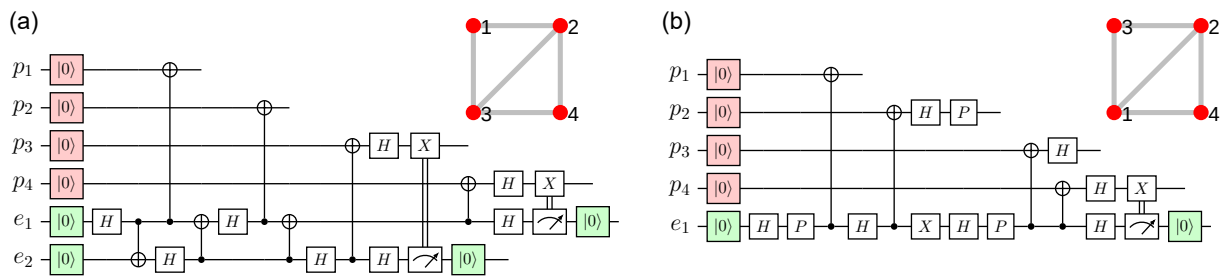

Figure 3.9: Graph state generation circuits for the 4-photon example graph shown in Fig. 3.8. In this figure, p_j ($j = 1, 2, 3, 4$) labels different photonic qubits, and e_1 and e_2 are emitter qubits. At the end of each circuit, the photon qubits are in the target graph state displayed at the top right, while the emitter qubits are in state $|0\rangle$ after the measurements. (a) The emission circuit obtained from the steps in Fig. 3.8. (b) A different generation circuit that produces the same target graph state as in (a). This circuit is obtained by swapping qubits $1 \leftrightarrow 3$, resulting in a circuit that requires only one emitter. (This figure is adapted from [5].)

Now that the algorithm is complete, we reverse all the operations to obtain the final generation sequence. This circuit is shown in Fig. 3.9(a). It is worth noting that, in this example, the emission sequence can be further optimized by swapping the 1st and 3rd photons in the emission order, such that the maximum of $h(x)$ is reduced to 1. Thus, only one emitter qubit is needed in this case, and the corresponding generation circuit is displayed in Fig. 3.9(b).

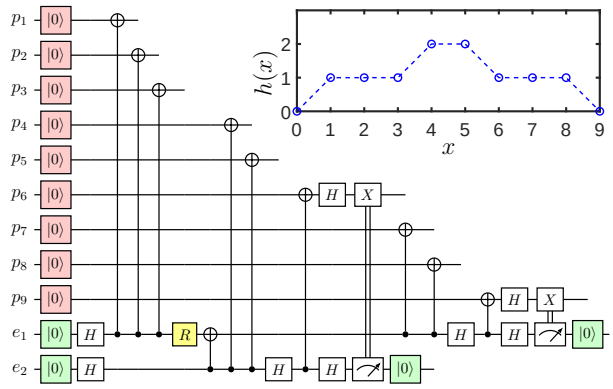

Figure 3.10: The emission circuit that generates a logical state of the Shor code, controlled by a local operation R (the yellow block). The inset displays the height function of $|\pm\rangle_L$, which has $h_{\max} = 2$. (This figure is adapted from [5].)

3.2.4.2 Supplementary Note 2

In this subsection, we demonstrate how to generate a useful quantum error correction code, with some continuous logical rotation. In particular, we present an emission sequence for the Shor code [89] with 9 photonic qubits, which is able to protect a qubit from single bit-flip and phase-flip errors. The stabilizer generators of this code are well known: $g_j = \sigma_j^z \sigma_{j+1}^z$ for $j = 1, 2, 4, 5, 7, 8$, and $g_3 = \sigma_1^x \sigma_2^x \cdots \sigma_6^x$, $g_6 = \sigma_4^x \sigma_5^x \cdots \sigma_9^x$ [11]. We can also define the logical operators $X_L \equiv \sigma_1^z \sigma_2^z \cdots \sigma_9^z$, $Z_L \equiv \sigma_1^x \sigma_2^x \cdots \sigma_9^x$ and $Y_L = iX_L Z_L$. Let the last stabilizer be $g_9 = \pm X_L$, which determines a pair of logical space basis states $|\pm\rangle_L$. For both choices, Eq. (3.10) gives $h_{\max} = 2$, and the emission circuit solutions for $|\pm\rangle_L$ are given in Fig. 3.10, where $|\pm\rangle_L$ are separately given by $R = \mathbb{1}$ and $R = X_{e_1}$. Therefore, by replacing R by a more general x-rotation, $e^{i\frac{\varphi}{2}X_{e_1}} \equiv \mathbb{1}\cos\frac{\varphi}{2} + iX_{e_1}\sin\frac{\varphi}{2}$, we can obtain a rotated logical qubit $|\varphi\rangle_L = e^{i\frac{\varphi}{2}Z_L}|+\rangle_L$, with an arbitrary angle φ. That is, the circuit in Fig. 3.10 allows us to transmit a rotated photonic logical qubit protected by the Shor code, with merely 2 emitter qubits, 1 two-qubit gate and 2 measurements, which is surprisingly simple.

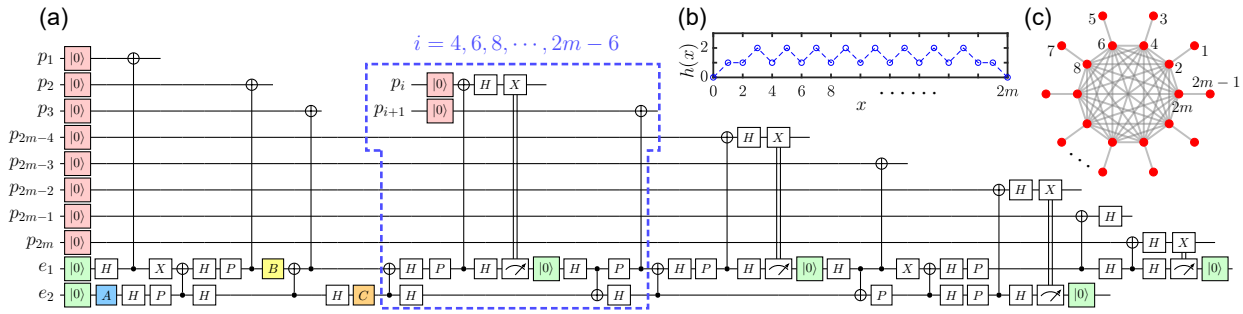

Figure 3.11: (a) and (b) show the emission circuit and height function for the repeater graph state of $2m$ photons displayed in (c). The boxed area of the circuit is repeated multiple times to generate photons $p_4, p_5, p_6, \cdots, p_{2m-6}$. (This figure is adapted from [5].)

3.2.4.3 Supplementary Note 3

In this section, we generalize the repeater graph state example from the main text and present explicit generation circuits for repeater graphs with arbitrarily many photons. As shown in Fig. 3.11, for a repeater graph state with $2m$ photons, the maximum of the height function indicates that we need 2 emitters regardless how large m is ($m \geq 4$). The unitary operations A, B and C displayed in Fig. 3.12(a) depend on m:

$$A = X_{e_2}^{\lfloor m/2 \rfloor + 1}, \quad B = X_{e_1}^{\lfloor m/2 \rfloor}, \quad C = P_{e_2}^{m} \ , \tag{3.13}$$

where $X_i = \sigma_i^x$, and $P = \mathrm{diag}(1, i)$. Compared to the approach given in previous work [124], which requires $m-1$ two-qubit gates and m measurements, the new solution in Fig. 3.11(a) uses $2m-3$ two-qubit gates and $m-1$ measurements, reducing the number of measurements needed to produce the state. We highlight that our method yields different solutions with flexible settings, so actually the solution from Ref. [124] can also be obtained from our algorithm.

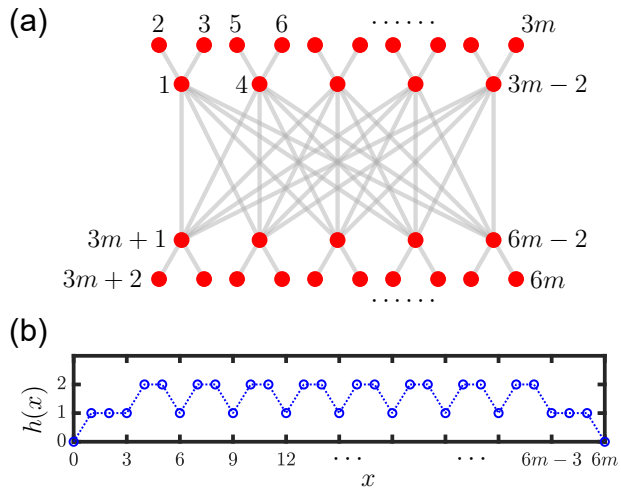

Figure 3.12: (a) The graph for RGS, which has $6m$ vertices. The labels represent the emission sequence. (b) The height function $h(x)$ for the target graph state in (a). (This figure is adapted from [5].)

3.2.4.4 Supplementary Note 4

Finally, we consider a modified repeater graph state that includes some additional redundancy to further boost the likelihood of successful Bell measurements [124]. Fig. 3.12(a) shows an example of such a repeater graph state with $6m$ photons ($m > 3$). Note that compared to the state in Fig. 3.11(c), this state contains twice as many external photon arms and is missing those internal edges that are not necessary for the functionality of this state as a repeater. Fig. 3.12(b) shows that the height function is at most 2 for any $m > 3$, i.e., only two emitter qubits are needed to generate the state in (a). We list all operations in the generation circuit in Eq. (3.9). Denoting the e_1-th and the e_2-th qubits as the emitter

qubits, where $e_1 = 6m+1$ and $e_2 = 6m+2$, the circuit is given by:

$$
\begin{aligned}
W_0 &= \mathrm{CNOT}_{e_1 e_2} H_{e_1} H_{e_2} \\
\eta_j &= \begin{cases} e_2, & 6m-5 \le j \le 6m-3 \\ e_1, & \text{otherwise} \end{cases} \\
U_{p,j} &= \begin{cases} \mathbb{1}, & j = 1 \pmod 3 \\ H_j, & \text{otherwise} \end{cases} \\
U_{e,j} &= \begin{cases} \mathrm{CNOT}_{e_2 e_1}, & j = 3 \\ H_{e_1}, & j = 3k \text{ with } 2 \le k \le 2m \\ H_{e_2}, & j = 6m-3 \\ \mathbb{1}, & \text{otherwise} \end{cases}
\end{aligned}
,
\quad
\begin{aligned}
\mu_j &= \begin{cases} e_1, & j = 3k \text{ with } 2 \le k \le 2m, \\ & \qquad \text{and } k \ne 2m-1 \\ e_2, & j = 6m-3 \\ \text{not assigned}, & \text{otherwise} \end{cases} \\
W_j &= \begin{cases} \mathrm{CNOT}_{e_1 e_2}, & j = 3k \text{ with } 2 \le k \le 2m-2, \\ & \qquad \text{and } k \ne m-1 \\ H_{e_2}\mathrm{CNOT}_{e_1 e_2}, & j = 3m-3 \\ H_{e_2}, & j = 6m-3 \\ H_{e_1}, & j = 6m \\ \mathbb{1}, & \text{otherwise} \end{cases}
\end{aligned}
. \tag{3.14}
$$

In the above circuit, there are $2m-1$ measurements, and $2m-1$ CNOT gates. Plugging these operations into Eq. (3.9) gives the full sequence.

Chapter 4

Conclusion and Outlook

This dissertation has mainly discussed two topics from the theoretical perspective: how to control matter qubits in a noisy environment and how to generate multiparty entangled photonic qubits with the minimal available resource. The first topic is included in chapter 2. Besides brief reviews of open system dynamics, error channels, quantum error correction, and some traditional control theories, the original works presented here comprise the combination of geometric formalism with filter functions and artificial neural networks. These parts of the work rely on numerical methods to design appropriate control functions. Concretely, we have shown that the geometric formalism can assist in finding dynamical error-correcting gates with better filter functions, and machine learning can tackle the time-optimizing problem in quantum control with unhandy constraints. The second topic is presented in chapter 3, where we have introduced the features of the photonic qubit and some prospective applications with quantum optics. Particularly, as a resource state, we give the concept of graph state and several of its properties. Finally, we have presented the deterministic method of generating photonic graph states with quantum emitters. An original work of optimizing the quantum emitter number based on the stabilizer formalism is provided at the end.

Based on this progress, there are plenty of possibilities to be explored. For example, our exploration of designing control pulses with physics-informed neural networks is quite primitive. We look forward to designing control pulses for multi-qubit gates, multi-level systems, and self-robust pulses with machine learning. Improving the efficiency of the machine learning

approach by investigating different network architectures and algorithms is also important and worth studying. Regarding the photonic resource state generation protocol, we hope to develop a protocol that is equipped with fault-tolerant features, such that the generation scheme is more robust for practical implementations. Also, it would be interesting to consider optimizing the overall resource use in the protocol under different contexts and constraints.

Bibliography

[1] Edwin Barnes, Fernando A Calderon-Vargas, Wenzheng Dong, Bikun Li, Junkai Zeng, and Fei Zhuang. Dynamically corrected gates from geometric space curves. *Quantum Science and Technology*, 7(2):023001, jan 2022.

[2] Bikun Li, Fernando A. Calderon-Vargas, Junkai Zeng, and Edwin Barnes. Designing arbitrary single-axis rotations robust against perpendicular time-dependent noise. *New Journal of Physics*, 23(9):093032, sep 2021.

[3] Götz S. Uhrig. Keeping a quantum bit alive by optimized π-pulse sequences. *Phys. Rev. Lett.*, 98:100504, Mar 2007.

[4] I. Schwartz, D. Cogan, E. R. Schmidgall, Y. Don, L. Gantz, O. Kenneth, N. H. Lindner, and D. Gershoni. Deterministic generation of a cluster state of entangled photons. *Science*, 354(6311):434–437, 2016.

[5] Bikun Li, Sophia E. Economou, and Edwin Barnes. Photonic resource state generation from a minimal number of quantum emitters. *npj Quantum Information*, 8(1):11, Feb 2022.

[6] P.W. Shor. Algorithms for quantum computation: discrete logarithms and factoring. In *Proceedings 35th Annual Symposium on Foundations of Computer Science*, pages 124–134, 1994.

[7] Aram W. Harrow, Avinatan Hassidim, and Seth Lloyd. Quantum algorithm for linear systems of equations. *Phys. Rev. Lett.*, 103:150502, Oct 2009.

[8] Lov K. Grover. A fast quantum mechanical algorithm for database search. In *Proceedings of the Twenty-Eighth Annual ACM Symposium on Theory of Computing*, STOC '96, page 212–219, New York, NY, USA, 1996. Association for Computing Machinery.

[9] Charles H. Bennett and Gilles Brassard. Quantum cryptography: Public key distribution and coin tossing. *Theoretical Computer Science*, 560:7–11, 2014. Theoretical Aspects of Quantum Cryptography – celebrating 30 years of BB84.

[10] Ji-Gang Ren, Ping Xu, Hai-Lin Yong, Liang Zhang, Sheng-Kai Liao, Juan Yin, Wei-Yue Liu, Wen-Qi Cai, Meng Yang, Li Li, Kui-Xing Yang, Xuan Han, Yong-Qiang Yao, Ji Li, Hai-Yan Wu, Song Wan, Lei Liu, Ding-Quan Liu, Yao-Wu Kuang, Zhi-Ping He, Peng Shang, Cheng Guo, Ru-Hua Zheng, Kai Tian, Zhen-Cai Zhu, Nai-Le Liu, Chao-Yang Lu, Rong Shu, Yu-Ao Chen, Cheng-Zhi Peng, Jian-Yu Wang, and Jian-Wei Pan. Ground-to-satellite quantum teleportation. *Nature*, 549(7670):70–73, Sep 2017.

[11] Michael A. Nielsen and Isaac L. Chuang. *Quantum Computation and Quantum Information: 10th Anniversary Edition*. Cambridge University Press, USA, 10th edition, 2011.

[12] Daniel A. Lidar and Todd A. Brun. *Quantum Error Correction*. Cambridge University Press, 2013.

[13] L. M. K. Vandersypen and I. L. Chuang. NMR techniques for quantum control and computation. *Rev. Mod. Phys.*, 76:1037–1069, Jan 2005.

[14] Stephen Wimperis. Broadband, Narrowband, and Passband Composite Pulses for Use in Advanced NMR Experiments. *J. Magn. Reson. Ser. A*, 109(2):221–231, aug 1994.

[15] Terry Gullion, David B Baker, and Mark S Conradi. New, compensated carr-purcell sequences. *Journal of Magnetic Resonance (1969)*, 89(3):479–484, 1990.

[16] Lorenza Viola, Emanuel Knill, and Seth Lloyd. Dynamical decoupling of open quantum systems. *Phys. Rev. Lett.*, 82:2417–2421, Mar 1999.

[17] Lorenza Viola, Seth Lloyd, and Emanuel Knill. Universal control of decoupled quantum systems. *Phys. Rev. Lett.*, 83:4888–4891, Dec 1999.

[18] Lorenza Viola and Emanuel Knill. Robust dynamical decoupling of quantum systems with bounded controls. *Phys. Rev. Lett.*, 90:037901, Jan 2003.

[19] Junkai Zeng and Edwin Barnes. Fastest pulses that implement dynamically corrected single-qubit phase gates. *Physical Review A*, 98(1):012301, 2018.

[20] Junkai Zeng, Xiu-Hao Deng, Antonio Russo, and Edwin Barnes. General solution to inhomogeneous dephasing and smooth pulse dynamical decoupling. *New Journal of Physics*, 20(3):033011, 2018.

[21] Junkai Zeng, CH Yang, AS Dzurak, and Edwin Barnes. Geometric formalism for constructing arbitrary single-qubit dynamically corrected gates. *Physical Review A*, 99(5):052321, 2019.

[22] Donovan Buterakos, Sankar Das Sarma, and Edwin Barnes. Geometrical formalism for dynamically corrected gates in multiqubit systems. *PRX Quantum*, 2:010341, Mar 2021.

[23] E. Knill, R. Laflamme, and G. J. Milburn. A scheme for efficient quantum computation with linear optics. *Nature*, 409(6816):46–52, Jan 2001.

[24] Robert Raussendorf and Hans J. Briegel. A one-way quantum computer. *Phys. Rev. Lett.*, 86:5188–5191, May 2001.

[25] Sara Bartolucci et al. Fusion-based quantum computation. *Preprint at https://arxiv.org/abs/2101.09310*, 2021.

[26] Alberto Politi, Jonathan C.F. Matthews, Mark G. Thompson, and Jeremy L. O'Brien. Integrated quantum photonics. *IEEE Journal of Selected Topics in Quantum Electronics*, 15(6):1673–1684, 2009.

[27] Netanel H. Lindner and Terry Rudolph. Proposal for pulsed on-demand sources of photonic cluster state strings. *Phys. Rev. Lett.*, 103:113602, Sep 2009.

[28] Sophia E. Economou, Netanel Lindner, and Terry Rudolph. Optically generated 2-dimensional photonic cluster state from coupled quantum dots. *Phys. Rev. Lett.*, 105:093601, Aug 2010.

[29] Hannes Pichler, Soonwon Choi, Peter Zoller, and Mikhail D. Lukin. Universal photonic quantum computation via time-delayed feedback. *PNAS*, 114(43):11362–11367, 2017.

[30] M. Hein, J. Eisert, and H. J. Briegel. Multiparty entanglement in graph states. *Phys. Rev. A*, 69:062311, Jun 2004.

[31] Łukasz Cywiński, Wayne M. Witzel, and S. Das Sarma. Electron spin dephasing due to hyperfine interactions with a nuclear spin bath. *Phys. Rev. Lett.*, 102:057601, Feb 2009.

[32] Arian Vezvaee, Girish Sharma, Sophia E. Economou, and Edwin Barnes. Driven dynamics of a quantum dot electron spin coupled to a bath of higher-spin nuclei. *Phys. Rev. B*, 103:235301, Jun 2021.

[33] G. Lindblad. On the generators of quantum dynamical semigroups. *Communications in Mathematical Physics*, 48(2):119–130, Jun 1976.

[34] L.J. Landau and R.F. Streater. On birkhoff's theorem for doubly stochastic completely positive maps of matrix algebras. *Linear Algebra and its Applications*, 193:107–127, 1993.

[35] Guido Burkard, Thaddeus D. Ladd, John M. Nichol, Andrew Pan, and Jason R. Petta. Semiconductor spin qubits. *Preprint at https://arxiv.org/abs/2112.08863*, 2021.

[36] Jens Koch, Terri M. Yu, Jay Gambetta, A. A. Houck, D. I. Schuster, J. Majer, Alexandre Blais, M. H. Devoret, S. M. Girvin, and R. J. Schoelkopf. Charge-insensitive qubit design derived from the cooper pair box. *Phys. Rev. A*, 76:042319, Oct 2007.

[37] J. I. Cirac and P. Zoller. Quantum computations with cold trapped ions. *Phys. Rev. Lett.*, 74:4091–4094, May 1995.

[38] Łukasz Cywiński, Roman M. Lutchyn, Cody P. Nave, and S. Das Sarma. How to enhance dephasing time in superconducting qubits. *Phys. Rev. B*, 77:174509, May 2008.

[39] Peter Groszkowski, Alireza Seif, Jens Koch, and A. A. Clerk. Simple master equations for describing driven systems subject to classical non-markovian noise. *Preprint at https://arxiv.org/abs/2207.03980*, 2022.

[40] E. L. Hahn. Spin echoes. *Phys. Rev.*, 80:580–594, Nov 1950.

[41] H. Y. Carr and E. M. Purcell. Effects of diffusion on free precession in nuclear magnetic resonance experiments. *Phys. Rev.*, 94:630–638, May 1954.

[42] Zdeněk Tošner, Thomas Vosegaard, Cindie Kehlet, Navin Khaneja, Steffen J. Glaser, and Niels Chr. Nielsen. Optimal control in nmr spectroscopy: Numerical implementation in simpson. *Journal of Magnetic Resonance*, 197(2):120–134, 2009.

[43] Kaveh Khodjasteh and Lorenza Viola. Dynamically error-corrected gates for universal quantum computation. *Phys. Rev. Lett.*, 102:080501, Feb 2009.

[44] Todd J Green, Jarrah Sastrawan, Hermann Uys, and Michael J Biercuk. Arbitrary quantum control of qubits in the presence of universal noise. *New Journal of Physics*, 15(9):095004, sep 2013.

[45] A. Uhlmann. The "transition probability" in the state space of a $*$-algebra. *Reports on Mathematical Physics*, 9(2):273–279, 1976.

[46] Richard Jozsa. Fidelity for mixed quantum states. *Journal of Modern Optics*, 41(12):2315–2323, 1994.

[47] Mark D. Bowdrey, Daniel K.L. Oi, Anthony J. Short, Konrad Banaszek, and Jonathan A. Jones. Fidelity of single qubit maps. *Physics Letters A*, 294(5):258–260, 2002.

[48] Christoph Dankert, Richard Cleve, Joseph Emerson, and Etera Livine. Exact and approximate unitary 2-designs and their application to fidelity estimation. *Phys. Rev. A*, 80:012304, Jul 2009.

[49] N Cody Jones, Thaddeus D Ladd, and Bryan H Fong. Dynamical decoupling of a qubit with always-on control fields. *New Journal of Physics*, 14(9):093045, sep 2012.

[50] K. Khodjasteh and D. A. Lidar. Fault-tolerant quantum dynamical decoupling. *Phys. Rev. Lett.*, 95:180501, Oct 2005.

[51] Götz S Uhrig and Stefano Pasini. Efficient coherent control by sequences of pulses of finite duration. *New Journal of Physics*, 12(4):045001, apr 2010.

[52] Willi Freeden, M. Zuhair Nashed, and Michael Schreiner. *Slepian Functions: Basics and Settings*, pages 131–145. Springer International Publishing, Cham, 2018.

[53] V. M. Frey, S. Mavadia, L. M. Norris, W. de Ferranti, D. Lucarelli, L. Viola, and M. J. Biercuk. Application of optimal band-limited control protocols to quantum noise sensing. *Nature Communications*, 8(1):2189, Dec 2017.

[54] Dennis Lucarelli. Quantum optimal control via gradient ascent in function space and the time-bandwidth quantum speed limit. *Phys. Rev. A*, 97:062346, Jun 2018.

[55] Malcolm H. Levitt. Composite pulses. *Progress in Nuclear Magnetic Resonance Spectroscopy*, 18(2):61–122, jan 1986.

[56] G. Goelman, S. Vega, and D. B. Zax. Squared amplitude-modulated composite pulses. *J. Magn. Reson.*, 81:423, 1989.

[57] Holly K. Cummins, Gavin Llewellyn, and Jonathan A. Jones. Tackling systematic errors in quantum logic gates with composite rotations. *Phys. Rev. A*, 67:042308, 2003.

[58] Michael J. Biercuk, Hermann Uys, Aaron P. VanDevender, Nobuyasu Shiga, Wayne M. Itano, and John J. Bollinger. Optimized dynamical decoupling in a model quantum memory. *Nature*, 458:996, 2009.

[59] K. Khodjasteh, D. A. Lidar, and L. Viola. Arbitrarily accurate dynamical control in open quantum systems. *Phys. Rev. Lett.*, 104:090501, 2010.

[60] Jonathan A. Jones. Quantum computing with NMR. *Prog. Nucl. Magn. Reson. Spectrosc.*, 59(2):91–120, aug 2011.

[61] T. van der Sar, Z. H. Wang, M. S. Blok, H. Bernien, T. H. Taminiau, D.M. Toyli, D. A. Lidar, D. D. Awschalom, R. Hanson, and V. V. Dobrovitski. Decoherence-protected quantum gates for a hybrid solid-state spin register. *Nature*, 484:82–86, 2012.

[62] Xin Wang, Lev S. Bishop, J. P. Kestner, Edwin Barnes, Kai Sun, and S. Das Sarma. Composite pulses for robust universal control of singlet-triplet qubits. *Nat. Commun.*, 3:997, 2012.

[63] Todd J Green, Jarrah Sastrawan, Hermann Uys, and Michael J Biercuk. Arbitrary quantum control of qubits in the presence of universal noise. *New Journal of Physics*, 15(9):095004, 2013.

[64] J. P. Kestner, Xin Wang, Lev S. Bishop, Edwin Barnes, and S. Das Sarma. Noise-resistant control for a spin qubit array. *Phys. Rev. Lett.*, 110:140502, 2013.

[65] F. A. Calderon-Vargas and J. P. Kestner. Dynamically Correcting a CNOT Gate for any Systematic Logical Error. *Phys. Rev. Lett.*, 118(15):150502, apr 2017.

[66] J. R. Petta. Coherent Manipulation of Coupled Electron Spins in Semiconductor Quantum Dots. *Science*, 309(5744):2180–2184, sep 2005.

[67] Xin Wang, Lev S. Bishop, Edwin Barnes, J. P. Kestner, and S. Das Sarma. Robust quantum gates for singlet-triplet spin qubits using composite pulses. *Phys. Rev. A*, 89(2):022310, feb 2014.

[68] Genko T. Genov, Daniel Schraft, Thomas Halfmann, and Nikolay V. Vitanov. Correction of arbitrary field errors in population inversion of quantum systems by universal composite pulses. *Phys. Rev. Lett.*, 113:043001, Jul 2014.

[69] Xiao-Ming Zhang, Jianan Li, Xin Wang, and Man-Hong Yung. Minimal nonorthogonal gate decomposition for qubits with limited control. *Phys. Rev. A*, 99:052339, May 2019.

[70] Zhen-Yu Wang and Ren-Bao Liu. No-go theorems and optimization of dynamical decoupling against noise with soft cutoff. *Phys. Rev. A*, 87:042319, Apr 2013.

[71] J-M Cai, B. Naydenov, R. Pfeiffer, L. P. McGuinness, K. D. Jahnke, F. Jelezko, M. B. Plenio, and A. Retzker. Robust dynamical decoupling with concatenated continuous driving. *New J. Phys.*, 14(11):113023, nov 2012.

[72] L. Van Damme, Q. Ansel, S. J. Glaser, and D. Sugny. Robust optimal control of two-level quantum systems. *Phys. Rev. A*, 95:063403, Jun 2017.

[73] U. Boscain, M. Sigalotti, and D. Sugny. Introduction to the pontryagin maximum principle for quantum optimal control. *PRX Quantum*, 2:030203, Sep 2021.

[74] D. Liberzon. *Calculus of Variations and Optimal Control Theory: A Concise Introduction*. Princeton University Press, 2012.

[75] L. E. Dubins. On curves of minimal length with a constraint on average curvature, and with prescribed initial and terminal positions and tangents. *American Journal of Mathematics*, 79(3):497–516, 1957.

[76] Xu-Chen Yang, Man-Hong Yung, and Xin Wang. Neural-network-designed pulse sequences for robust control of singlet-triplet qubits. *Phys. Rev. A*, 97:042324, Apr 2018.

[77] Murphy Yuezhen Niu, Sergio Boixo, Vadim N. Smelyanskiy, and Hartmut Neven. Universal quantum control through deep reinforcement learning. *npj Quantum Information*, 5(1):33, Apr 2019.

[78] Xian Wang, Anshuman Kumar, Christian R. Shelton, and Bryan M. Wong. Harnessing deep neural networks to solve inverse problems in quantum dynamics: machine-learned predictions of time-dependent optimal control fields. *Phys. Chem. Chem. Phys.*, 22:22889–22899, 2020.

[79] David Xu, A. Barış Özgüler, Giuseppe Di Guglielmo, Nhan Tran, Gabriel N. Perdue,

Luca Carloni, and Farah Fahim. Neural network accelerator for quantum control. *Preprint at https://arxiv.org/abs/2208.02645*, 2022.

[80] Ariel Norambuena, Marios Mattheakis, Francisco J. González, and Raúl Coto. Physics-informed neural networks for quantum control. *Preprint at https://arxiv.org/abs/2206.06287*, 2022.

[81] M. Raissi, P. Perdikaris, and G.E. Karniadakis. Physics-informed neural networks: A deep learning framework for solving forward and inverse problems involving nonlinear partial differential equations. *Journal of Computational Physics*, 378:686–707, 2019.

[82] Qi Yao, Jun Zhang, Xiao-Feng Yi, Li You, and Wenxian Zhang. Uniaxial dynamical decoupling for an open quantum system. *Phys. Rev. Lett.*, 122:010408, Jan 2019.

[83] Diederik P. Kingma and Jimmy Ba. Adam: A method for stochastic optimization. In Yoshua Bengio and Yann LeCun, editors, *3rd International Conference on Learning Representations, ICLR 2015, San Diego, CA, USA, May 7-9, 2015, Conference Track Proceedings*, 2015.

[84] Daniel Gottesman. Stabilizer codes and quantum error correction. *Preprint at https://arxiv.org/abs/quant-ph/9705052*, 1997.

[85] Michael A. Nielsen and Isaac L. Chuang. *Quantum Computation and Quantum Information: 10th Anniversary Edition*. Cambridge University Press, 2010.

[86] Sergey Bravyi and Alexei Kitaev. Universal quantum computation with ideal clifford gates and noisy ancillas. *Phys. Rev. A*, 71:022316, Feb 2005.

[87] Anirudh Krishna and Jean-Pierre Tillich. Towards low overhead magic state distillation. *Phys. Rev. Lett.*, 123:070507, Aug 2019.

[88] Sergey Bravyi and Jeongwan Haah. Magic-state distillation with low overhead. *Phys. Rev. A*, 86:052329, Nov 2012.

[89] Peter W. Shor. Scheme for reducing decoherence in quantum computer memory. *Phys. Rev. A*, 52:R2493–R2496, Oct 1995.

[90] Emanuel Knill and Raymond Laflamme. Theory of quantum error-correcting codes. *Phys. Rev. A*, 55:900–911, Feb 1997.

[91] Charles H. Bennett, David P. DiVincenzo, John A. Smolin, and William K. Wootters. Mixed-state entanglement and quantum error correction. *Phys. Rev. A*, 54:3824–3851, Nov 1996.

[92] A. R. Calderbank and Peter W. Shor. Good quantum error-correcting codes exist. *Phys. Rev. A*, 54:1098–1105, Aug 1996.

[93] A.Yu. Kitaev. Fault-tolerant quantum computation by anyons. *Ann. Phys.*, 303(1):2–30, 2003.

[94] S. B. Bravyi and A. Yu. Kitaev. Quantum codes on a lattice with boundary. *Preprint at https://arxiv.org/abs/quant-ph/9811052*, 1998.

[95] Chao-Yang Lu, Wei-Bo Gao, Jin Zhang, Xiao-Qi Zhou, Tao Yang, and Jian-Wei Pan. Experimental quantum coding against qubit loss error. *Proceedings of the National Academy of Sciences*, 105(32):11050–11054, 2008.

[96] D. Nigg, M. Müller, E. A. Martinez, P. Schindler, M. Hennrich, T. Monz, M. A. Martin-Delgado, and R. Blatt. Quantum computations on a topologically encoded qubit. *Science*, 345(6194):302–305, 2014.

[97] Rajeev Acharya, Igor Aleiner, Richard Allen, Trond I. Andersen, Markus Ansmann, and *et al.* Suppressing quantum errors by scaling a surface code logical qubit. *Preprint at https://arxiv.org/abs/2207.06431*, 2022.

[98] Daniel Gottesman, Alexei Kitaev, and John Preskill. Encoding a qubit in an oscillator. *Phys. Rev. A*, 64:012310, Jun 2001.

[99] Qubit stabilizer code. In Victor V. Albert and Philippe Faist, editors, *The Error Correction Zoo*. 2022.

[100] Daniel Gottesman. The Heisenberg representation of quantum computers. *Preprint at https://arxiv.org/abs/quant-ph/9807006*, 1998.

[101] Scott Aaronson and Daniel Gottesman. Improved simulation of stabilizer circuits. *Phys. Rev. A*, 70:052328, Nov 2004.

[102] Koenraad M. R. Audenaert and Martin B Plenio. Entanglement on mixed stabilizer states: normal forms and reduction procedures. *New J. Phys.*, 7:170, may 2005.

[103] Sergey Bravyi, Dan Browne, Padraic Calpin, Earl Campbell, David Gosset, and Mark Howard. Simulation of quantum circuits by low-rank stabilizer decompositions. *Quantum*, 3:181, September 2019.

[104] J. Pablo Bonilla Ataides, David K. Tuckett, Stephen D. Bartlett, Steven T. Flammia, and Benjamin J. Brown. The xzzx surface code. *Nature Communications*, 12(1):2172, Apr 2021.

[105] H. Bombin and M. A. Martin-Delgado. Topological computation without braiding. *Phys. Rev. Lett.*, 98:160502, Apr 2007.

[106] Adam Nahum, Jonathan Ruhman, Sagar Vijay, and Jeongwan Haah. Quantum entanglement growth under random unitary dynamics. *Phys. Rev. X*, 7:031016, Jul 2017.

[107] Yaodong Li, Xiao Chen, and Matthew P. A. Fisher. Measurement-driven entanglement transition in hybrid quantum circuits. *Phys. Rev. B*, 100:134306, Oct 2019.

[108] Matthew P. A. Fisher, Vedika Khemani, Adam Nahum, and Sagar Vijay. Random quantum circuits. *Preprint at https://arxiv.org/abs/2207.14280*, 2022.

[109] Nicolas Gisin and Rob Thew. Quantum communication. *Nat. Photonics*, 1(3):165–171, Mar 2007.

[110] L A Lugiato, A Gatti, and E Brambilla. Quantum imaging. *J. Opt. B: Quantum Semiclass. Opt.*, 4(3):S176–S183, apr 2002.

[111] Daniel Gottesman, Thomas Jennewein, and Sarah Croke. Longer-baseline telescopes using quantum repeaters. *Phys. Rev. Lett.*, 109:070503, Aug 2012.

[112] Koji Azuma, Kiyoshi Tamaki, and Hoi-Kwong Lo. All-photonic quantum repeaters. *Nat. Commun.*, 6(1):6787, Apr 2015.

[113] T. C. Ralph, A. J. F. Hayes, and Alexei Gilchrist. Loss-tolerant optical qubits. *Phys. Rev. Lett.*, 95:100501, Aug 2005.

[114] Michael Varnava, Daniel E. Browne, and Terry Rudolph. Loss tolerance in one-way quantum computation via counterfactual error correction. *Phys. Rev. Lett.*, 97:120501, Sep 2006.

[115] Eric Chitambar and Gilad Gour. Quantum resource theories. *Rev. Mod. Phys.*, 91:025001, Apr 2019.

[116] W. Dür, G. Vidal, and J. I. Cirac. Three qubits can be entangled in two inequivalent ways. *Phys. Rev. A*, 62:062314, Nov 2000.

[117] Miguel Navascués, Elie Wolfe, Denis Rosset, and Alejandro Pozas-Kerstjens. Genuine network multipartite entanglement. *Phys. Rev. Lett.*, 125:240505, Dec 2020.

[118] Mohsen Bahramgiri and Salman Beigi. Graph states under the action of local clifford group in non-binary case. *Preprint at https://arxiv.org/abs/quant-ph/0610267*, 2006.

[119] S. Anders, M. B. Plenio, W. Dür, F. Verstraete, and H.-J. Briegel. Ground-state approximation for strongly interacting spin systems in arbitrary spatial dimension. *Phys. Rev. Lett.*, 97:107206, Sep 2006.

[120] M Rossi, M Huber, D Bruß, and C Macchiavello. Quantum hypergraph states. *New Journal of Physics*, 15(11):113022, nov 2013.

[121] Maarten Van den Nest, Jeroen Dehaene, and Bart De Moor. Graphical description of the action of local clifford transformations on graph states. *Phys. Rev. A*, 69:022316, Feb 2004.

[122] Maarten Van den Nest, Jeroen Dehaene, and Bart De Moor. Efficient algorithm to recognize the local clifford equivalence of graph states. *Phys. Rev. A*, 70:034302, Sep 2004.

[123] Mohsen Bahramgiri and Salman Beigi. An efficient algorithm to recognize locally equivalent graphs in non-binary case. *Preprint at https://arxiv.org/abs/cs/0702057*, 2007.

[124] Donovan Buterakos, Edwin Barnes, and Sophia E. Economou. Deterministic generation of all-photonic quantum repeaters from solid-state emitters. *Phys. Rev. X*, 7:041023, Oct 2017.

[125] F. Hahn, A. Pappa, and J. Eisert. Quantum network routing and local complementation. *npj Quantum Information*, 5(1):76, Sep 2019.

[126] Yuan Zhan and Shuo Sun. Deterministic generation of loss-tolerant photonic cluster states with a single quantum emitter. *Phys. Rev. Lett.*, 125:223601, Nov 2020.

[127] Kianna Wan, Soonwon Choi, Isaac H. Kim, Noah Shutty, and Patrick Hayden. Fault-tolerant qubit from a constant number of components. *PRX Quantum*, 2:040345, Dec 2021.

[128] D. Schlingemann and R. F. Werner. Quantum error-correcting codes associated with graphs. *Phys. Rev. A*, 65:012308, Dec 2001.

[129] H.-J. Briegel, W. Dür, J. I. Cirac, and P. Zoller. Quantum repeaters: The role of imperfect local operations in quantum communication. *Phys. Rev. Lett.*, 81:5932–5935, Dec 1998.

[130] W. Dür, H.-J. Briegel, J. I. Cirac, and P. Zoller. Quantum repeaters based on entanglement purification. *Phys. Rev. A*, 59:169–181, Jan 1999.

[131] Nicolas Sangouard, Christoph Simon, Hugues de Riedmatten, and Nicolas Gisin. Quantum repeaters based on atomic ensembles and linear optics. *Rev. Mod. Phys.*, 83:33–80, Mar 2011.

[132] Sreraman Muralidharan et al. Optimal architectures for long distance quantum communication. *Sci. Rep.*, 6(1):20463, Feb 2016.

[133] C. L. Degen, F. Reinhard, and P. Cappellaro. Quantum sensing. *Rev. Mod. Phys.*, 89:035002, Jul 2017.

[134] Jonathan P. Dowling. Quantum optical metrology – the lowdown on high-n00n states. *Cont. Phys.*, 49(2):125–143, Mar 2008.

[135] Daniel E. Browne and Terry Rudolph. Resource-efficient linear optical quantum computation. *Phys. Rev. Lett.*, 95:010501, Jun 2005.

[136] Wei-Bo Gao et al. Experimental demonstration of a hyper-entangled ten-qubit schrödinger cat state. *Nat. Phys.*, 6(5):331–335, May 2010.

[137] Jin-Peng Li et al. Multiphoton graph states from a solid-state single-photon source. *ACS Photonics*, 7(7):1603–1610, Jul 2020.

[138] Kae Nemoto et al. Photonic architecture for scalable quantum information processing in diamond. *Phys. Rev. X*, 4:031022, Aug 2014.

[139] Hyeongrak Choi, Mihir Pant, Saikat Guha, and Dirk Englund. Percolation-based architecture for cluster state creation using photon-mediated entanglement between atomic memories. *npj Quantum Information*, 5(1):104, 2019.

[140] C. Schön, E. Solano, F. Verstraete, J. I. Cirac, and M. M. Wolf. Sequential generation of entangled multiqubit states. *Phys. Rev. Lett.*, 95:110503, Sep 2005.

[141] C. Schön, K. Hammerer, M. M. Wolf, J. I. Cirac, and E. Solano. Sequential generation of matrix-product states in cavity qed. *Phys. Rev. A*, 75:032311, Mar 2007.

[142] Netanel H. Lindner and Terry Rudolph. Proposal for pulsed on-demand sources of photonic cluster state strings. *Phys. Rev. Lett.*, 103:113602, Sep 2009.

[143] Jean-Claude Besse et al. Realizing a deterministic source of multipartite-entangled photonic qubits. *Nat. Commun.*, 11(1):4877, Sep 2020.

[144] Sophia E. Economou, Netanel Lindner, and Terry Rudolph. Optically generated 2-dimensional photonic cluster state from coupled quantum dots. *Phys. Rev. Lett.*, 105:093601, Aug 2010.

[145] Mercedes Gimeno-Segovia, Terry Rudolph, and Sophia E. Economou. Deterministic generation of large-scale entangled photonic cluster state from interacting solid state emitters. *Phys. Rev. Lett.*, 123:070501, Aug 2019.

[146] Antonio Russo, Edwin Barnes, and Sophia E. Economou. Photonic graph state generation from quantum dots and color centers for quantum communications. *Phys. Rev. B*, 98:085303, Aug 2018.

[147] Paul Hilaire, Edwin Barnes, and Sophia E. Economou. Resource requirements for efficient quantum communication using all-photonic graph states generated from a few matter qubits. *Quantum*, 5:397, February 2021.

[148] Johannes Borregaard et al. One-way quantum repeater based on near-deterministic photon-emitter interfaces. *Phys. Rev. X*, 10:021071, Jun 2020.

[149] Cathryn P. Michaels et al. Multidimensional cluster states using a single spin-photon interface coupled strongly to an intrinsic nuclear register. *Quantum*, 5:565, Oct 2021.

[150] Antonio Russo, Edwin Barnes, and Sophia E Economou. Generation of arbitrary all-photonic graph states from quantum emitters. *New J. Phys.*, 21(5):055002, may 2019.

[151] M Van den Nest, W Dür, A Miyake, and H J Briegel. Fundamentals of universality in one-way quantum computation. *New J. Phys.*, 9(6):204 – 204, jun 2007.

[152] Peter Høyer, Mehdi Mhalla, and Simon Perdrix. Resources Required for Preparing Graph States. In *17th International Symposium on Algorithms and Computation (ISAAC 2006)*, volume 4288 of *Lecture Notes in Computer Science*, pages 638 – 649, Kolkata, India, December 2006.

[153] M. Hein et al. Entanglement in graph states and its applications. *Preprint at https://arxiv.org/abs/quant-ph/0602096*, 2006.

[154] Marcus Cramer et al. Efficient quantum state tomography. *Nat. Commun.*, 1(1):149, Dec 2010.

[155] Román Orús. A practical introduction to tensor networks: Matrix product states and projected entangled pair states. *Ann. Phys.*, 349:117–158, 2014.

[156] E. N. Gilbert. Random Graphs. *Ann. Math. Stat.*, 30(4):1141 – 1144, 1959.

[157] David Fattal, Yoshihisa Yamamoto Toby S. Cubitt, Sergey Bravyi, and Isaac L. Chuang. Entanglement in the stabilizer formalism. *Preprint at https://arxiv.org/abs/quant-ph/0406168*, 2004.

[158] Sang il Oum. Rank-width: Algorithmic and structural results. *Discret. Appl. Math.*, 231:15–24, 2017. Algorithmic Graph Theory on the Adriatic Coast.

[159] J. L. Massey. Foundation and methods of channel encoding. *Proc. Int. Conf. on Information Theory and Systems*, 65, 1978. (Berlin, Germany, Sept. 1978).

[160] Sang il Oum. Rank-width and vertex-minors. *J. Combin. Theory Ser. B*, 95(1):79–100, 2005.

[161] Jisu Jeong, Eun Jung Kim, and Sang-il Oum. The "art of trellis decoding" is fixed-parameter tractable. *IEEE Trans. Inform. Theory*, 63(11):7178–7205, 2017.

[162] Isolde Adler, Mamadou Moustapha Kanté, and O-joung Kwon. Linear rank-width of distance-hereditary graphs I. A polynomial-time algorithm. *Algorithmica*, 78(1):342–377, May 2017.

[163] Bikun Li. Photon-emission-circuit-solver: Emission circuit solver for photonics stabilizer state, 2021. https://doi.org/10.5281/zenodo.5652105.

[164] Eugene P. Wigner. On the distribution of the roots of certain symmetric matrices. *Annals of Mathematics*, 67(2):325–327, 1958.